3D Printed PETG S-Shaped Auxetic Structure: An Experimental and Numerical Study
(versão final após defesa)

Beatriz Teixeira Fernandes

Dissertação para obtenção do Grau de Mestre em
Engenharia Aeronáutica
(mestrado integrado)

Orientador: Prof. Doutor Thiago Assis Dutra
Co-orientador: Prof. Doutor Abílio Manuel Pereira da Silva
Co-orientador: Mestre Martim Lima de Aguiar

Covilhã, abril de 2024

Declaração de Integridade

Eu, Beatriz Teixeira Fernandes, que abaixo assino, estudante com o número de inscrição a41591 de/o Mestrado Integrado em Engenharia Aeronáutica da Faculdade de Engenharia, declaro ter desenvolvido o presente trabalho e elaborado o presente texto em total consonância com o **Código de Integridades da Universidade da Beira Interior**.

Mais concretamente afirmo não ter incorrido em qualquer das variedades de Fraude Académica, e que aqui declaro conhecer, que em particular atendi à exigida referenciação de frases, extratos, imagens e outras formas de trabalho intelectual, e assumindo assim na íntegra as responsabilidades da autoria.

Universidade da Beira Interior, Covilhã, 20/04/2024.

Beatriz Teixeira Fernandes

Acknowledgements

I would like to express my sincere gratitude to all those who have supported and contributed to the successful completion of this dissertation. This journey would have been an insurmountable challenge without the unwavering assistance and motivation of several people. Foremost, I extend my deepest gratitude to my dissertation advisor, Professor Thiago Dutra, whose invaluable guidance, mentorship, and steadfast support played a pivotal role in this research endeavor. His expertise, patience, dedication, and encouragement have pushed me to explore knowledge beyond the boundaries of my field and comfort zone, profoundly shaping this dissertation. This endeavor would not have been possible without the continuous exchange of insightful perspectives and discussions, as well as the motivation provided by Professor Abílio Silva. I am eternally thankful for his encouragement, patience, and positive influence. Additionally, I cannot adequately express my appreciation for Professor Martim Aguiar, whose generously shared knowledge and expertise, as well as his thoughtful guidance in additive manufacturing, made this work a reality. I am profoundly thankful to the Centre for Mechanical and Aerospace Science and Technologies (C-MAST) for their provision of laboratory resources, equipment, raw materials, and unwavering support in rendering services, to the Departamento das Ciências Aeroespaciais (DCA) for providing the knowledge throughout the course and to Departamento de Engenharia Eletromecânica (DEM) for their willingness to provide equipment, materials and support, without which this work would not have been possible.. A special mention is reserved for my family, whose boundless love, encouragement, and understanding sustained me through the peaks and valleys of this academic journey. Your unwavering support has been my rock of stability. Lastly, I extend my gratitude to my friends, who have become my chosen family. In particular, I want to express my deep appreciation to João Cristóvão, who has been with me since day one of this journey, Gonçalo Silva, for his unwavering support over the years and significant contributions to this work, and Guilherme Quaresma, for his patience and unwavering friendship.

Resumo

Esta dissertação tem como interesse principal investigar estruturas auxéticas e as suas possíveis aplicações, especialmente no setor aeronáutico. Devido às propriedades únicas destas estruturas, elas cada vez mais ganham importância na indústria aeronáutica por conseguirem dar resposta a muitos problemas e dificuldades nesta indústria. As estruturas auxéticas têm possivel aplicação em estruturas leves, de altas propriedades mecânicas e com grande capacidade de absorção de energia. Durante a realização deste estudo, percebe-se que o fabrico aditivo (AM) é uma tecnologia que tem um papel muito importante nas estruturas auxéticas uma vez que permite a construção de estruturas complexas, que é o caso das estruturas auxéticas. Após ter sido feita uma revisão dos vários tipos de estruturas auxéticas, uma das estruturas destacou-se, não só pela sua forma invulgar, mas também pelas suas propriedades. Esta estrutura em forma de S, destaca-se pelas seguintes propriedades: concentração de esforços reduzida, elevada capacidade de absorção de energia e elevada recuperação elástica. Devido a este destaque, decidiu-se estudar em pormenor esta estrutura. Neste trabalho fabricaram-se várias amostras de estruturas em forma de S, utilizando AM como método de fabrico e o politereftalato de etileno glicol (PETG) como material. As amostras foram submetidas a dois tipos de testes experimentais, testes de compressão e testes de recuperação de fluência. Desta forma foi possível obter informações valiosas acerca do comportamento destas estruturas sob carga e da sua recuperação após a aplicação de cargas. Também foi desenvolvido um modelo numérico para melhor compreensão da estrutura em forma S. O modelo númerico foi feito a partir dos dados obtidos com a caracterização do material PETG. Os resultados das simulações são meticulosamente comparados aos dados experimentais, destacando a eficácia dos modelos numéricos, apesar das complexidades inerentes. Por último, as descobertas deste trabalho projetam um futuro promissor para o PETG e para as estruturas auxéticas em diversos domínios da engenharia, incluindo compósitos, segurança automotiva, aeronáutica e aeroespacial. O alicerce estabelecido neste trabalho abre caminho para futuras pesquisas, possibilitando uma exploração mais profunda das possibilidades e implicações desses materiais e estruturas inovadoras.

Palavras-chave

Estruturas Auxéticas, Estrutura em forma de S, Coeficiente de Poisson, Fabrico Aditivo, PETG, Análise Numérica, Gémeo Digital

Abstract

This dissertation's main interest is to investigate auxetic structures and their potential applications, especially in the aeronautical sector. Due to the unique properties of these structures, they are increasingly gaining importance in the aeronautical industry for addressing many problems and challenges. Auxetic structures have potential applications in lightweight structures with high mechanical properties and a significant energy absorption capacity. During this study, it is understood that additive manufacturing (AM) plays a crucial role in auxetic structures as it allows the construction of complex structures, such as auxetic structures. After a review of various types of auxetic structures, one structure stood out, not only for its unusual shape but also for its properties. This S-shaped structure stands out for reduced stress concentration, high energy absorption capacity, and high elastic recovery. Due to this distinction, it was decided to study this structure in detail. In this work, several samples of S-shaped structures were manufactured using AM as the manufacturing method and polyethylene terephthalate glycol (PETG) as the material. The samples underwent two types of experimental tests, compression tests, and creep-recovery tests. This allowed obtaining valuable information about the behavior of these structures under load and their recovery after the application of loads. A numerical model was also developed to better understand the S-shaped structure. The numerical model was based on data obtained from the characterization of the PETG material. The simulation results are meticulously compared to experimental data, highlighting the effectiveness of the numerical models despite inherent complexities. Finally, the findings of this work project a promising future for PETG and auxetic structures in various engineering domains, including composites, automotive safety, aeronautics, and aerospace. The foundation established in this work paves the way for future research, enabling a deeper exploration of the possibilities and implications of these innovative materials and structures.

Keywords

Auxetic Structures, S-shaped Structure, Poisson's Ratio, Additive Manufacturing, PETG, Numerical Analysis, Digital Twin

Contents

List of Figures

List of Tables

Acronyms and Abbreviations

2D	Two-Dimensional
3D	Three-Dimensional
ABS	Acrylonitrile Butadiene Styrene
AM	Additive Manufacturing
ASTM	American Society for Testing and Materials
BJ	Binder Jetting
CAD	Computer-Aided Design
CAM	Computer-Aided Manufacturing
CDLP	Continuous Digital Light Processing
CoV	Coefficient of Variation
DLP	Digital Light Processing
DMLS	Direct Metal Laser Sintering
DOD	Drop On Demand
EBAM	Electron Beam Additive Manufacturing
EBM	Electron Beam Melting
EMUDA	Empirical Modelling Using Dummy Atoms
FEA	Finite Element Analysis
FFF	Fused Filament Fabrication
FRP	Fiber Reinforced Polymer
LCD	Liquid Crystal Display
LENS	Laser Engineering Net Shape
LOM	Laminated Object Manufacturing
MJF	Multi Jet Fusion
NC	Numerical Control
NPJ	Nano Particle Jetting
NPR	Negative Poisson’s Ratio
PETG	Polyethylene Terephthalate Glycol
PLA	Polylactic Acid
PPR	Positive Poisson’s Ratio
PTFE	Polytetrafluoroethylene
SEA	Specific Energy Absorption
SLA	Stereolithography
SLM	Selective Laser Melting
SLS	Selective Laser Sintering
STL	Stereo Lithography
TEA	Total Energy Absorption
TPU	Thermoplastic Polyurethane
UAV	Unmanned Aerial Vehicle

UC	Ultrasonic Consolidation
UTS	Ultimate Tensile Strength
ZPR	Zero Poisson’s Ratio

Symbols

Latin Symbols

A	Area	m^2
B	Derivative of the Shape Function	$-$
D	Material Constitutive Tensor	$-$
E	Young's Modulus	Pa
f	Equivalent Nodal Forces	N
F	External Forces	N
G	Shear Modulus	Pa
H	Hardness	Pa
k	Bulk Modulus	Pa
K	Stiffness	N/m
l	Length	m
L	Differential Operators	$-$
P	Load	N
q	Nodal Displacement	m
u	Displacement	m
U^i	Internal Deformation Energy	J
V^e	Work Done by External Forces	J
W	Work	J

Greek Symbols

γ	Coefficient of Evans	$-$
δ	Displacement	m
ε	Strain	m/m
ν	Poisson's Ratio	$-$
Π	Potential Energy Functional	J
σ	Stress	Pa
Φ	Shape Function	$-$

Chapter 1

Introduction

The main purpose of this initial chapter is to provide an overview of the significance of auxetic materials in the aeronautical and aerospace industries, with a particular focus on their unique properties. Furthermore, this chapter will explain the motivation for this study, its ambitions, and the organization of the documentation.

In recent decades, advances in structural engineering design and technology in a variety of sectors, including aeronautical and aerospace, automotive, sports, and leisure, have led to the development of new materials with superior performance characteristics to meet increasingly demanding engineering requirements. These materials must exhibit high stiffness and strength while also offering significant weight savings, resistance to corrosion and chemicals, low maintenance, and reduced costs [1].

The aviation industry, in particular, has been a significant driver of advanced material development, with composite materials becoming more common in aircraft designs. Both Boeing and Airbus, two of the most important players in the sector, are using them at an extensive level of usage on the B787 and A380, respectively, with up to 50 % by weight of the airframe in B787 consisting of reinforced plastics [2]. The use of fiber reinforced polymers (FRPs) promotes a reduction in weight, leading to reduced fuel costs, emissions, and maintenance [3].

Fiber-reinforced polymers (FRPs), also referred to as fiber-reinforced plastics, are composite materials consisting of a polymer matrix filled with reinforcing fibers. Composite materials can be engineered or obtained naturally. They are made up of two or more constituent materials with significantly different physical or chemical properties that remain distinct within the finished structure. Typically, the fiber component is strong and stiff, whereas the matrix component is weaker and less stiff. The objective of this combination is to produce a strong and rigid component with a low density. Typical polymer matrix systems include epoxy, vinyl ester, polyester thermosetting plastic, or phenol formaldehyde resins. Glass, carbon, or aramid fibers are commonly employed as reinforcements, while other fibers, such as paper, wood, or asbestos, have been used on occasion [4]. Composites with metal or ceramic matrices also exist as distinct classes. Figure 1.1 illustrates the constituents and their main role in fiber-reinforced composites.

FRP composites offer several significant advantages, including their lightweight nature, high specific strength and stiffness, noncorrosive properties, and ease of construction. These materials can be tailored by orienting the reinforcing fibers in the direction of maximum stiffness and strength, being able to obtain properties that meet specific performance requirements [1]. Consequently, they are adopted in a wide range of advanced engineering structures, from aircrafts, helicopters, and spacecrafts to boats, ships, offshore platforms, automobiles, sports equipment, chemical processing equipment, and civil infrastructure [4]. Composite materials have also found employment in unmanned aerial vehicles (UAVs), where their use has led to more complex and expensive UAVs. These systems are constructed from a range of specialized materials with the primary goal of increasing flight time and improving maneuverability [5].

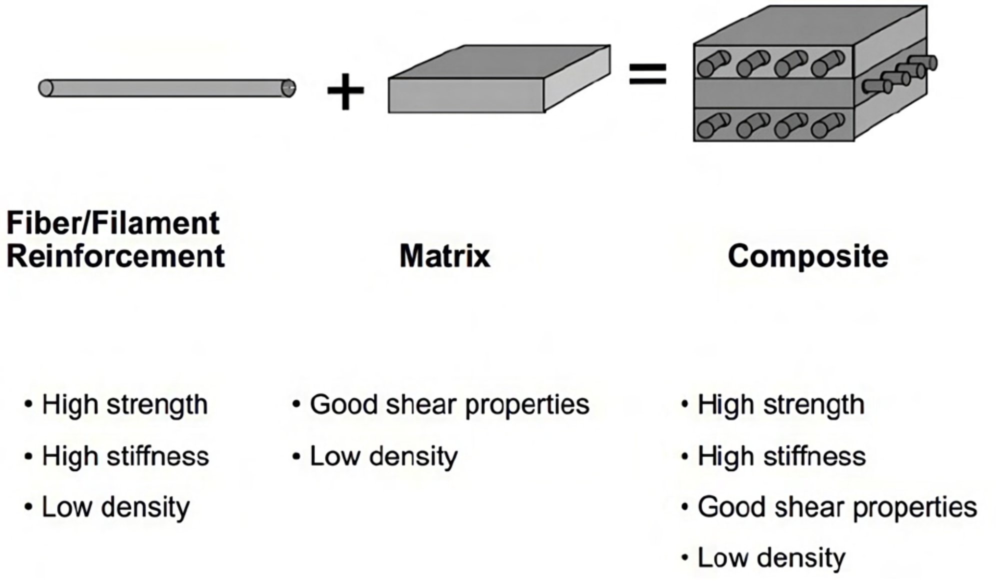

Figure 1.1: FRP composite constituents and their main role. Adapted from [6].

Simultaneous enhancement of strength, energy absorption, and weight reduction in structural components is a fundamental goal of engineering [7]. Consequently, FRPs have been utilized in lightweight sandwich composite structures. These structures are widely used in the automotive, sports, aeronautic, and aerospace industries [8] due to their high stiffness, strength, and energy absorption capabilities [9]. The incorporation of these structures into aircrafts results in improved acceleration, reduced fuel consumption, and lower lifecycle costs. Furthermore, their utilization in several applications results in lower operating costs [10].

Sandwich structures consist of two high-strength and hardness FRP face sheets enclosing a low-density core [11]. The core and face sheets may be composed of the same or different materials [12]. The mechanical properties of these structures are largely influenced by the cellular structure topology of the core, the materials used for the core and face sheets, and the geometry of the panel. The selection of material for the face sheets and the topology of the cellular structure of the core are crucial factors in determining the properties of the sandwich panel for a specific application, such as structural stiffness [13], energy absorption capacity [14], vibration and acoustic attenuation [15], and thermal insulation [16].

Sandwich panels are typically loaded in bending, and the constituent components of the structure perform various functions under such conditions. Their face sheets, depending on their location relative to the load, can experience compressive or tensile stresses [17] and provide in-plane strength and stiffness, as well as protection for the inner materials. The core of the sandwich panel performs two critical functions. First, it serves to separate the face sheets, thereby increasing the second moment of area, and consequently increasing the panel's rigidity. Second, the core supports the shear loads generated by bending, thus contributing to the out-of-plane strength and stiffness of the sandwich panel, while maintaining its lightweight nature [1]. Figure 1.2 illustrates a sandwich composite that undergoes bending deformation. In general, sandwich constructions offer a particular combination of low weight and high mechanical properties.

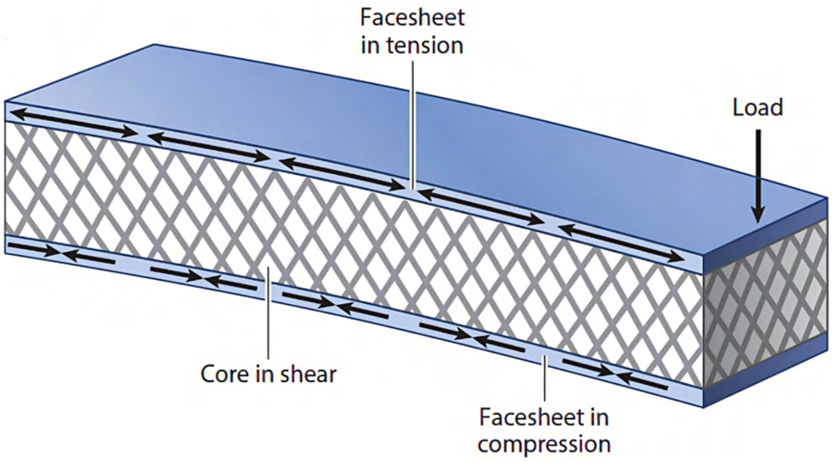

Figure 1.2: Sandwich composite structure under bending load. Adapted from [8].

The quest for lighter structures has led to the advancement and refinement of high-performance composite sandwich structures. With the aim of improving their mechanical properties, composite sandwich structures with diverse core topologies have been fabricated and examined [18]. The evaluated core topologies include lattice trusses [19, 20, 21, 22, 23], prismatics [24, 25, 26, 27], honeycomb [28, 29, 30, 31, 32], and foam cores [33, 34, 35, 36, 37]. Among them, honeycomb cores presently predominate in such structures, which have found specific utility in the aerospace industry, particularly in aircrafts [38].

In aerospace and aeronautical industries, advanced structures require the use of materials with high shear strength and modulus, high impact strength, especially against low-velocity impacts arising from runway debris or bird strikes, increased energy absorption, improved fatigue resistance, and easy detection and repair of damaged sections. Although conventional composites possess many desirable properties, they lack certain characteristics such as impact resistance, energy absorption, and repairability [1].

These requirements can be met by a new class of material called auxetic materials. Auxetic materials have emerged as a new class of mechanical metamaterials exhibiting exceptional properties compared to conventional materials. The term auxetic was first defined by Evans in 1991 and is derived from the Greek term “auxetos”, meaning “tends to expand” [39]. Most materials possess a positive Poisson’s ratio (PPR), whereby they laterally expand when longitudinally compressed and laterally contract when stretched. In contrast, auxetic materials display counter-intuitive behavior due to their negative Poisson’s ratio (NPR). These materials laterally expand when stretched and laterally contract when longitudinally compressed [40]. Additionally, materials with zero Poisson’s ratio (ZPR) exhibit no transverse deformation in response to axial strain [41]. Figure 1.3 shows the different deformation modes associated with different Poisson’s ratios.

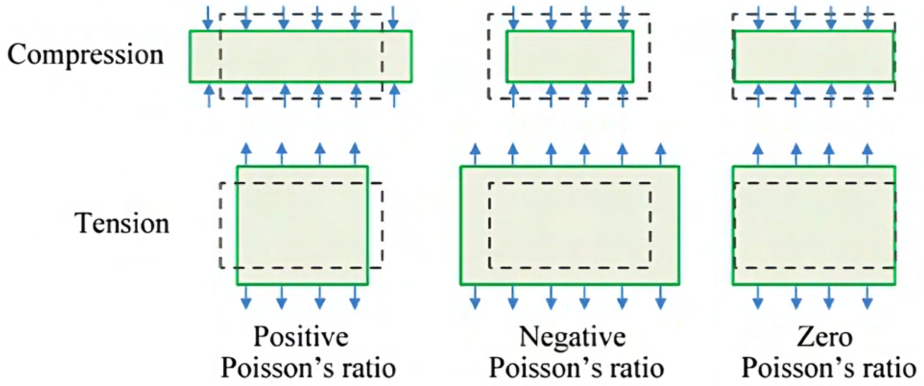

Figure 1.3: Deformation modes of materials with positive, negative, and zero Poisson’s ratio. Adapted from [42].

Auxetic materials have recently received significant attention due to their unconventional properties and a diverse range of potential applications, including sandwich composites [43]. These materials offer several advantages in engineering, such as reduced bending deflection [39] and increased shear modulus [44], making them suitable for use as sandwich core topologies. Among the various auxetic materials and structures that have been identified, the re-entrant honeycomb has garnered considerable interest from researchers. Comparative studies of sandwich structures with conventional honeycomb cores and those with re-entrant honeycomb cores revealed that the latter has improved shear properties due to snap-through instability, resulting in significantly higher energy absorption capacity compared to traditional materials [11].

Auxetic materials and structures possess several desirable properties due to their unique deformation characteristics under both compression and tension. These properties include enhanced shear modulus [45], indentation resistance [46], fracture resistance [47], synclastic behavior [44], variable permeability [48], and superior energy absorption performance [49]. A detailed analysis of these properties is presented in Subsection 2.1.

According to the literature, the auxetic properties of materials arise from their geometrical configuration rather than their inherent material properties [50]. Subsection 2.2 examines a variety of cellular auxetic elements and structures. Figure 1.4 summarizes a general classification of auxetic materials.

Auxetic behavior can be found in natural materials such as rocks, minerals, animal skin, and load-bearing cancellous bones found in human shins [40]. In addition to naturally occurring auxetic materials, synthetic auxetic materials have been developed, such as polyurethane [44], polytetrafluoroethylene (PTFE) [51], and ultra-high-molecular-weight polyethylene [50]. Auxetic textiles, including fibers [52], yarns [53], and fabrics [54], have also been produced. Furthermore, composite materials displaying auxetic properties, which are also known as auxetic composites, have been engineered recently.

Auxetic composites represent a distinct class of composite materials characterized by their auxetic behavior, which involves lateral expansion under longitudinal stretching and lateral contraction during compression [40]. Research in auxetic composites aims to leverage the advantages of both composites and auxetic properties, expanding their potential applications.

As highlighted in before, honeycomb structures are commonly utilized as cores in sandwich composites. A honeycomb single-cell in a sandwich composite is represented in Figure 1.5. An inherent issue with these honeycombs lies in their tendency to induce anticlastic or saddle-shaped curvatures, leading to localized damage and increased processing costs. This limitation has been addressed through the incorporation of a core possessing a negative Poisson's ratio (NPR), thereby introducing auxetic structures into composite sandwich panels. This approach presents an attractive solution for several engineering applications due to the improved mechanical properties and impact energy absorption capabilities of auxetic structures, which drives ongoing research into novel designs and performance enhancements [55].

Another avenue to achieve auxetic behavior in composites involves the use of the laminated angle-ply method, wherein the layers are strategically stacked to induce an NPR. Additionally, auxetic composites can be produced by integrating auxetic inclusions with varying geometries, proportions, and properties to confer auxetic characteristics to the final composite [40].

Being a special type of composite materials, auxetic composites share the common advantages of conventional composites, including high specific stiffness and strength, as well as lightweight properties. Furthermore, they inherit the unique attributes of auxetic materials, as it will be outlined in Section 2.1.

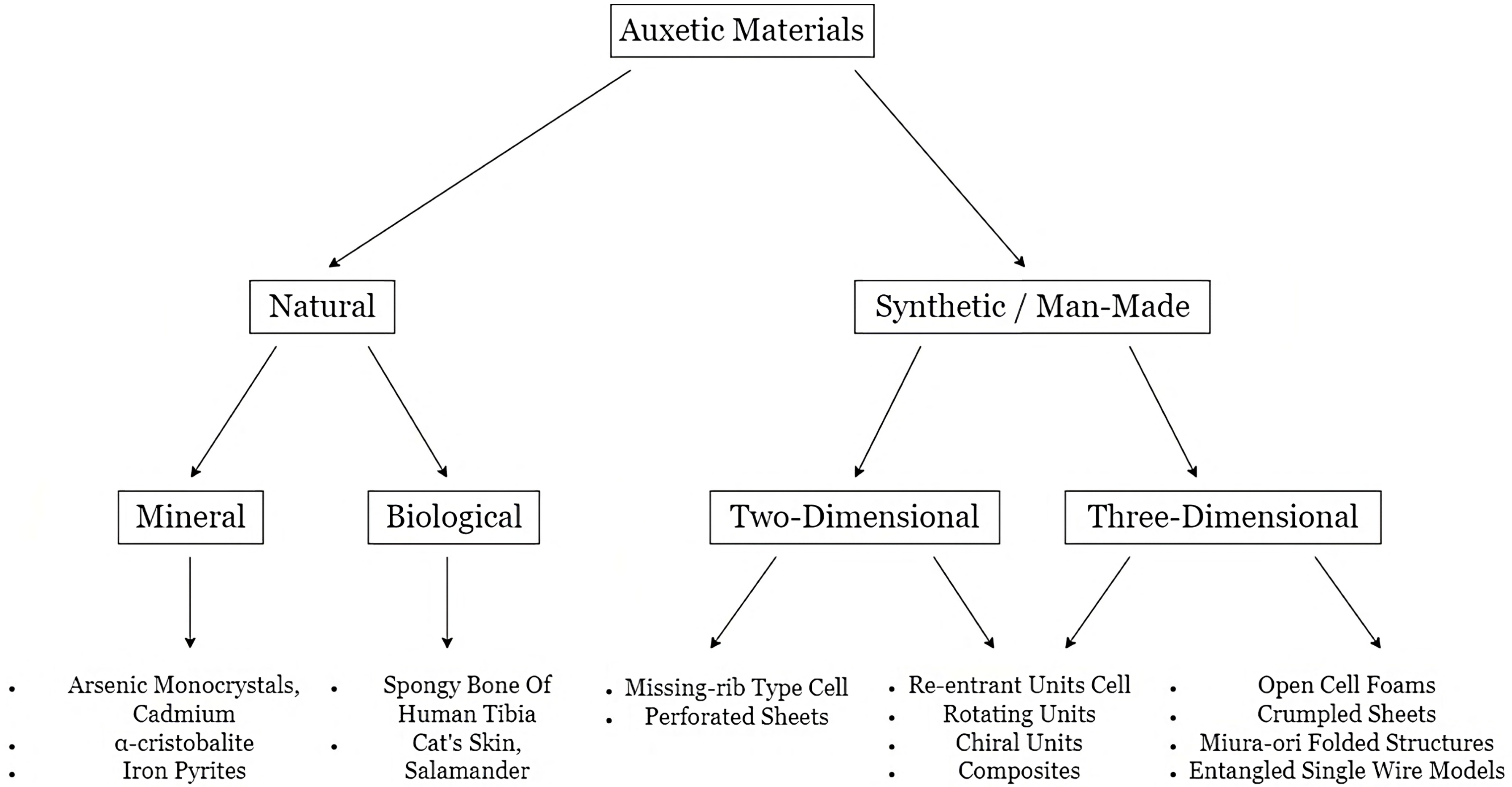

Figure 1.4: General classification of auxetic materials. Adapted from [56].

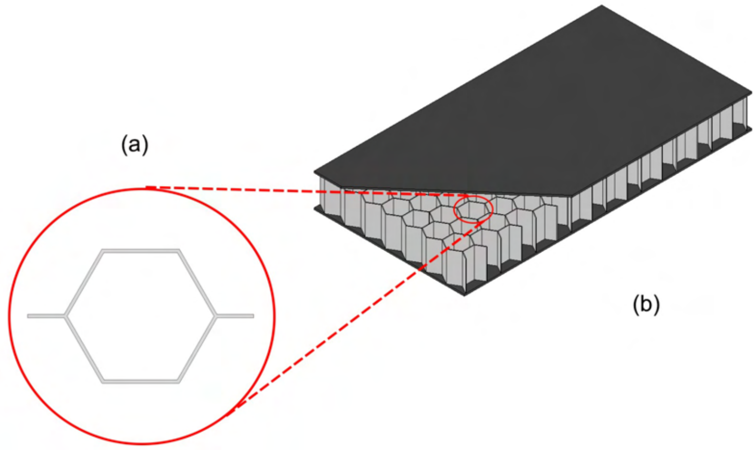

Figure 1.5: Representation of a (a) honeycomb single-cell in a (b) sandwich composite structure.

In view of these attributes, auxetic composites are suitable for use in high-profile applications such as aeronautical and aerospace engineering. Their high shear modulus renders them suitable for aerospace applications, particularly in components like wings that experience significant shear forces. The synclastic curvature property enhances their formability, making them valuable for shaping complex structures. Moreover, auxetic composites offer an excellent strength-to-weight ratio, which is a critical aspect for aircrafts. For example, they have the potential to improve performance, safety, and environmental impact through reduced weight and energy consumption. However, it is important to note that the challenge of large-scale manufacturing remains a limitation for auxetic composites [40].

1.1 Motivation

The motivation underlying this investigation into auxetic materials is rooted in their transformative potential across diverse industries and applications. Auxetic materials, distinguished by their negative Poisson's ratio (NPR), exhibit unconventional deformation under external forces. The envisaged impact of auxetic materials spans sectors such as aeronautics, aerospace, automotive, and composites, promising groundbreaking advancements.

The distinctive properties of auxetic materials position them as superior to conventional composites, particularly in aviation and aerospace engineering applications. They present an opportunity for reinforcing lightweight composite materials, enhancing their stiffness and strength. Notably, auxetic materials are under consideration for applications in energy-absorbing systems within airplane seats and interiors, potentially improving crashworthiness. Additionally, their exceptional compression resistance and stress distribution make them viable candidates for integration into wing and fuselage components, contributing to improved aerodynamics and fuel efficiency.

Unlocking the potential of auxetic materials holds promise for developing structures that are not only lighter but also more resilient and safer. In the aerospace industry, these materials could revolutionize aircraft performance, safety standards, and fuel efficiency. Similarly, in the automotive sector, auxetic materials might redefine vehicle design, introducing stronger and more energy-absorbing components for enhanced crash safety.

Figure 1.6 depicts an aircraft wing with morphing airfoils filled with auxetic structures, showcasing the potential of this design concept for enhanced aeroelastic performance and vibration control. However, further research is necessary to fully explore the possibilities presented by auxetic structures integrated into morphing airfoils [57].

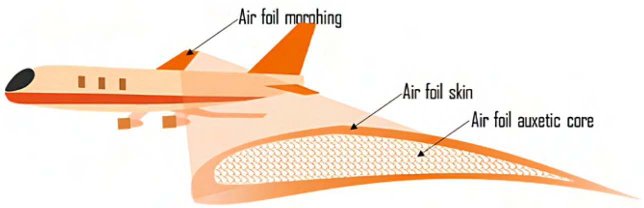

Figure 1.6: Aeronautic industry: auxetic airfoil morphing panel. Adapted from [57].

Table 1.1 provides insights into auxetic properties and the pivotal role of materials in aeronautic and aerospace components. Various components, such as curved parts, aircraft front cones, and wing panels, predominantly utilize composites and metals. Desired auxetic properties include energy absorption, synclastic curvature, compressive strength, and shear stiffness. Additionally, components like airfoils, spoilers, sandwich panels, and aircraft shafts, made of polymers, metals, and composites, require robust compressive strength and shear stiffness. Sandwich panels should exhibit good energy absorption and dissipation properties.

This research is also motivated by the exploration of additive manufacturing's untapped potential. Investigating the fabrication of auxetic structures through additive manufacturing techniques opens avenues for innovative design possibilities and material advancements.

By delving into the characterization, testing, and numerical analysis of auxetic materials, this study seeks to expand knowledge and explore unconventional applications. The motivation lies in advancing technology, enhancing safety, and optimizing performance across industries through the integration of auxetic materials. It is also driven by the recognition that auxetic materials are not well-understood, particularly in terms of numerical studies. Ultimately, this research is propelled by the conviction that auxetic materials hold the potential to reshape the future of engineering and manufacturing.

Table 1.1: Auxetic properties and material's significant role in aeronautic and aerospace industries. Adapted from [57].

Components	Desired Properties	Materials
Curved Parts	Energy absorption and dissipation Synclastic curvature Compressive strength Shear stiffness	Composites Metals
Aircraft Front Cones	Energy absorption and dissipation Synclastic curvature Compressive strength Shear stiffness	Composites Metals
Wing Panels	Energy absorption and dissipation Synclastic curvature Compressive strength Shear stiffness	Composites Metals
Airfoils/Spoilers	Compressive strength Shear stiffness	Composites Metals Polymers
Sandwich Panels	Energy absorption and dissipation Compressive strength Shear stiffness	Composites Metals Polymers
Aircraft Shafts	Compressive strength Shear stiffness	Composites Metals Polymers

In summary, the significance of auxetic materials spans multiple industries, including automotive, textiles, sports, safety equipment, biomedical, defense, aeronautics, and aerospace. Particularly in the aeronautics and aerospace sectors, auxetic materials present substantial promise. However, further research and development are essential to fully exploit their potential in this field.

1.2 Objectives

This dissertation aims to perform an extensive and comprehensive research on auxetic structures, in addition to further selection, manufacturing, experimental and numerical testing, and analysis of an auxetic structure. To achieve the described objectives, the following tasks must be fulfilled:

- Provide an in-depth examination of advanced structures, particularly those utilized in aeronautical and aerospace applications, including Fiber-Reinforced Polymers (FRPs) and sandwich composites.
- Conduct a thorough exploration of auxetic materials, emphasizing their unique properties and significance within the aerospace and aeronautics industries.
- Perform a comprehensive analysis comparing the properties of auxetic materials with conventional counterparts, highlighting distinctive characteristics.
- Examine various cellular auxetic structures, select a specific structure for detailed study, and justify the adopted additive manufacturing process.
- Detail the selection process of materials for sample fabrication, elucidate the rationale behind material choices, and conduct a thorough characterization.
- Explore the intricacies of the manufacturing process for specimens and samples, providing insights into the fabrication methodology.
- Conduct a diverse array of tests on fabricated specimens and samples, elucidating the testing procedures.
- Employ the results of experimental characterization to validate the mechanical behavior of the selected material in numerical simulations.
- Employ finite element methods for conducting numerical simulations on an auxetic structure.
- Analyze and interpret the results obtained from both experimental and numerical tests, including comparisons with existing literature.

1.3 Dissertation Outline

This dissertation work is structured as follow:

- Chapter 1, **Introduction**, offers an overview of auxetic materials, emphasizing their significance in the aerospace and aeronautics industries. The discussion underscores the pivotal role of composites and explores the potential enhancements achievable through the integration of auxetic materials. The chapter delves into the properties of these materials, highlighting their applications and contextualizing the importance of this study. Additionally, the chapter accentuates the novelty and innovation associated with the topic.
- Chapter 2, **State of the Art**, conducts an in-depth exploration of auxetic material properties in comparison to conventional materials. It critically examines various

cellular auxetic materials and structures, elucidating the selection criteria for the specific structure studied, the S-shaped structure. The chapter also addresses different additive manufacturing processes, providing a rationale for the chosen method.

- Chapter 3, **Experimental Procedure**, divided into three sections, first details the material chosen for sample fabrication, justifying the selection and explaining the necessity of material characterization. It further outlines the manufacturing process and presents the results. The second section provides insight into specimen and sample testing procedures, describing the tests conducted and the equipment utilized. The final section offers results from the characterization of the selected material.

- Chapter 4, **Numerical Procedure**, outlines the procedures and methodologies employed in numerical simulations. It begins by explaining the finite element method used and subsequently focuses on two crucial aspects: initial simulations validating the mechanical behavior of the adopted material within the models, and subsequent simulations of an auxetic structure's behavior.

- Chapter 5, **Results and Discussion**, conducts an analysis and interpretation of both experimental and numerical test results. A comparative discussion with existing literature is also presented.

- Chapter 6, **Conclusions and Future Perspectives**, summarizes the findings derived from the dissertation work, addresses the inherent limitations within the study, proposes potential avenues for enhancing the work, delineates future research trajectories, and explores prospective applications.

Chapter 2

State of the Art

This chapter is dedicated to conducting an in-depth exploration of the fundamental properties of auxetic materials, accompanied by a comparative analysis with traditional materials. A comprehensive examination of diverse cellular auxetic materials and structures is undertaken, with a focus on elucidating their respective advantages, disadvantages, and relevant research studies. Additionally, the chapter delves into an exploration of various additive manufacturing processes, with a particular emphasis on Fused Filament Fabrication (FFF), which is commonly employed in the manufacture of the specific types of auxetic structures discussed in this study.

2.1 Auxetic Properties

As previously stated in Chapter 1, auxetic materials demonstrate a counter-intuitive deformation behavior, which provides them with several advantages over conventional materials. The most notable characteristics of auxetic materials are examined in this Section.

2.1.1 Shear Strength

In contrast to regular materials, auxetic materials exhibit greater resistance to shear forces. The classical theory of elasticity for three-dimensional isotropic solids states that a body's elastic behavior can be defined by two of four constants: the Young's modulus (E), the shear modulus (G), the bulk modulus (k), and the Poisson's ratio (ν). Equations 2.1 and 2.2 describe the interrelation between these constants in three-dimensional cases.

$$G = \frac{3k(1-2\nu)}{2(1+\nu)} \quad (2.1)$$

$$G = \frac{E}{2(1+\nu)} \quad (2.2)$$

The previous Equations demonstrate that a lower Poisson's ratio results in a higher shear modulus, indicating greater resistance to shear forces [58]. As auxetic materials possess a negative Poisson's ratio, they exhibit enhanced shear strength.

2.1.2 Indentation Resistance

In non-auxetic materials, indentation causes local compression of the material under the load. To counteract this pressure, the material expands perpendicularly to the applied force [59], as illustrated in Figure 2.1(a). In contrast, isotropic auxetic materials exhibit local contraction in response to the same compression. This results in material flowing into the immediate impact area and accumulating beneath the indentor, as shown in Figure 2.1(b). This accumulation forms a denser region of the material with higher resistance to indentation [60]. As a result, auxetic materials demonstrate superior indentation resistance compared to conventional materials [58].

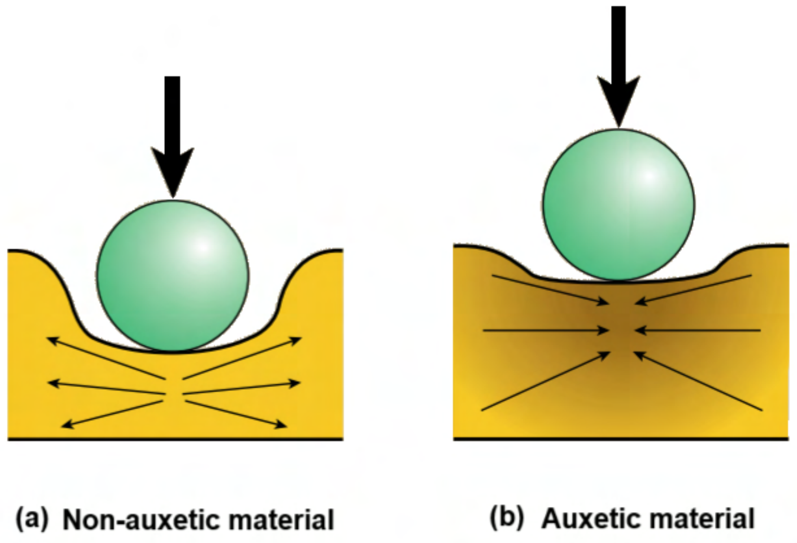

Figure 2.1: Indentation behavior: (a) non-auxetic material; (b) auxetic material. Adapted from [61].

In accordance with the classical theory of elasticity, the hardness (H) of a material is closely related to its indentation resistance, which can be expressed as a function of the Poisson's ratio using Equation 2.3.

$$H \propto \left[\frac{E}{(1-\nu^2)}\right]^{\gamma} \quad (2.3)$$

where E is the Young's modulus, ν is the Poisson's ratio of the base materials and γ is assumed to be 1 or 2/3 in the scenario of uniform pressure distribution or hertzian indentation, respectively.

According to Equation 2.3, as ν approaches -1, the hardness of the material increases toward infinity [62]. For three-dimensional isotropic solids, the maximum value of ν is 0.5, resulting in a lower resistance to indentation. In contrast, for two-dimensional isotropic systems, the maximum value of ν is 1, indicating infinite hardness as well [63].

Argatov et al. [46] conducted initial theoretical investigations on indentation and impact analyses of auxetic materials. Coenen et al. [64] reported a greater resistance to indentation in auxetic laminates with smaller and more localized damage regions for the two indentors with larger diameter, where delamination was identified as the main failure mechanism. Dirrenberger et al. [65] explored the effective elastic properties of auxetic microstructures using numerical simulations of cylindrical and spherical elastic indentation tests. Their findings suggested that, under specific conditions, auxetic materials exhibit superior indentation strength compared to honeycomb cells.

2.1.3 Fracture Toughness

Materials possessing NPR are known to exhibit superior fracture toughness compared to conventional materials [44]. Moreover, they have low crack propagation [45], as confirmed by Donoghue et al. [66], who stated that more energy is required to propagate a crack in NPR materials than in traditional materials. Therefore, such materials are less susceptible to fracture [58].

In the field of crack growth, various investigations have been conducted on both auxetic and non-auxetic foams. Re-entrant foams were observed to exhibit greater fracture toughness with increasing volumetric compression in analytical and experimental studies. Yang et al. [67] reported that auxetic composites possess almost double the fracture toughness of conventional composites. The fundamental concept of auxetic materials accounts for this behavior. When subjected to tensile loading, these materials expand in size, as confirmed macroscopically. However, the apparent growth is simply the result of each auxetic cell's dimensional increase. Consequently, whenever a crack occurs, the cells' growth tends to close it [58].

2.1.4 Synclastic Behavior

Synclastic behavior refers to the ability of a body to deform into a dome shape when subjected to bending [68]. When a body is bent, it experiences both tensile and compressive stresses, as per fundamental material mechanics. When subjected to an out-of-plane bending moment, conventional materials exhibit a saddle shape, as depicted in Figure 2.2(a). However, auxetic materials expand on the outside and contract on the inside when bent, leading to a dome-shaped structure, as depicted in Figure 2.2(b). This unique characteristic is highly desirable [69] as it enables the creation of complex structures without the need for harmful procedures or additional machining [70], which are typically necessary to achieve such shapes.

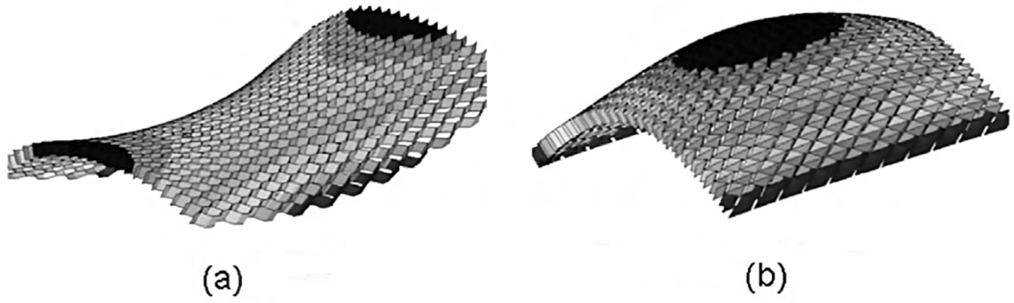

Figure 2.2: Deformation patterns for non-auxetic and auxetic materials under out-of-plane bending: (a) saddle shape (non-auxetic); (b) dome-shape (auxetic). Adapted from [71].

2.1.5 Variable Permeability

Most well-known auxetic materials possess porous microstructures. During compressive and tensile deformation, the pore sizes of these materials can change. As a result of this behavior, it is possible to claim that these structures have variable permeability. This property makes auxetics promising for filter applications [72]. Figure 2.3 illustrates this type of behavior.

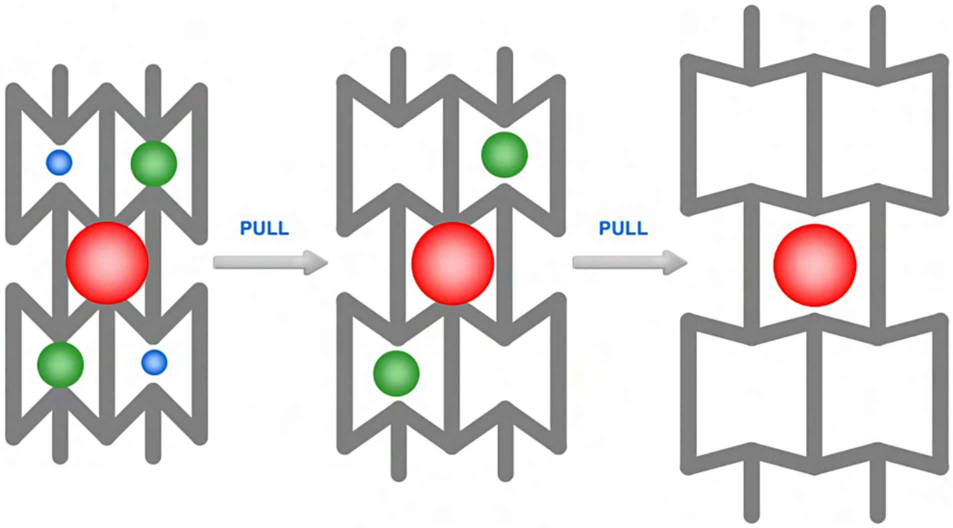

Figure 2.3: Smart filters to demonstrate the variable permeability: blue - small pores; green - medium pores; red - big pores. Adapted from [73].

Alderson et al. [74] conducted pioneering research demonstrating the improved filter performance of auxetic materials across macro-scale to nano-scales, attributed to their unique pore-opening properties and characteristics. Subsequently, in an extension of their earlier work, Alderson et al. [75] performed glass bead transmission tests on auxetic polyurethane foams. They confirmed the advantages of using auxetic materials in mass transport applications, highlighting that auxeticity persists in three-dimensional (3D) macro-scale filters and 3D sieves with significant tortuosity in the pore structure.

2.1.6 Energy Absorption

Auxetic materials are known to exhibit superior energy absorption compared to conventional materials, which translates into increased sound absorption and damping. The sound absorption capabilities of NPR foams are determined by their pore size, and previous research has explored this topic extensively [57]. For instance, Chen et al. [76] found that increasing the hierarchical level n in hierarchical honeycomb materials improves specific energy absorption due to the stress/strain law and deformation energy. The term level n refers to the hierarchical structure's level or order. Yang et al. [77] investigated the ballistic resistance of sandwich panels with aluminum foam and auxetic honeycomb cores and found that the auxetic-cored panel outperformed the aluminum foam-cored panel in ballistic resistance due to increased material concentration at the impacted location caused by auxetic behavior. Other studies have shown that auxetic foam-filled tubes and composite panels exhibit superior crashworthiness and blast-resistance performance compared to conventional materials, as demonstrated by Mohsenizadeh et al. [78], Imbalzano et al. [49, 79], and Qi et al. [80]. Lastly, Scarpa et al. [81] found that iron particle-seeded auxetic polyurethane foam had intrinsically higher acoustic absorption properties than standard open-cell foams.

Energy absorption structures have various applications, including crash-worthy structures such as cars, bullet-proof vests, and transport packaging. As previously stated, auxetic materials have been found to exhibit good energy absorption properties [82].

2.1.7 Shape Memory

Shape memory refers to the capacity of a material to recall and revert to its original shape and dimensions after undergoing a plastic or semi-plastic deformation when exposed to a particular thermal stimulus [83, 84]. In the context of auxetic foams, research has shown that they can be converted from auxetic to non-auxetic and vice versa multiple times without compromising their mechanical properties [85]. This conversion process was obtained using a purpose made mould composed by cylinders backed by pistons to impose axial compression on the foams. The conversion process applied to the foams involved the imposition of a combined axial and radial compression, followed by heating until the softening temperature is reached [86]. This feature is particularly advantageous in scenarios where temperature variations require materials with changing mechanical properties [87, 88].

2.2 Cellular Auxetic Materials and Structures

As mentioned in Chapter 1, the auxetic properties of materials or structures are primarily determined by their geometrical configuration. The size of these structures can range from micro to macro [89], and they can be categorized as two-dimensional (2D) or three-dimensional (3D). Initially, there was extensive research on 2D structures and models. The most significant classes of 2D auxetic structures include re-entrant honeycombs [90], chiral and anti-chiral structures [91], rotating rigid/semi-rigid units [92], and double arrowhead structures [93]. With advances in additive manufacturing technology, three-dimensional models have been proposed and investigated, mostly developed from 2D auxetic structures [94].

The following sections present a detailed analysis of certain models of cellular auxetic materials and structures, aimed at emphasizing their unique properties resulting from variations in their geometrical configuration.

2.2.1 Re-entrant Models

Gibson et al. [95] introduced the conventional re-entrant cellular structure in the form of re-entrant honeycombs for the first time. Subsequently, Masters et al. [96] proposed an auxetic behavior based on the traditional 2D re-entrant structure. Under a tensile load applied in the horizontal direction, the re-entrant sides stretch out while the diagonal ribs move outward [96], causing the re-entrant vertices to displace laterally. Consequently, the neighboring cell undergoes vertical expansion through neutral cell ribs that latch onto the vertices [57], as illustrated in Figure 2.4. However, bending of the diagonal ribs is inevitable in most honeycombs with re-entrant cellular configuration [72].

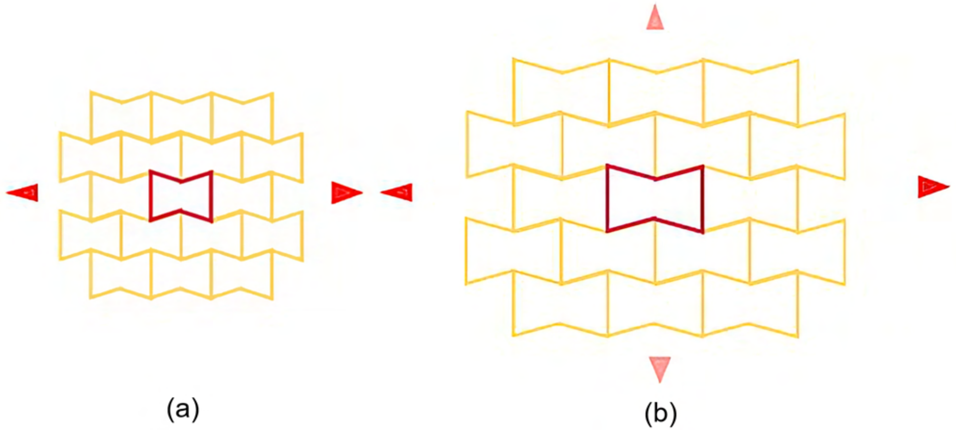

Figure 2.4: Representation of a 2D re-entrant honeycomb structure: (a) undeformed condition; (b) deformed condition. Adapted from [57].

A variety of 2D re-entrant structures are illustrated in Figure 2.5, including the chiral quadratic lattice structure, structurally hexagon re-entrant honeycomb [97], square rib missing model, and lozenge missing rib model. These structures can be formed by systematically arranging the patterns [57].

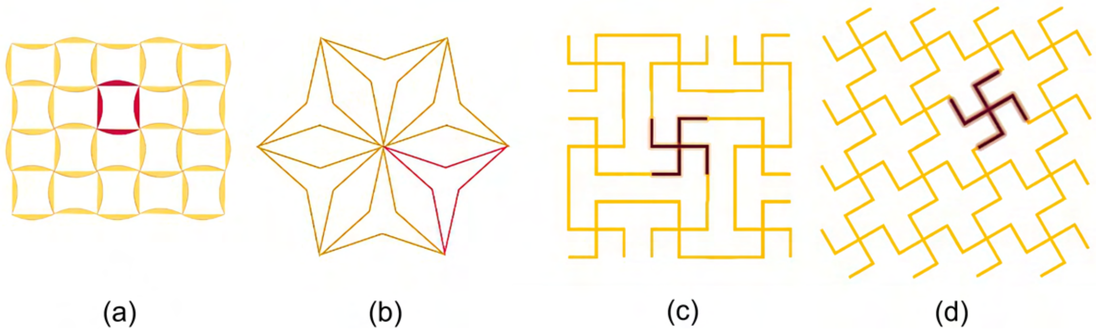

Figure 2.5: Other re-entrant structures: (a) chiral quadratic lattice structure; (b) structurally hexagon re-entrant honeycomb; (c) square rib missing model; (d) lozenge missing rib model. Adapted from [57].

In the field of auxetics, certain 2D re-entrant structures can be transformed into 3D structures [56]. Evans et al. [98] reported the first orthotropic 3D re-entrant honeycomb auxetic structure. Further analytical research conducted by Yang et al. [99] revealed that mechanical properties of 3D re-entrant honeycomb auxetic structures could be controlled by the characteristic strut length, ratio, and re-entrant angle. With the advancement of fabrication processes such as additive manufacturing, more complex configurations arose based on pre-existing auxetic structures. Figure 2.6(a) provides a depiction of the general layout of a 3D re-entrant honeycomb construction, while Figure 2.6(b) portrays a three-dimensional re-entrant arrowhead structure and Figure 2.6(c) illustrates a 3D chiral quadratic re-entrant lattice structure. These structures represent only a few among many possible variations of the re-entrant honeycomb configuration.

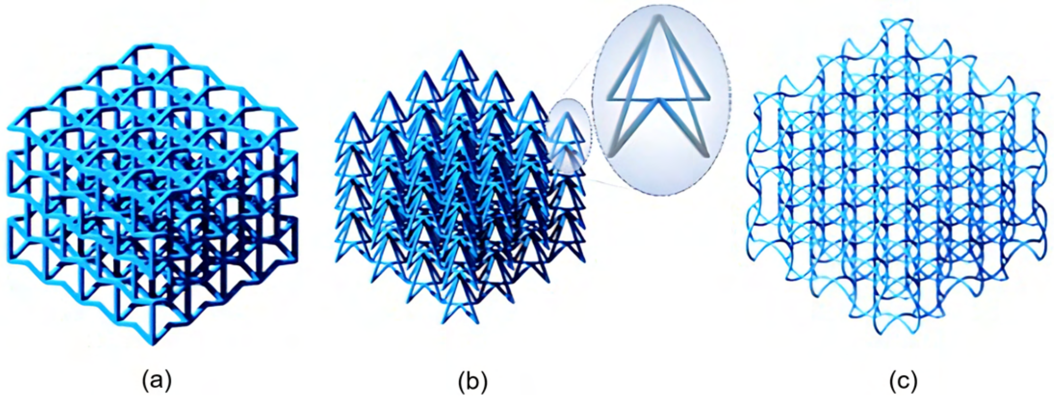

Figure 2.6: Illustrations of 3D re-entrant structures: (a) 3D re-entrant honeycomb structure; (b) 3D arrow re-entrant structure; (c) 3D chiral quadratic re-entrant lattice structure. Adapted from [57].

Grima et al. [100] investigated the mechanical properties of star-shaped structures with rational symmetry of order 3, 4, or 6 using the Empirical Modelling Using Dummy Atoms (EMUDA) technique, as shown in Figure 2.7. The study demonstrated that these structures could exhibit auxetic behavior and that the magnitude of Poisson's ratio can be controlled by adjusting the stiffness of the hinges and rod elements. Additionally, their study showed that the EMUDA technique is a useful tool for exploring the behavior of periodic structures under applied loads and distinguishing between auxetic and non-auxetic systems.

Auxetic re-entrant models present both advantages and disadvantages. Their high porosity or low density is advantageous for small-sized structures. However, re-entrant structures are composed of intricately latched thin struts, making precise and defect-free creation challenging. Due to their complex interior cavities, 3D re-entrant structures require the adoption of additive manufacturing processes. Furthermore, auxetic movement is impeded by thin rib displacement and flexure. Additionally, small ribs are susceptible to fatigue damage, ultimately reducing the overall durability of the construction [57].

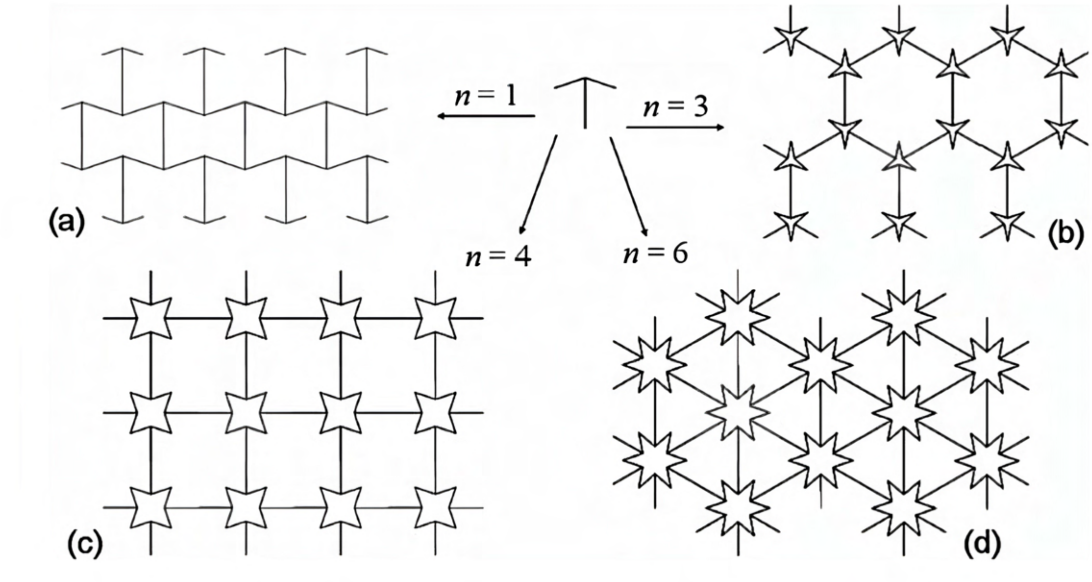

Figure 2.7: Various star-shape systems with different rotational symmetry of order: (a) auxetic honeycomb; (b) star-3 system; (c) star-4 system; (d) star-6 system. Adapted from [100].

Re-entrant structures are frequently utilized in the core of lightweight sandwich structures, particularly in applications such as aeronautical components [101]. As an example, Lira et al. [102] explored gradient cellular auxetics as prospective cores for aeroengine fan blades.

2.2.2 Rotating-Rigid Units

The rotating-rigid unit is a prevalent type of auxetic model that has been explored by Grima [92, 103], Alderson et al. [104], and Rafsanjani et al. [105]. The basic geometry of rotating-rigid units comprises squares that are linked at vertices. Figure 2.8 illustrates the unit cell of this mechanism. When these structures are subjected to loads, the squares tend to rotate, causing either expansion or contraction, depending on the type and direction of the applied load.

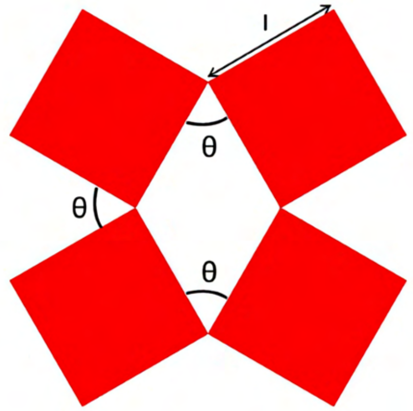

Figure 2.8: Unit cell of rotating square model. Adapted from [72].

Apart from the rotating square model, Grima [92] conducted a theoretical analysis of the rotating square model and suggested that the rotating triangle mechanism could be an effective approach for introducing NPRs into actual materials. In a subsequent work, Grima et al. [106] presented a more general auxetic model of rotating rectangles, as squares are a special case of rectangles. Grima et al. [103] also conducted another study focused on rotating polymeric models.

Under deformation conditions, the series of stiff squares with a Poisson's ratio of -1 may suggest that the model is susceptible to collapsing and changing its aspect ratio. If the rotating units are connected by a semi-rigid formation, the Poisson's ratio will vary and is primarily determined by the rigidity of the rotating units relative to the stiffness of the links and the direction of applied loading [57].

2.2.3 Chiral Models

Chiral models represent another extensively researched type of cellular auxetic material. The term "chiral" refers to a molecule that is non-superimposable on its mirror image [72]. The first proposal for an auxetic chiral configuration based on rotating disks and nearest neighbor inverse *n*th power interactions was made by Wojciechowski [107]. Additionally, Prall and Lakes [108] introduced a chiral honeycomb that has a theoretical in-plane Poisson's ratio of -1.

The hexagonal chiral honeycomb can be constructed from chiral units. These chiral units consist of a central cylinder, also known as a central node, and ligaments attached tangentially [91]. The number of chiral units can range from 3 (tri-chiral) to 6 (hexa-chiral) depending on the geometric arrangement of ligaments per unit cell, as depicted in Figure 2.9. The fundamental chiral unit cell can be assembled by arranging ligaments on either side. The chiral or anti-chiral properties can be achieved through these arrangements, with anti-chiral structures possessing reflective symmetry. By interlocking the ligament on the same side across the core, a geometrical network with anti-chiral symmetry can be generated.

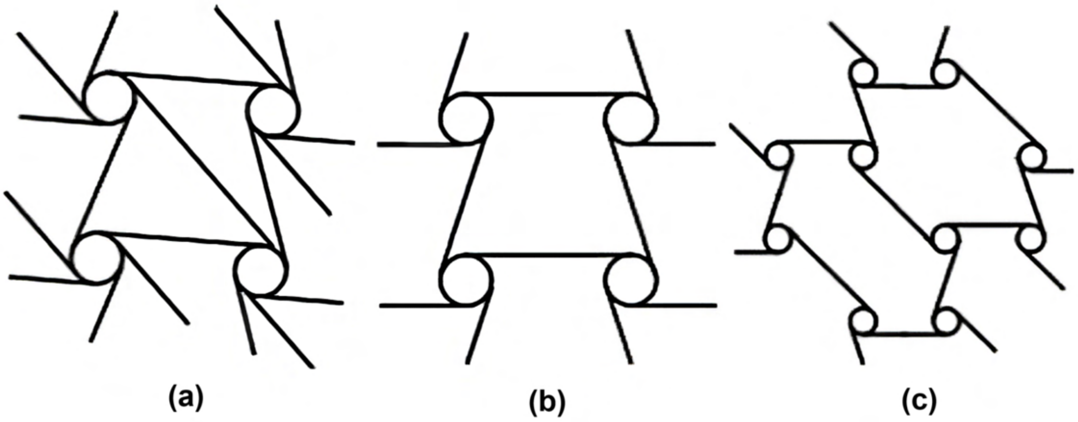

Figure 2.9: Meta-chiral systems with different number of ribs attached to each node:(a) six ribs; (b) four ribs; (c) three ribs. Adapted from [91].

In chiral structures, the application of mechanical loads results in flexible folding or unfolding of the chiral unit due to the spin of the core cylinder. The folding mechanism of chiral structures is illustrated in Figure 2.10. The deformation of chiral structures is primarily caused by core cylinder spin and ligament deformation [109]. When nodes experience compression or stretching forces, they spin in-plane, causing the linked ligaments to flex [110].

Lightweight chiral materials and designs have the potential to achieve impact energy absorption, vibration reduction, acoustic performance, electromagnetic stealth, thermal insulation, and zero thermal expansion. Chiral mechanical metamaterials also offer wave mitigation properties and adjustable energy band gap properties through local node spin and ligament bending deformation, as well as elastic energy storage generated by localized resonances, which can be utilized for their broadband passive energy damping capabilities [57].

Gatt et al. [111] conducted a noteworthy study on auxetic chiral models in which they examined the mechanical properties of the general forms of the flexing anti-tetrachiral system using analytical and finite element methods. The study found that the geometry and material properties of the constituent materials have a significant impact on the mechanical properties of the flexing anti-tetrachiral system. Specifically, the length-thickness ratio of the ligaments affects the Poisson's ratio of the general flexing anti-tetrachiral. Gatt et al. [111] also concluded that the rigidity of the anti-tetrachiral system can be adjusted without affecting the Poisson's ratio by modifying the relative stiffness of the ligaments. In a subsequent study, Gatt et al. [112] used the finite element approach to investigate the connection between the nodes and ligaments in the anti-tetrachiral structure. The study found that the amount of adhesive used to attach the ligaments to the node has a negligible effect on the Poisson's ratio but a significant impact on the stiffness of the structure. Additionally, the stiffness of the adhesive affects the chiral system's mode of deformation.

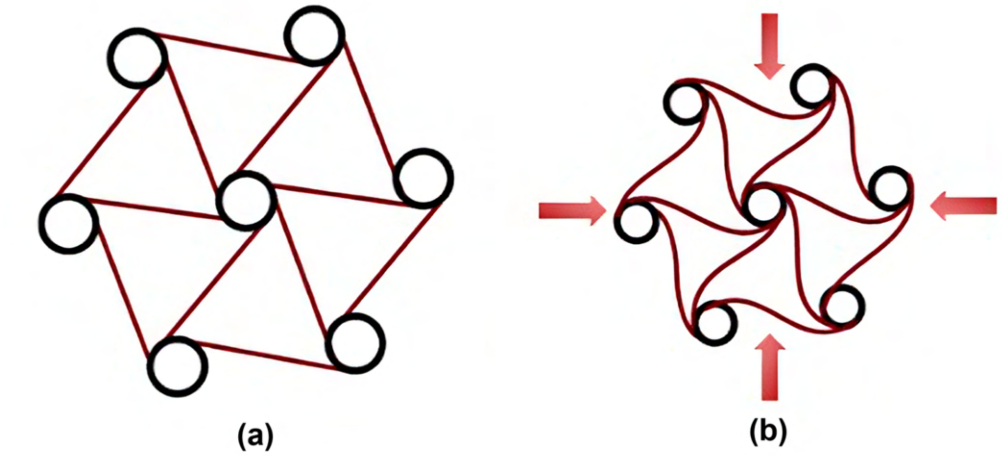

Figure 2.10: Hexachiral unit deformation: (a) relaxed; (b) completely deformed. Adapted from [57].

Rossiter et al. [113] introduced an innovative study that showcased a new shape memory auxetic deployable chiral structure capable of deformation without requiring an external actuation mechanism. The structure employed shape memory alloy beams that transformed from their programmed curled shape to straight beams upon heating, leading to significant overall expansion.

In recent years, chiral models have been the subject of extensive research, particularly for their potential use in morphing structures. Airoldi et al. [114, 115] constructed chiral honeycombs from thin composite laminates with morphing ribs for a variable camber wing box. Bornengo et al. [116] proposed a hexagonal chiral honeycomb concept as a truss-like internal structure for adaptable wing box shapes. Budarapu et al. [117] developed a framework to design an aircraft wing structure and analyze a chiral morphing airfoil. Gong et al. [118] suggested a unique honeycomb structure with zero Poisson's ratio, capable of achieving deformations along two orthogonal directions while maintaining effective stiffness in the morphing direction. Figure 2.11 depicts five chiral models that can be derived from the fundamental chiral unit.

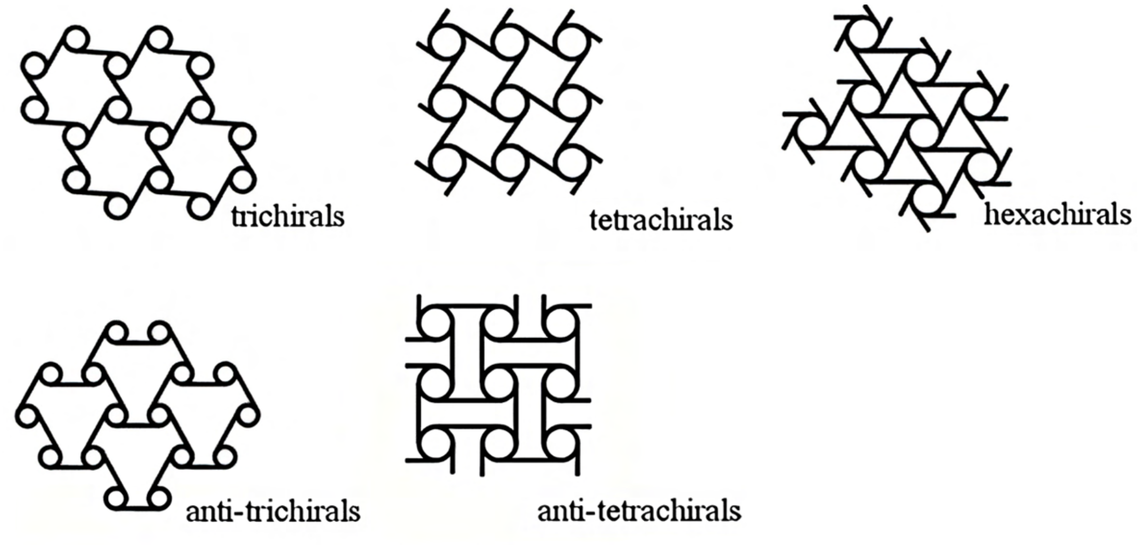

Figure 2.11: Five tessellations that may be obtained from the chiral basic units. Adapted from [91].

2.2.4 S-shaped Structure

In a recent study conducted by Meena and Singamneni [119], a novel structural concept was introduced, characterized by an "S"-shaped unit cell, as depicted in Figure 2.12. The geometrical parameters that describe this unit cell are outlined in Table 2.1. As previously discussed, auxetic geometries fall into three primary categories such as re-entrant, chiral, and rotating models. The "S" structure, in its deformation patterns, aligns with those of a node-ligament based chiral structure, achieving its auxetic behavior through rotation and thereby qualifying as a chiral model.

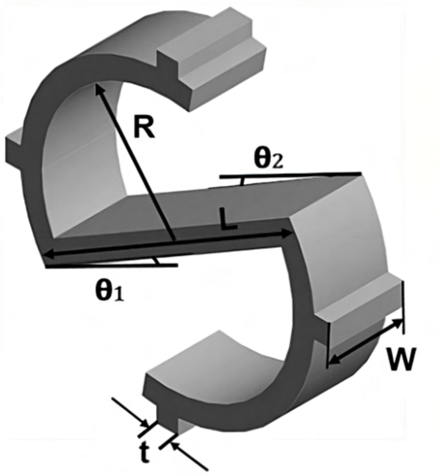

Figure 2.12: S-shaped unit cell. Adapted from [119].

Table 2.1: Significant geometrical parameters of the S-shaped unit cell. Adapted from [119].

L (mm)	R (mm)	θ_1 , θ_2 (º)	t (mm)	W (mm)
14	7	30	1.5	10

The motivation behind this unique structure stemmed from design challenges associated with the sharp corners and joints prevalent in conventional auxetic configurations. A higher number of joints increases the potential for stress concentration points and increases the risk of structural failure due to critical stress concentrations at these locations. Xiong et al. [120] explored the impact of the fillet radius, on re-entrant structures and found that increasing the fillet radius could mitigate the effects of stress concentration. In Figure 2.13 is shown a modified re-entrant NPR unit cell with inclined links and fillets studied by Xiong et al. [120]. Building on this insight, Meena and Singamneni [119] developed the "S" unit cell configuration, aiming to achieve auxetic responses similar to re-entrant forms while mitigating stress concentration phenomena.

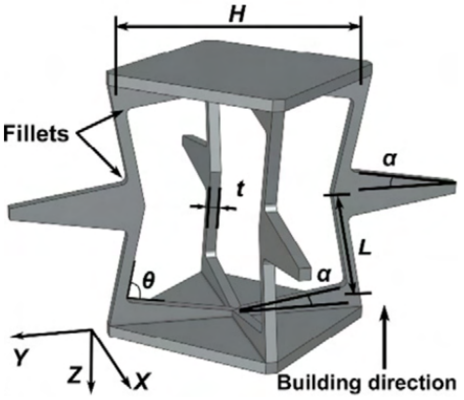

Figure 2.13: Modified re-entrant NPR unit cell with inclined links and fillets. Adapted from [120].

Their study involved both experimental and numerical comparisons between the "S" structure and the re-entrant configuration. For numerical analysis, computer-aided design (CAD) models of both structures were designed, and Finite Element Analysis (FEA) was conducted using commercial finite element software. The "S" structure was optimized numerically by adjusting geometric parameters to balance negative Poisson's ratios and von Mises stresses under loading conditions. The FEA mesh consisted of uniform tetrahedral elements with a size of 0.50 mm. Boundary conditions for compression simulations included a face-fixed constraint at one end and a compressive load applied at the opposite face. Material properties of stainless steel 316L were considered, with linear and non-linear material models represented by linear and bi-linear curves, respectively. Displacements of -0.1 and -4 mm were applied to linear and non-linear materials, respectively.

For experimental analysis, selective laser melting was used to fabricate models of both structures using stainless steel 316L. Mechanical compression tests were conducted, applying compressive loads to achieve a maximum displacement of 20 mm at a rate of 2 mm/min over a duration of 10 minutes. The entire compression process was recorded, and subsequent image analysis in ImageJ software facilitated the measurement of lateral and longitudinal displacements, which were then converted to strains to determine Poisson's ratios.

Observing the experimental results in Figure 2.14, Meena and Singamneni [119] noted that the "S" structure deformed through the rotation of its inclined struts, creating a virtual circular path. The curved portions and columns of the middle rows of unit cells moved toward their respective inclined struts to close the gaps between them. As they attempted to fill these gaps, the struts widened the space between the curved and inclined parts of the corner unit cells due to the pulling effect from adjacent cells. Ultimately, as the gap between the curved part and the inclined strut of the unit cells closed, the entire structure collapsed inwards rather than deforming sideways.

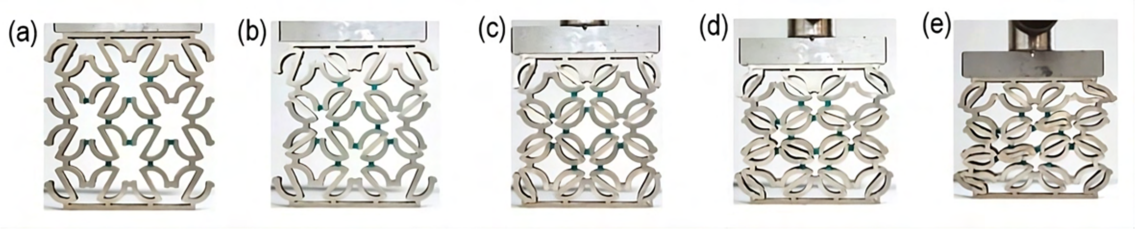

Figure 2.14: Sequence of pictures for applied displacement of "S" structures: (a) 0 mm; (b) 5 mm; (c) 10 mm; (d) 15 mm; (e) 20 mm. Adapted from [119].

Analyzing the stress-strain curves for the "S" structure, it was observed that stress increased almost linearly with strain in the elastic region. When plastic deformation began, some waviness appeared, but stress continued to rise steadily with increasing strain. At around 20% strain, the structure was nearly compressed to its limits, and further stress increase ceased as the struts approached a densely packed and distorted state. Mechanical properties were determined, including Young's modulus of 635 MPa and an ultimate tensile strength of 37 MPa. Notably, Poisson's ratio was consistently negative across all deformation levels, with greater negativity at lower deformation values. The loss of auxeticity in the structures was attributed to the densification and collapse of the struts over time. It was observable that the S-shaped structure is characterized by the unit cells working together to resist the loads.

Meena and Singamneni's [119] global findings revealed that the S-shaped auxetic structure has diminished stress concentration effects, simultaneously exhibiting enhanced auxetic responses. It was also highlighted several key points, such as:

- The deformation responses of the S-shaped auxetic structure surpassed those of the re-entrant structure, with no occurrence of cracking or failure within the elements of the structure;
- Re-entrant structures exhibited lateral displacement and row-wise collapsing, while the S-shaped unit cells shared deformation uniformly across the structure;
- The S-shaped structures displayed more prominent negative Poisson's ratios, with values around -1.75 in the elastic range, and they maintained their auxetic nature up to almost 15% of externally applied strain. In contrast, the re-entrant form only reached a maximum of approximately -1.2 for the Poisson's ratio, and its auxetic responses diminished within 5% of external strains;
- Concentrated stress levels were higher in re-entrant structures, reaching up to 2.5 times for linear and 1.9 times for non-linear loading cases compared to stresses generated in "S" structures;
- The average Poisson's ratio absolute values obtained through numerical simulations slightly lower from those obtained from experimental responses;
- The auxeticity of the "S" structure (Negative Poisson's Ratio) gradually diminished as strain levels increased.

Given the distinctive nature and unique properties of the S-shaped structure, a decision was made to conduct a more detailed investigation into this particular structure. The intricacy of this design poses challenges for conventional manufacturing processes in achieving the desired structure. Consequently, a comprehensive examination of various manufacturing methods, with a particular emphasis on additive manufacturing processes, is essential. This scrutiny aims to determine the most suitable manufacturing approach for producing the sample designated for in-depth study.

2.3 Additive Manufacturing (AM)

Manufacturing is the intricate process of converting raw materials into finished or semi-finished products on a large scale. The approach entails utilizing various methodologies, human labor, and equipment, depending on the desired final product. Evolving due to industrial, economic, and technological shifts, manufacturing industries are in perpetual pursuit of refining techniques to reduce costs and energy consumption, and to broaden their capabilities. Several manufacturing processes are traditionally employed in production. Subtractive technologies, remove material through methods such as machining, drilling, or grinding. Formative methods, like casting injection or extrusion, shape materials into desired forms. Additionally, joining techniques, such as welding, riveting, or gluing, are also extensively used. These well-established methods are quality-assured and widely implemented in commercial contexts. Conversely, AM, commonly known as “3D printing”, employs innovative technology to construct intricate shapes by layering material to form a part [121]. Figures 2.15 and 2.16 present a concise overview of the different additive manufacturing technologies, different types and processes.

Originating in the 1960s, AM has experienced rapid and continuous growth, introducing novel techniques that expand manufacturing capabilities and redefine conventional approaches. The current focus within research and industry lies in identifying opportunities where AM can either supplant existing manufacturing systems or create entirely new ones [121]. Notably, the material extrusion method, in which is included Fused Filament Fabrication (FFF), has gained prominence as a popular AM process, due to its wide avaliability and low cost of machinery and consumables. In the context of this study, FFF is chosen to produce structural components, with detailed exploration presented in Subsection 2.3.1.

Throughout the years, a multitude of manufacturing techniques have been explored to enhance the fabrication of auxetic structures. These methods endeavor to enhance versatility and flexibility in both the design and production of auxetic structures, employing strategies such as low-cost materials, efficient designs, and streamlined structural optimization approaches. AM techniques have pioneered this endeavor, offering distinct advantages that make it a preferred manufacturing method. Noteworthy benefits include reduced material wastage, accelerated fabrication timelines, intricate and precise geometry creation, less dependence on skilled labor, and simplified design iterations, among others [123].

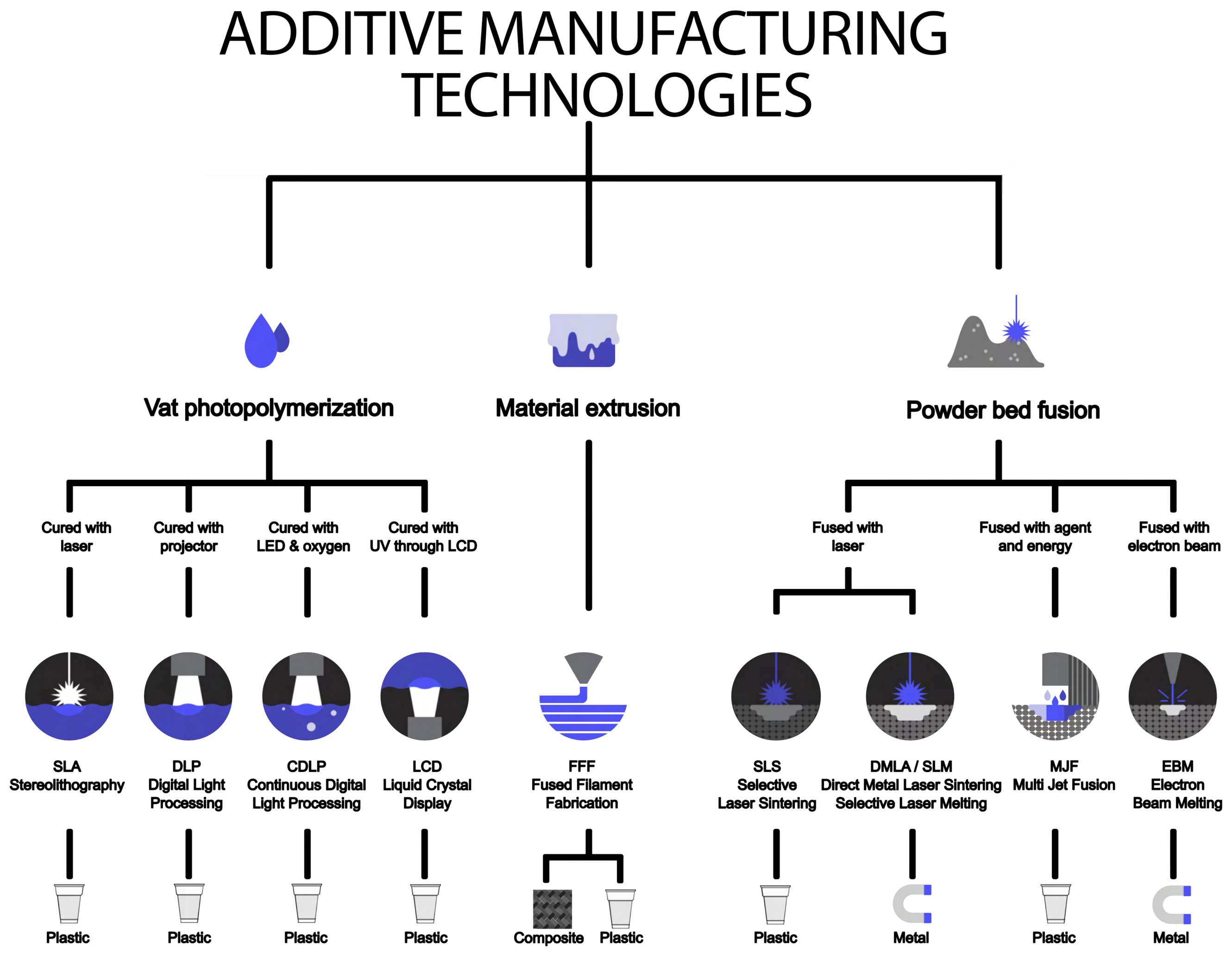

Figure 2.15: Additive manufacturing technologies: different types and processes - Part I. Adapted from [122].

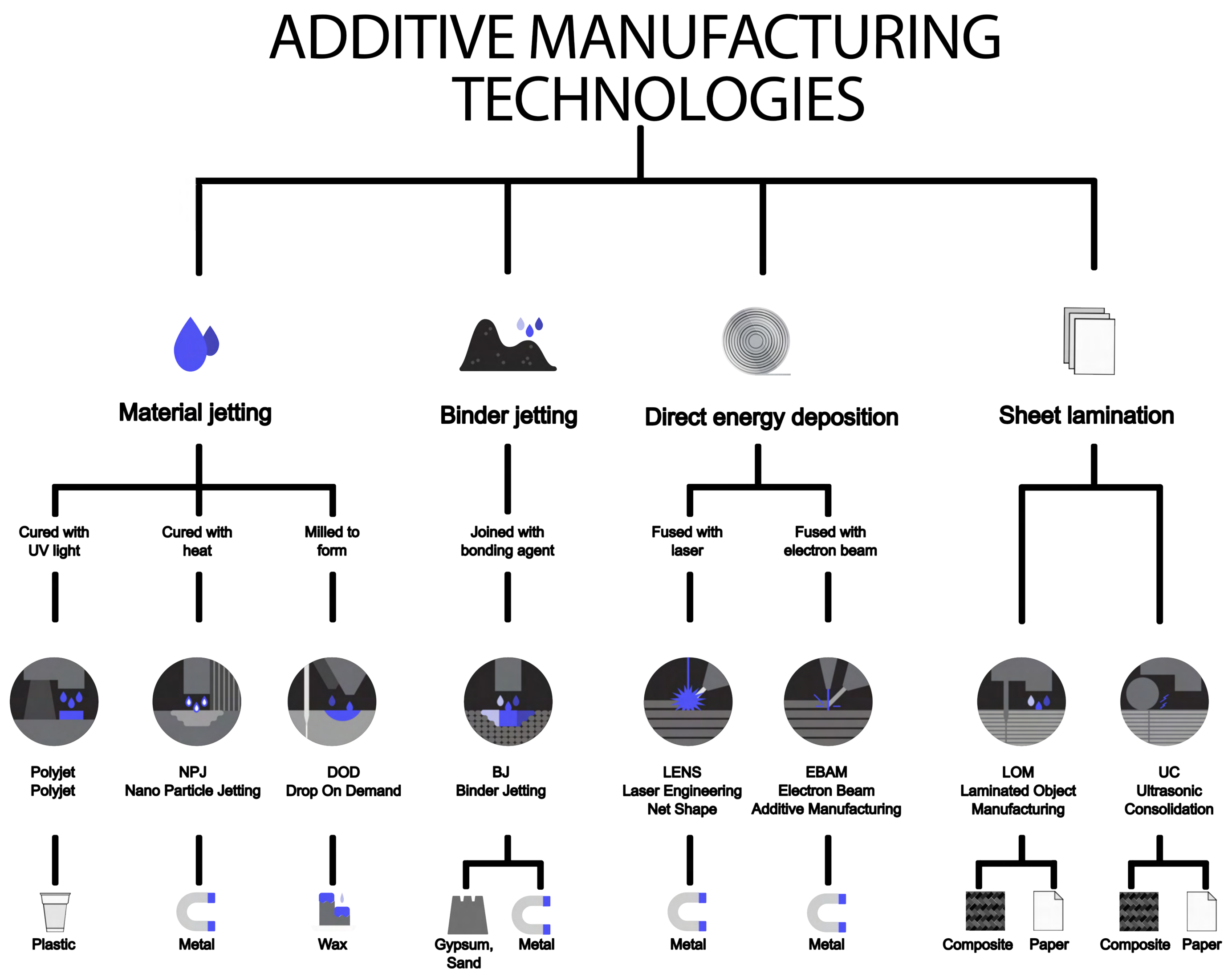

Figure 2.16: Additive manufacturing technologies: different types and processes - Part II. Adapted from [122].

2.3.1 Fused Filament Fabrication (FFF)

Fused Filament Fabrication (FFF) stands out as a prominent low cost additive manufacturing technology utilized to construct prototypes and functional components using thermoplastics. It is the most available to the common consumer and the most economical. The fundamental concept of this process involves fusing and extruding thermoplastic filament through a nozzle tip to deposit successive layers on a platform, thereby constructing parts layer by layer directly, where the process begins with a computer-aided design (CAD) model which is then translated into operational instructions via computer-aided manufacturing (CAM) software. This allows for the direct and precise creation of physical objects from the initial digital design. Given its simplicity, reliability, and cost-effectiveness, FFF has gained widespread recognition and adoption across industry, academia, and consumer domains. Additionally, the research and development sectors have extensively leveraged the FFF process to enhance its efficacy, innovate new materials, and apply FFF systems to a wide range of engineering applications [124].

FFF, a filament extrusion-based procedure, seamlessly integrates CAD and CAM systems, materials science, computer numerical control, and the extrusion process to fabricate three-dimensional parts directly from CAD models. Generally, FFF technology encompasses four distinct stages in the process of part fabrication [124]:

1. CAD modeling;
2. Preprocessing on CAM software;
3. Part construction utilizing the FFF machine;
4. Post-processing.

Initiating the process, a CAD solid model is generated in any CAD software and subsequently converted to a stereolithography (STL) format, which is a faceted approximation of the model. The STL file is then subjected to preprocessing using CAM slicing software. This preprocessing phase encompasses crucial steps such as determining the optimal part orientation within the build volume, slicing the model into thin horizontal layers, selecting pertinent printing parameters, and generating supports. Proper orientation is pivotal to minimize or eliminate support structures and enhance surface finish. For each layer, the CAM software generates "tool paths" or build instructions for the extruder to create successive layers. The CAM software generates G-code file that is transmitted to the FFF machine for the part construction phase. G-code, or Geometric Code, is a language used in computer-aided manufacturing (CAM) and numerical control (NC) to control and direct computerized machine tools and 3D printers. It consists of a series of alphanumeric codes that represent specific commands, such as movement, speed, and tool changes, guiding the machine in the fabrication of a part or object based on a digital design.

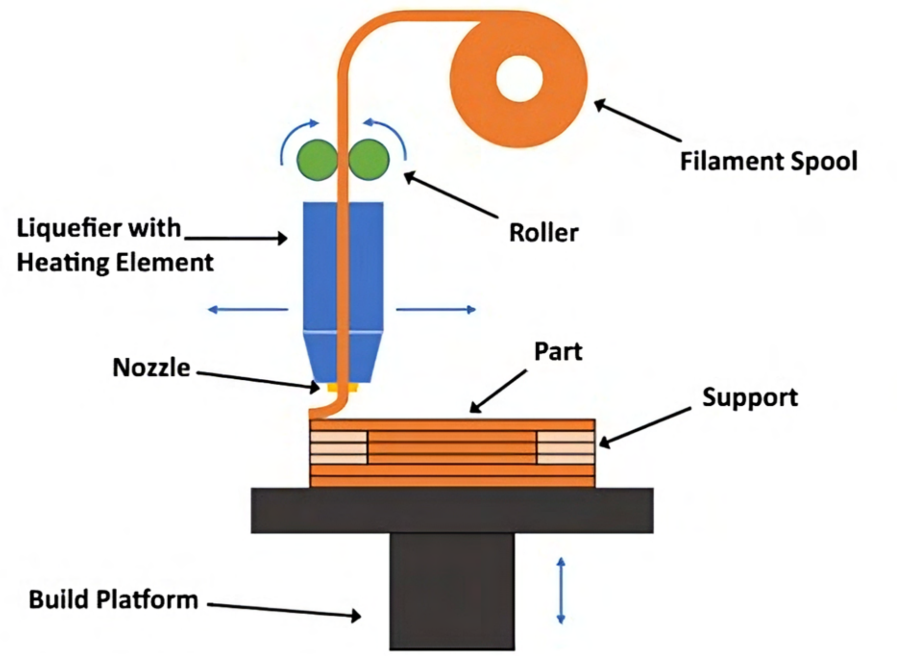

Figure 2.17: Schematic illustration of FFF process. Adapted from [125].

Within the FFF machine, thermoplastic feedstock filament is drawn from a spool into the FFF extrusion head via drive wheels. Inside the extrusion head, the filament is heated to a molten state and subsequently extruded through the orifice of a nozzle tip fitted at the bottom of the extrusion head. The schematic representation of the basic FFF process is illustrated in Figure 2.17. The controlled movement of the extrusion head, governed by computer directives, facilitates the material deposition in thin layers on a base. This layer-by-layer construction results in the solidification of the material upon deposition, ensuring its bonding to the previous layer. Post-creation, the part is ready for removal from the FFF machine with support structures, if present, either being removed by breaking them away from the part or via immersion in a solution. The accuracy and precision of the resulting part are contingent upon the process parameters, and certain advanced FFF machines offer remarkable precision and accuracy levels.

The versatility of the FFF process extends to a wide range of thermoplastic materials, including polylactic acid (PLA), butadiene styrene (ABS), polyethylene terephthalate glycol (PETG), thermoplastic polyurethane (TPU), nylon, and others. Table 2.2 provides a comprehensive overview of the properties associated with the most common feedstock thermoplastic materials employed in FFF processes.

Table 2.2: Most common feedstock materials used in FFF processes and their properties. Adapted from [126].

Material	PLA	ABS	PETG	TPU	Nylon
Ultimate Strength (MPa)	65	40	53	26-43	40-85
Stiffness (on a scale of 1 to 10)	7.5/10	5/10	5/10	1/10	5/10
Durability (on a scale of 1 to 10)	4/10	8/10	8/10	9/10	10/10
Maximum Service Temperature (^{o}C)	52	98	73	60 - 74	80 - 95
Coefficient of Thermal Expansion (μ/m-^{o}C)	68	90	60	157	95
Density (g/cm^3)	1.24	1.04	1.23	1.19-1.23	1.06-1.14
Printability (on a scale of 1 to 10)	9/10	8/10	9/10	6/10	8/10
Extruder Temperature (^{o}C)	190 - 220	220 - 250	230 - 250	225 - 245	220 - 270
Bed Temperature (^{o}C)	45 - 60	95 - 110	75 - 90	45 - 60	70 - 90
Other Hardware Requirements	Part cooling fan	Heated bed Enclosure recommended	Heated bed Part cooling Fan	Part cooling fan	Heated bed Enclosure recommended May require all metal hotend
Other Properties	Heated bed not required	Impact resistant Heat resistant	Water resistant Chemically resistant Fatigue resistant	Flexible Elastic Soft Fatigue resistant Heated bed not required	Flexible Impact resistant Heat resistant Fatigue resistant

Chapter 3

Experimental Procedure

This chapter is dedicated to providing an in-depth overview of the methodologies and processes employed during the experimental phase of this study. This chapter plays a pivotal role in elucidating the systematic approach followed throughout the experiments, encompassing three primary aspects: (i) the selection of the material and manufacturing process, (ii) the testing procedure of specimens and samples, and (iii) the subsequent material characterization. Each of these components is of significant importance in ensuring the accuracy and reliability of the experimental results. Therefore, this chapter serves as a comprehensive guide to the intricate steps involved in the experimental phase, outlining the rationale behind the material selection, the rigorous characterization process, the intricacies of sample fabrication, and the meticulous procedures for sample analysis. It lays the foundation for a thorough understanding of the empirical investigations undertaken in this study, which ultimately contribute to the generation of valuable insights and conclusions.

3.1 Material and Manufacturing Process

As mentioned before, the fabrication method selected to produce the S-shaped samples was Fused Filament Fabrication (FFF). As elaborated in Subsection 2.3.1, the predominant materials for this fabrication method include PLA, ABS, PETG, and Nylon. After a close inspection on the mechanical properties of these materials, PETG was selected due to having a good balance between mechanical properties and ease of printing when compared with PLA, ABS, TPU and Nylon. The specific PETG material utilized in the production of samples is supplied by the Tucab manufacturer, and its material properties are detailed in Table 3.1.

Given the adoption of printing parameters and displacement rates for the compression tests of the auxetic structures that are different from those adopted by the supplier for characterizing the PETG, a mechanical characterization was conducted to ascertain the properties of the employed material. For this purpose, PETG specimens were manufactured.

The manufacturing process for both the specimens and the S-shaped structure comprises three distinct stages: CAD, CAM and 3D printing. The CAD models for both specimens were developed using Autodesk Inventor Professional 2024 software. Upon the completion of the CAD models, it was necessary to convert them to the STL file format for processing in the CAM software. The CAM software used was Ultimaker Cura 5.2.1. This software was responsible for generating a G-code file, which was then saved onto a flash drive for later use with the 3D printer. A comprehensive overview of the FFF parameters employed for the printing of both models can be found in Table 3.2.

Table 3.1: Properties of PETG from Tucab manufacturer. Adapted from [127].

Property	**Standard**	**Value**
Hardeness (R-scale)	ASTM D785	110
Tensile strength (MPa) (50 mm/min)	ASTM D638	50
Stress at fracture (MPa) (50 mm/min)	ASTM D638	29
Strain at maximum stress (%) (50 mm/min)	ASTM D638	5.0
Strain at fracture (%) (50 mm/min)	ASTM D638	140
Density (g/cm^3)	ASTM D792	1.27

Table 3.2: Printing parameters adopted in the FFF process.

Parameters	**Specimens' Printing**	**Samples' Printing**
Filament diameter (mm)	1.75	1.75
Nozzle diameter (mm)	0.8	0.8
Extrusion width (mm)	0.8	0.8
Nozzle temperature (ºC)	220	220
Bed temperature (ºC)	80	80
Printing Speed (mm/s)	30	45
Layer height (mm)	0.2	0.2
Infill density (%)	100	100

The ensuing step encompassed the actual 3D printing of the models. The Artillery Sidewinder X1 printer was employed for this purpose. Calibration of the printer was crucial during this phase to address potential issues that could lead to defects in the prints. Given that PETG, the selected material, tends to exhibit challenges adhering to the print bed of the printer used on this study, an adhesive spray was employed to enhance bed adhesion before initiating print jobs. With these considerations addressed, the printer was primed for operation. The G-code file on the flash drive was linked to the printer, which then proceeded to read the file and execute the print jobs.

3.1.1 PETG Specimens

The mechanical characterization of the PETG material involved the design of Type I specimens, conforming to the guidelines specified in the ASTM D638 standard [128]. The CAD model of the specimen is visually represented in Figure 3.1. As previously detailed in the fabrication process of the PETG specimens, an exception was made with regard to the selected printing parameters within the Fused Filament Fabrication (FFF) process, as concisely summarized in Table 3.2. Specifically, this modification involved omitting the walls, top and bottom layers, and implementing a line-based infill pattern.

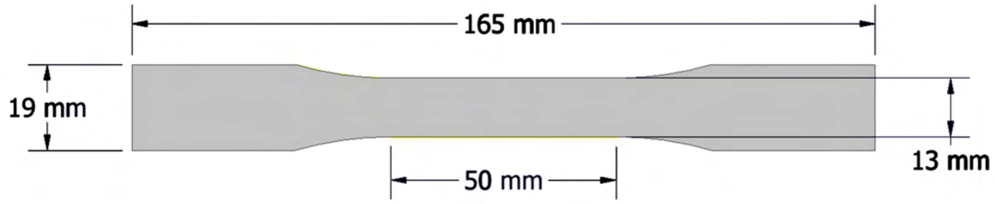

Figure 3.1: PETG specimen adopted for the material characterization: CAD model, with dimensions.

3.1.2 S-shaped Samples

Given that the primary focus of this investigation is the S-shaped structure, nine PETG samples of this structure were fabricated following the previously outlined procedure. The design of the sample's CAD model was informed by geometric characteristics consistent with those presented by Meena and Singamneni [119], as specified in Table 2.1 of Section 2.2.4. For visual reference, Figure 3.2 illustrates both the CAD model of the structure and the CAD model of the unit cell, including their respective dimensions.

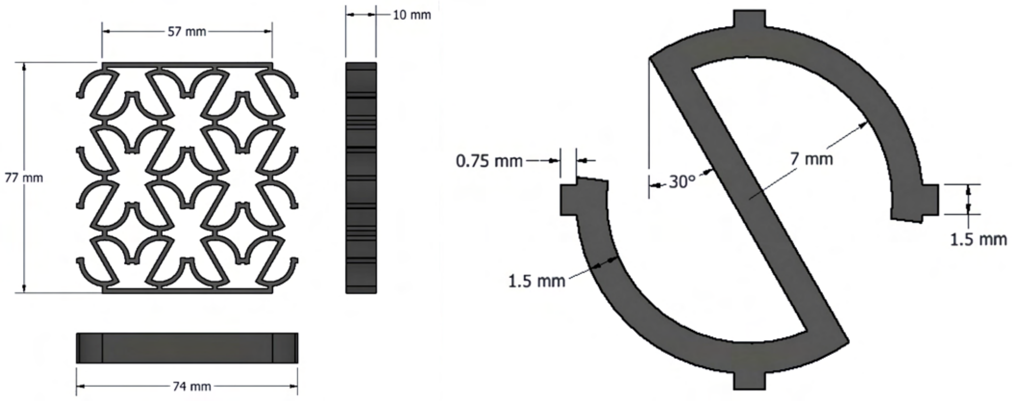

Figure 3.2: CAD model of the adopted S-shaped auxectic structure.

Subsequently, the 3D printing phase was initiated. The printing parameters utilized in the Fused Filament Fabrication (FFF) process are concisely presented in Table 3.2, with a printing speed set at 45 mm/s.

3.1.3 Printing Results

Given the orthotropic behavior that 3D printed parts can present, the specimen's layers were printed along the same direction, leading to some imperfections in the transition region located between grip surface and narrow section. Moreover, noticeable variations in the lateral borders result from the absence of walls. Figure 3.3 illustrates the printed PETG specimen.

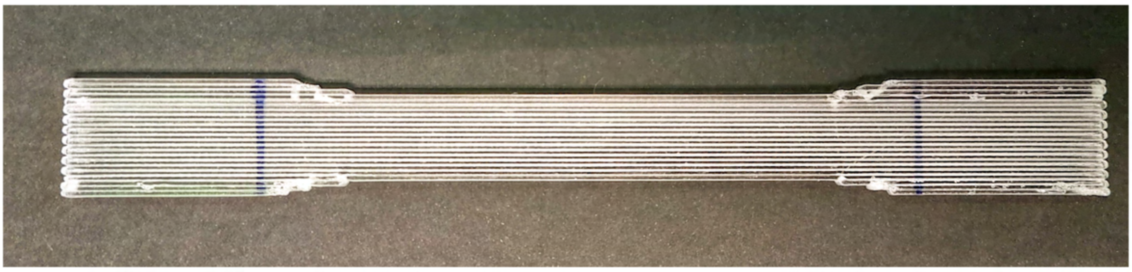

Figure 3.3: PETG specimen adopted for the material characterization: 3D printed specimen.

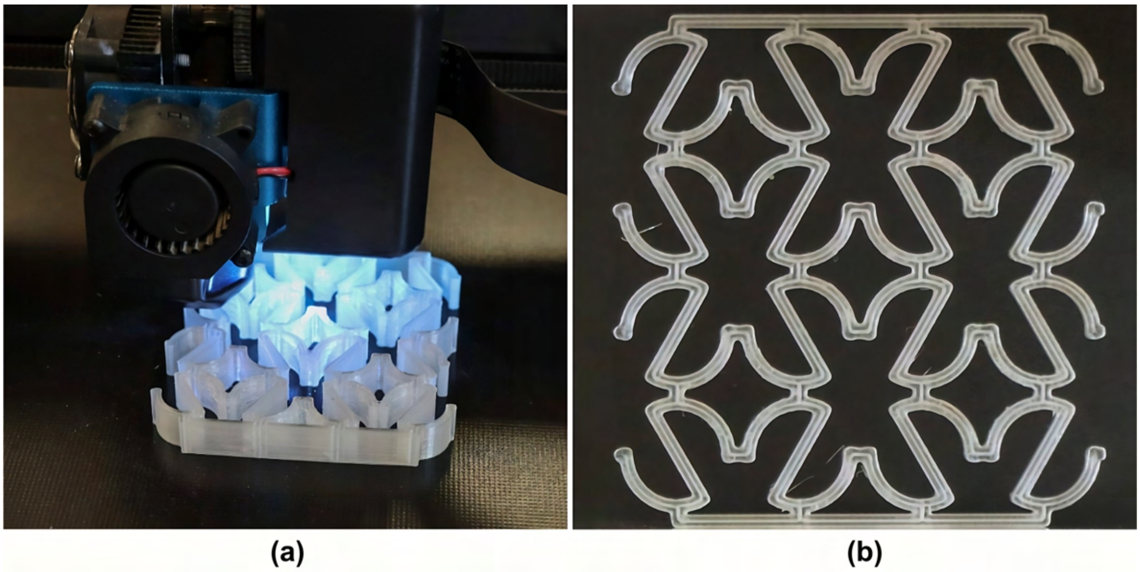

Figure 3.4: (a) Manufacturing of the samples through the FFF process and (b) 3D printed S-shaped sample.

In the case of the S-shaped structure samples, the 3D-printed specimens exhibited minimal issues. The only noticeable deviation was observed in the contours, which appeared slightly more rounded compared to the CAD model. However, this particular characteristic did not adversely impact the results of the tests. Additionally, some stringing is visible, attributable to the intricate nature of the structure and the challenges associated with 3D printing using PETG material. A visual representation of a sample during the printing process, as well as a completed printed sample, is depicted in Figure 3.4.

3.2 Testing Procedure and Apparatus

3.2.1 PETG Specimen Tensile Test

After printing and measuring the specimens, the adopted PETG was characterized by performing uniaxial tensile tests carried out in accordance with ASTM D638 standard. Three specimens were tested at a displacement rate of 2 mm/min using a Shimadzu universal testing machine, AGS-X, equipped with a 10 kN load cell. All testing data (displacement and load) were recorded by the testing machine acquisition system. The applied sample rate was 10 Hz. To obtain measurements of lateral and longitudinal deformation and subsequently calculate Poisson's ratios, a camera was employed to capture images at two distinct moments: one before the beginning of the test and the other immediately after its conclusion. These captured images were processed using ImageJ software. The experimental setup adopted for these tests is depicted in Figure 3.5.

Throughout the uniaxial tensile test, load-displacement curves were recorded in terms of the applied load (P), measured using the load cell, and the crosshead displacement (δ). After measuring the specimens, a cross-sectional area (A) of the narrow section was found to be 39mm^2 and an initial gauge length (l) of 105 mm was set when the specimens were placed within the grips of the testing machine. For each specimen, stresses (σ) and strains (ε) were calculated using the Equations 3.1 and 3.2 at each acquired point.

$$\sigma = \frac{P}{A} \quad (3.1)$$

$$\varepsilon = \frac{\delta}{l} \quad (3.2)$$

The values calculated using Equations 3.1 and 3.2 are the engineering data. In Section 4.2 is explained how these values were converted into true data.

The characterization of the adopted PETG involved the calculation of different mechanical properties, including the ultimate tensile strength (UTS), yield strength, Young's modulus (E), and Poisson's ratio (ν). The UTS represents the maximum stress applied to the specimen. To determine Young's modulus (E), an initial linear portion of the stress-strain curve was selected. More specifically, Equation 3.3 was applied to the strain range between 0.1% and 0.4%. Since the elastic regions of the stress-strain curves were not entirely linear, typical yield points could not be identified. Thus, an offset line, parallel to the linear portion used to calculate Young's modulus (E), was constructed and located at a positive strain of 0.2%. The intersection point between this offset line and the stress-strain curve represented the yield point, with the corresponding stress denoting the offset yield strength. As previously mentioned, Poission's ratio (ν) was determined by analyzing images captured before and after the test using ImageJ software. The initial image of the specimen, in which it was undeformed, provided reference dimensions that were used as input to ImageJ software. Therefore, the software was able to calculate the dimensions of the deformed specimen in the second image. Based on the calculated lateral and longitudinal strain values, the Poisson's ratio (ν) was determined for each specimen using Equation 3.4.

$$E = \frac{\sigma_{0.4\%} - \sigma_{0.1\%}}{\varepsilon_{0.4\%} - \varepsilon_{0.1\%}} \quad (3.3)$$

$$\nu = -\frac{\varepsilon_{lateral}}{\varepsilon_{longitudinal}} \quad (3.4)$$

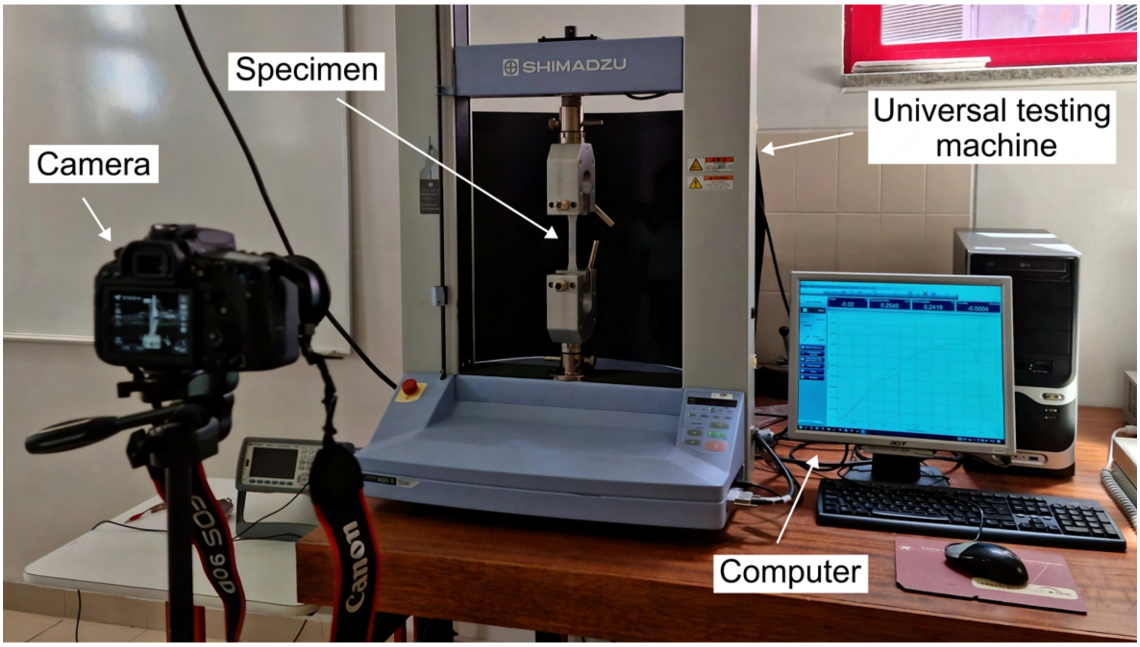

Figure 3.5: Experimental setup for uniaxial tensile testing of PETG specimens.

3.2.2 PETG S-shaped Auxectic Samples Tests

The S-shaped samples were subjected to two distinct types of testing for analysis, compression tests and two distinct creep-recovery tests. All these evaluations were conducted using the Shimadzu, AGS-X, universal testing machine equipped with a 10 kN load cell. For the compression and creep-recovery tests, compression platens were mounted on the testing machine. The experimental configuration for these testing procedures is depicted in Figure 3.6.

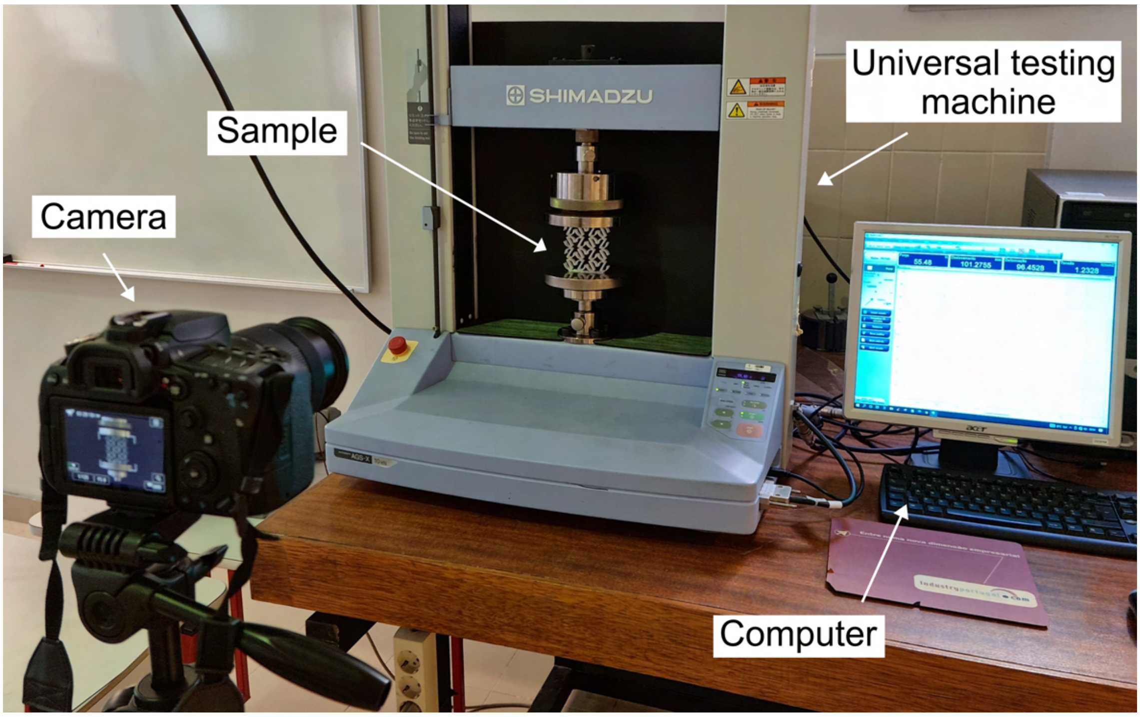

Figure 3.6: Experimental setup for compressive testing of PETG S-shaped samples.

3.2.2.1 PETG S-shaped Auxectic Samples Compression Tests

The compression tests were performed on three specimens, each subjected to a uniaxial compressive load, achieving a maximum displacement of 45 mm at a constant rate of 2 mm/min, following the methodology outlined by Meena and Singamneni [119]. During these tests, precise measurement of lateral displacements of S-Shaped specimens was essential for calculating the Poisson's ratio at specific points during the testing process. To achieve this, a camera was employed to record the tests, allowing the capture of frames at the desired moments.

The compression tests resulted in force-displacement curves. To characterize the mechanical behavior of the S-shaped structure, stress-strain curves of the samples were required. Similar to the characterization of the PETG specimens as detailed in Subsection 3.2.1, stress σ and strain ε were calculated using Equations 3.1 and 3.2, respectively. In these Equations, P represents the load applied to the top face of the specimens, measured by a load cell, A denotes the area of the bottom/top faces of the specimens, which is 57 mm^2, δ represents the crosshead displacement, and l represents the initial length of the specimens, which is 77 mm.

For the mechanical characterization of the S-shaped structure, several parameters were calculated, including the stress of the yield point, the maximum stress before densification, Poisson's ratio (ν), the stiffness, and the total energy absorption (TEA) for each sample. The calculation of the strength of the yield point, and the maximum stress before densification followed a similar procedure to that described in Subsection 3.2.1, with Equation 3.3 being used to determine the Young's modulus. The values obtained for the stiffness were the values of the slopes of the straight lines of the stress-strain curves in the elastic region.

To calculate the Poisson's ratio (ν) of the S-Shape structure, specific time points were selected during the test. These points correspond to longitudinal displacements at 0, 5, 10, and 15 mm. Frames capturing these moments were extracted from the recorded videos using a Python code. Subsequently, these images were processed using ImageJ software to determine the lateral and longitudinal displacements of the samples under loading. First, a known reference dimension, i.e. custom dimension of an undeformed sample, was provided to ImageJ software. Using this known length, the software converted it into a specific number of pixels, facilitating the calculation of the dimensions of the deformed samples. This correspondence between frames and longitudinal displacement values allowed the calculation of lateral displacements for each structure. The lateral and longitudinal displacements obtained from the deformed images were used to determine the strains, allowing the calculation of the Poisson's ratio (ν) using the Equation 3.4.

To calculate the total energy absorption, it was necessary to determine the area under the force-displacement curve for each sample. This was accomplished by subdividing the curve into small trapezoidal sections and calculating their respective area (A_{TEA}) using the Equation 3.6. Adapting the calculation of the area of a trapezoid ($A_{trapezoid}$), Equation 3.5, P_n and P_{n+1} represent the force values at points n and $n+1$, respectively, and $\delta_{n+1} - \delta_n$ represents the difference in displacement between these two points. This adaptation results in Equation 3.6. Summing the areas of all the trapezoids, provides the total area under the curve, thus yielding the total energy absorption (TEA) of each structure during the compression test, Equation 3.7.

$$A_{trapezoid} = \frac{a+b}{2} \cdot h \quad (3.5)$$

$$A_{TEA} = \frac{P_n + P_{n+1}}{2} \cdot (\delta_{n+1} - \delta_n) \quad (3.6)$$

$$TEA = \sum A_{TEA} \quad (3.7)$$

3.2.2.2 PETG S-shaped Auxectic Samples Creep-Recovery Tests

Two distinct creep-recovery tests were conducted, each encompassing different displacement conditions. In the first test, a displacement was applied to maintain the samples within the elastic regime, while the second test entailed applying a displacement that led the samples into the plastic regime. Both creep-recovery tests comprised three cycles, with each cycle involving a specific longitudinal displacement applied for 60 min, followed by a subsequent displacement of 0 mm for another 60 min.

The selection of the displacements for these creep-recovery tests was guided by the results of the compressive tests performed on the samples. Analyzing the stress-strain curves obtained from the compressive tests allowed the determination of the samples' yield point, a pivotal point on the stress-strain curve that delineates the transition from elastic behavior to plastic behavior.

The yield point marks the transition between elastic deformation, where materials revert to their original shape after stress removal, and plastic deformation, which entails permanent and non-reversible shape alterations. In the creep-recovery test involving the elastic regime, a displacement of 1.7 mm was employed, corresponding to a stress value 30% below the stress of the yield point of the samples. For the creep-recovery test associated with the plastic regime, a displacement of 4.6 mm was selected, reflecting a stress value 30% above the yield point.

3.3 Material Characterization Results

The fractured PETG specimens can be seen in Figure 3.7. The small blue dots marked on the surface of the narrow section of the specimens were used in image post-processing to determine longitudinal and lateral strains.

Figure 3.8 illustrates the engineering stress-strain curves obtained from the uniaxial tensile test of the three PETG specimens. As mentioned before, both the stresses and strains were calculated using Equations 3.1 and 3.2. From Figure 3.8 excellent consistency can be observed between the elastic modulus of the tested specimens. Regarding the tensile strength, the obtained values also present a good consistency, although some premature failure has been observed, leading to slightly different elongations at break.

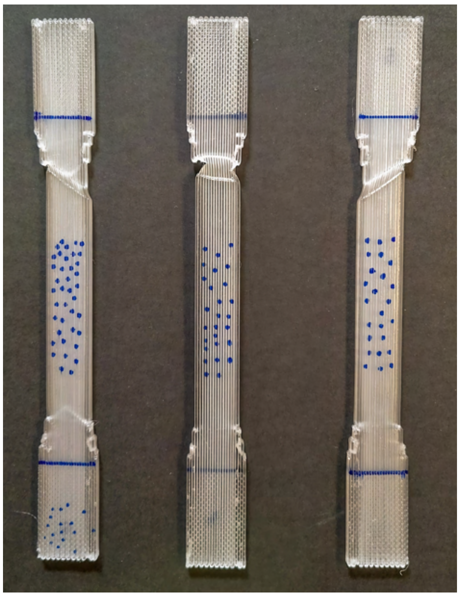

Figure 3.7: PETG specimens after uniaxial tensile test.

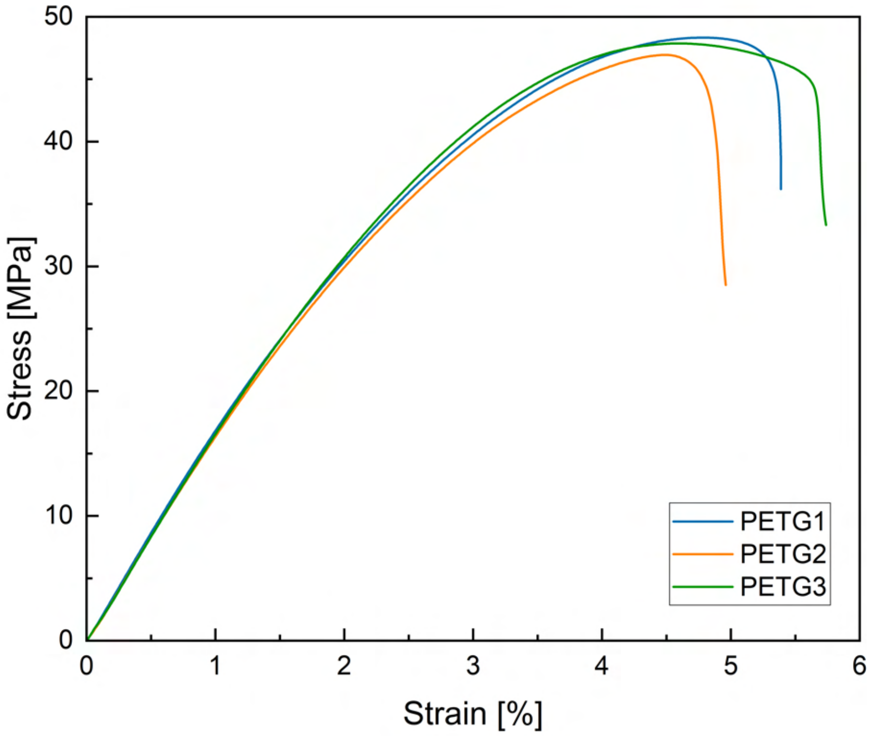

Figure 3.8: Experimental tensile test stress-strain curves of the PETG specimens.

Table 3.3 summarizes the results obtained for the mechanical properties of each PETG specimen tested. From Table 3.3, it is worth highlighting the low coefficients of variation (CoV), calculated as the standard deviation divided by the average of the data set, for each property obtained from the experimental tests, which indicates precise and valid experimental results. Also, comparing these results to the data form Table 3.1, it is visible that the UTS values obtain experimentally are close to the Tensile strength value provided by the PETG manufacturer. Hence, the PETG characterization depended on the outcomes derived from PETG1 specimen, as it closely matched the average stress-strain behavior of all specimens.

Table 3.3: Experimental tensile test results of the PETG specimens.

Specimen	**Yield Strength (MPa)**	**Ultimate Tensile Strength (MPa)**	**Young's Modulus (GPa)**	**Poisson's Ratio**
PETG1	27.806	48.330	1.764	0.379
PETG2	31.456	46.947	1.626	0.342
PETG3	34.990	47.868	1.617	0.321

CoV (%)	9.34	1.20	4.03	6.84

Chapter 4

Numerical Procedure

This chapter serves as an important component of this study, delving into the computational aspects of the research carried out. This chapter outlines the specific procedures and methodologies employed in numerical simulations, focusing on two crucial aspects: (i) the initial simulations conducted to validate the mechanical behavior of the adopted material within the models and (ii) the subsequent simulation of an auxetic structure. These numerical investigations were meticulously executed using Ansys Mechanical, an integral component of Ansys Workbench 2021 R2 software.

The primary objective of this chapter is to shed light on the computational framework that underpins the study, elucidating the steps taken to ensure the accuracy and reliability of numerical simulations. By providing a detailed account of the processes involved, from the verification of material characterization within the simulations to the complex modeling of auxetic structures, this chapter enables a comprehensive understanding of the pivotal role played by numerical analyses in this research. Furthermore, it sets the stage for the subsequent chapters, where the results and implications of these numerical investigations will be discussed in-depth, ultimately contributing to the attainment of valuable insights and conclusions.

4.1 Finite Element Method

The finite element method is a numerical method widely used in the solution of practical problem whose geometry and boundary conditions are generally complex [129]. The method surged as a new possibility to solve problems of elastic theory, overcoming the difficulties and problems inherent to the methods of Rayleigh-Ritz, Galerkin, finite differences, weighted residuals and others. In the Rayleigh-Ritz and Galerkin methods, for example, it is not always easy to obtain the approximation functions that satisfy the irregular boundary conditions and know whether they approximate the exact function.

The finite element method predicts the division of a continuous integration domain into a finite number of small regions, making this domain discrete. The main reason for dividing a continuous domain into several subdomains is due to the fact that it makes modeling simpler by approximating a complex function through several segments of simpler functions. However, each function segment must respect its neighborhood so that the function and its derivatives are continuous at neighboring points.

The finite element method is based on principles of analytical mechanics which are established in terms of scalar quantities such as work and energy. The principle of virtual displacements is part of analytical mechanics and predicts that a deformable solid is in equilibrium if, and only if, the sum of the work done by external forces and the work done by internal forces is zero for virtual displacements [129], as it is showed in Equation 4.1:

$$\delta W = \delta W_e + \delta W_i = 0 \quad (4.1)$$

Being U^i the internal deformation energy and V^e the work done by the external forces, the potential energy functional can be written as Equation 4.2.

$$\Pi = U^i - V^e \quad (4.2)$$

To meet the equilibrium condition according to the principle of virtual displacements, we have:

$$\delta\Pi = \delta U^i - \delta V^e = \delta\left(U^i - V^e\right) = 0 \quad (4.3)$$

The total potential energy functional of deformable bodies is given by the next Equation [130]:

$$\Pi = \frac{1}{2}\int_V \{\varepsilon\}^T [D]\{\varepsilon\} dV - \int_A \{u\}^T \{F\} dA \quad (4.4)$$

where $\{\varepsilon\}$ is the strain vector, $[D]$ is the constitutive stress-strain matrix, $\{u\}$ is the displacement vector and $\{F\}$ is the external forces vector.

The displacement vector can be rewritten in function of the nodal displacements:

$$\{u\} = [\Phi]\{q_e\} \quad (4.5)$$

where $[\Phi]$ is the shape function matrix of the element and $\{q_e\}$ is the nodal displacement vector of the element.

Defining $[L]$ as the matrix of the differential operators, the strain vector can be written as function of the nodal displacements of the element:

$$\{\varepsilon\} = [L]\{u\} = [L][\Phi]\{q_e\} = [B]\{q_e\} \quad (4.6)$$

where $[B] = [L][\Phi]$ contains the derivative of the shape function matrix.

Substituting Equations 4.5 and 4.6 into Equation 4.4, the potential energy functional for an element can be rewritten as:

$$\Pi = \frac{1}{2}\int_V \{q_e\}^T [B]^T [D][B]\{q_e\}dV - \int_A \{q_e\}^T [\Phi]^T \{F\}dA \quad (4.7)$$

Applying the equilibrium condition of the principle of virtual displacements in Equation 4.7 and knowing that $\{q_e\}$ and $\delta\{q_e\}$ do not change in volume and area, we have that:

$$\delta\Pi = \delta\{q_e\}^T \left(\int_V [B]^T [D][B]\,dV\{q_e\} - \int_A [\Phi]^T \{F\}dA\right) = 0 \quad (4.8)$$

Since $\delta\{q_e\}$ is any:

$$\int_V [B]^T [D][B]\,dV\{q_e\} - \int_A [\Phi]^T \{F\}dA = 0 \quad (4.9)$$

Defining the element stiffness matrix as:

$$[K_e] = \int_V [B]^T [D][B]\,dV \quad (4.10)$$

and the vector of equivalent nodal forces as:

$$\{f\}_e = \int_A [\Phi]^T \{F\}dA \quad (4.11)$$

the following expression is obtained for a given element:

$$[K_e]\{q_e\} = \{f\}_e \quad (4.12)$$

The global formulation will be obtained the contribution of each element to the corresponding nodal values, and can be written as:

$$[K]\{q\} = \{f\} \quad (4.13)$$

The expressions obtained previously are general and they can be used for different types of elements, starting from unidirectional elements to three-dimensional elements. In the next section, these expressions will be developed for the particular case of an 8-node hexahedral element that will be used in the simulations.

4.1.1 3D 8-Node Structural Solid Element

The finite element analysis employed SOLID185 for the three-dimensional modeling of solid structures. This element is characterized by eight nodes, with each node possessing three degrees of freedom, encompassing translations in the x, y, and z directions. SOLID185 offers a comprehensive range of capabilities, including plasticity, hyperelasticity, stress stiffening, creep, large deflection, and large strain behavior. It also accommodates mixed formulations for simulating deformations in nearly incompressible elastoplastic materials and fully incompressible hyperelastic materials. Importantly, SOLID185 is available in two variations: (i) a homogeneous structural solid and (ii) a layered structural solid [131].

While 3D printed materials often exhibit layered characteristics, for the sake of computational simplification, this study adopted a homogeneous structural solid element. The shape function of this element in the u direction is defined by Equation 4.14, and the shape functions for the v and w directions follow similar formulations as in the u direction.

$$\begin{aligned}\Phi =& \frac{1}{8}\left[\, u_I(1-s)(1-t)(1-r) + u_J(1+s)(1-t)(1-r)\right.\\ &+ u_K(1+s)(1+t)(1-r) + u_L(1-s)(1+t)(1-r)\\ &+ u_M(1-s)(1-t)(1+r) + u_N(1+s)(1-t)(1+r)\\ &\left.+u_O(1+s)(1+t)(1+r) + u_P(1-s)(1+t)(1+r)\right] \quad (4.14)\end{aligned}$$

Typically, 3D printed materials possess orthotropic properties, but to streamline computational procedures, both the specimens and the structures were treated as isotropic materials. Consequently, the constitutive stress-strain matrix is represented as:

$$D = \frac{E}{(1+\nu)(1-2\nu)} \begin{bmatrix} 1-\nu & \nu & \nu & 0 & 0 & 0 \\ \nu & 1-\nu & \nu & 0 & 0 & 0 \\ \nu & \nu & 1-\nu & 0 & 0 & 0 \\ 0 & 0 & 0 & 0.5-\nu & 0 & 0 \\ 0 & 0 & 0 & 0 & 0.5-\nu & 0 \\ 0 & 0 & 0 & 0 & 0 & 0.5-\nu \end{bmatrix} \quad (4.15)$$

4.2 Single Element Model

A decision was made to perform a simulation using a single element with PETG material properties obtained from the tensile tests of PETG specimens. The purpose of this simulation was to calibrate the numerical model, necessitated by the non-linear behavior observed in the compressive tests on the S-shaped samples. Utilizing a standard elastic linear model during the simulation of the S-shaped structure in the non-linear region would lead to inaccuracies. Hence, the single element simulation was employed to calibrate the adopted constitutive model.

A static structural analysis was employed for this simulation. This type of analysis determines displacements, stresses, strains, and forces in the structure when subjected to a tensile load and it can be either linear or nonlinear. The initial step in preparing the analysis involved defining the Engineering Data. A new material, named PETG, was introduced, which incorporates its density, listed in Table 3.1, linear properties, including Young's modulus and Poisson's ratio derived from the PETG1 specimen, and nonlinear properties represented by the stress-strain curve. To introduce this curve, a multilinear isotropic hardening was defined in the Engineering Data. The stress-strain curves in Figure 3.8 are derived from the testing machine, which means that it is assumed that the cross-sectional area of the specimen does not change during the whole deformation process. These data are called engineering data. However, the actual cross-sectional area will decrease while deforming due to elastic and plastic deformation. Due to this, for defining multilinear isotropic hardening in Ansys, the true stress-strain curve is necessary. To convert engineering data into true stress-strain data, Equations 4.16 and 4.17 were applied to the experimental curves obtained for PETG. Figure 4.1 illustrates the comparison between engineering and true stress-strain curves obtained.

$$\sigma_{true} = \sigma_{eng.} \times \left(1 + \varepsilon_{eng.}\right) \quad (4.16)$$

$$\varepsilon_{true} = \ln\left(1 + \varepsilon_{eng.}\right) \quad (4.17)$$

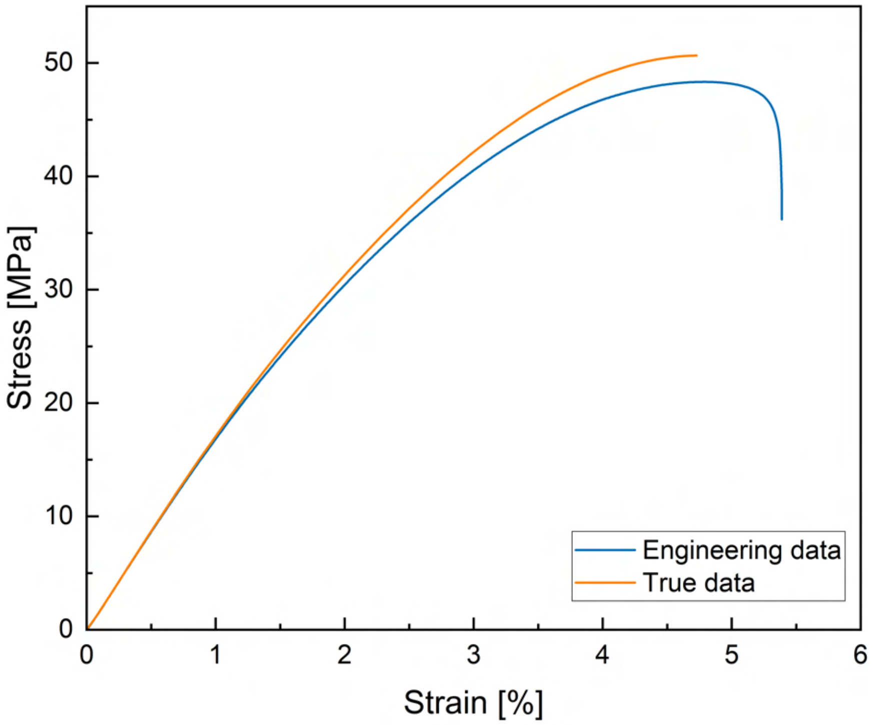

Figure 4.1: PETG stress-strain curves: engineering data vs true data.

The next stage involved defining the geometry, where a cube was created using SpaceClaim, a CAD application integrated into Ansys. Each edge of the cube measured 1 mm. Subsequently, the geometry was imported into the Ansys Mechanical application to set up the simulation. The cube was designated as a flexible body, and the PETG material, previously defined, was assigned to it. The mesh was defined with a uniform element size of 1 mm, resulting in a single-element domain discretization.

Boundary conditions were first imposed on three faces of the cube: (i) at face x = 0 mm, with components y and z free and component x fixed at 0 mm, (ii) at face y = 0 mm, with components x and z free and component y fixed at 0 mm, and (iii) at face z = 0 mm, with components x and y free and component z fixed at 0 mm. A displacement of 0.0484 mm was prescribed to the face at y = 1 mm along the y direction, corresponding to the last true strain value from the engineering data. Figure 4.2 shows the boundary conditions applied to the cube.

The predefined analysis settings were employed, aiming to compute the stress on the face at y = 1 mm and the resulting strain along the y direction. These results allowed the comparison with the experimental tensile test results obtained from the tested specimens. A force reaction probe was placed on the face y = 1 mm to obtain the stress, while a directional deformation object was employed to measure the strain along the y direction. Given that the dimensions of the cube's edges are 1 mm, it is worth noting that the recorded values from the force reaction probe represent stress measured in megapascals (MPa), while the values derived from the y-directional deformation analysis pertain to strain and are expressed in millimeters per millimeter (mm/mm). Figure 4.3 shows the deformed configuration and the reaction force of the cube.

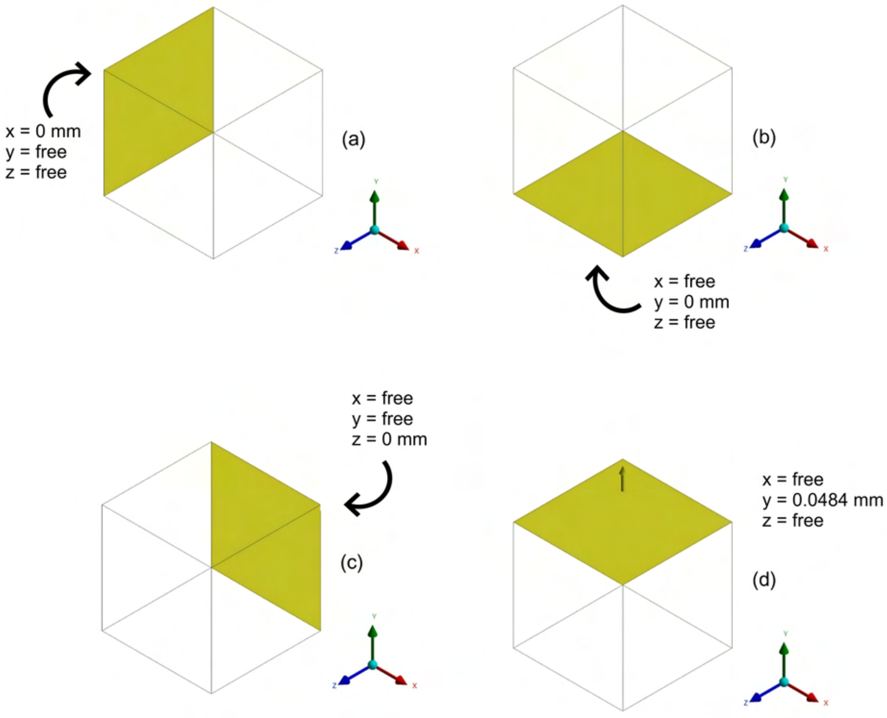

Figure 4.2: PETG single element boundary conditions: (a) x = 0 mm; (b) y = 0 mm; (c) z = 0 mm; (d) displacement applied.

This simulation comprised a single load step. In finite element analysis (FEA), load steps represent distinct phases or stages within the analysis process, typically involving variations in loads, boundary conditions, or material properties. Substeps, on the other hand, are subdivisions or increments within a load step, primarily employed to enhance the temporal or loading history resolution. Their purpose is to more accurately capture a structure's behavior, particularly in dynamic or nonlinear simulations. Substeps enable the load step to be partitioned into smaller time intervals or iterations, thereby aiding in convergence and facilitating a more detailed visualization of the model's behavior.

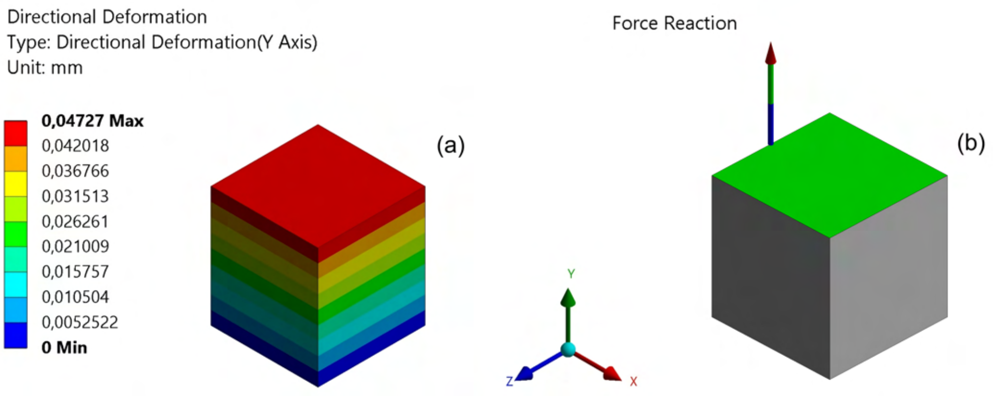

Figure 4.3: Numerical results of the PETG single element simulation: (a) deformed configuration; (b) force reaction.

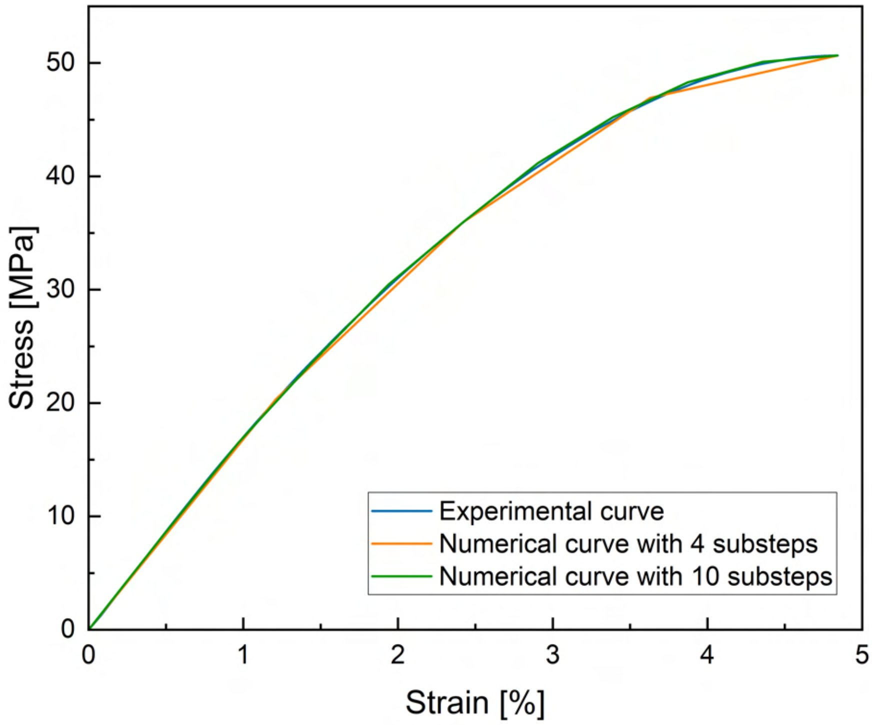

Figure 4.4: Experimental vs numerical stress-strain curves of the PETG single element simulation.

In this specific instance of the single-element simulation, Ansys automatically determined the number of substeps, resulting in a total of four substeps. Due to the low number of substeps in the simulation, the obtained results slightly deviated from the experimental curve, and therefore a second simulation with an increased number of substeps (10) was conducted. Figure 4.4 displays the experimental and numerical curves, demonstrating an excellent agreement between the results of the numerical simulation and the experimental data. This agreement indicated that the PETG material was accurately defined in the Engineering Data for the simulation.

4.3 Specimen Numerical Model

Up to this point, the simulations only considered material nonlinearity. To gain a better understanding of geometric nonlinearity, which was observed during the compression of the S-shaped structure, a simulation was conducted using a dogbone specimen subjected to large deflections. For this purpose, a new static structural analysis was employed, utilizing the same Engineering Data from PETG as before. The material model used in this simulation remained consistent with the previous one, and the boundary conditions encompassed fixed support and prescribed displacement. To represent the test scenario, the boundary conditions were applied to the rectangular portions at the extremities of the specimen, representing the grip areas. The displacement values were x = 5 mm, y = 0 mm, and z = 0 mm, with large deflections enabled. Figure 4.5 shows the boundary conditions applied to the specimen.

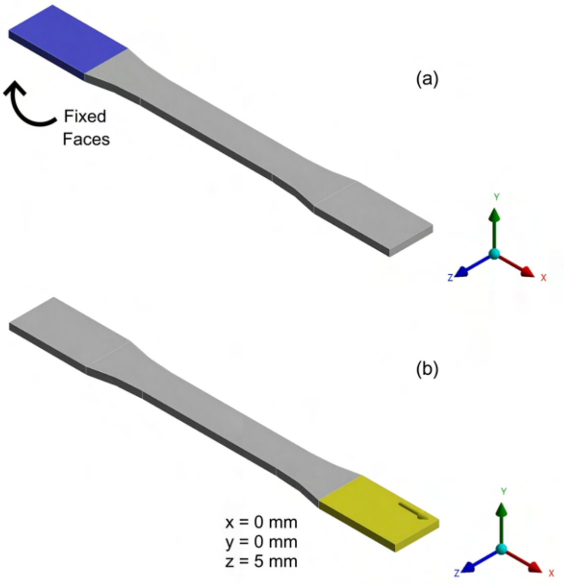

Figure 4.5: PETG specimen boundary conditions: (a) fixed faces; (b) displacement applied.

However, mesh convergence in this simulation could not be achieved, and the results suggested that the issue was related to the solver type. In fact, static structural analysis employs an implicit solver, prompting a subsequent attempt to use explicit dynamics analysis, which employs an explicit solver.

Implicit and explicit solvers are two distinct numerical techniques employed in FEA software, each offering unique advantages and limitations. The implicit solver is suitable for static and quasi-static simulations, as well as problems with slow dynamic responses. It is known for its stability in handling large time steps, making it computationally efficient for linear and mildly nonlinear analyses. The implicit solver employs an iterative approach, incrementally solving equations at each time step, which is ideal for capturing post-buckling behavior, material nonlinearity, and creep. However, it may converge slowly for highly nonlinear or dynamic simulations and could require significant computational resources. On the other hand, the explicit solver is designed for highly dynamic and transient simulations, particularly those involving impact, crash, or high-speed events. It computes results in a step-by-step manner, solving equations at each time increment without iterations. This approach provides better stability in the presence of severe nonlinearities and contact conditions, making it suitable for simulating rapid, dynamic responses. However, the explicit solver requires smaller time steps than the implicit solver, which can lead to longer simulation times. Additionally, it may not be as efficient for simulations involving slow or quasi-static behavior.

In the explicit dynamics analysis, the Engineering Data remained the same, but an additional parameter was introduced: the plastic strain failure value, which corresponds to the final point on the stress-strain curve used for defining multilinear isotropic hardening, with a value of 0.0186 mm/mm. The geometry of the specimen was imported, as depicted in Figure 3.1, retaining the same material model and boundary conditions as in the previous simulation. Explicit dynamics analysis introduces specific analysis parameters distinct from those of static structural analysis. Given the time-dependent nature of the explicit solver, it was imperative to establish the simulation end time. A desired simulation rate of 5 m/s was chosen to replicate a quasi-static test, as recommended in Ansys Help Documentation [131]. Achieving this rate necessitated setting the simulation's end time at 0.001 seconds, accounting for the 5 mm displacement applied to the specimen. Furthermore, erosion control features were activated to manage material failure effectively. To ensure the accuracy of the analysis, a mesh convergence study was executed, involving the variation of element sizes, as visually depicted in Figure 4.6.

Figure 4.6 illustrates that mesh convergence was achieved when the number of elements in the mesh reached approximately 42500, corresponding to an element size of 0.6 mm. Figure 4.7 shows deformed configuration of the specimen. To facilitate the comparison of these simulation results with the experimental data, it was necessary to obtain stress and strain values experienced by the specimen. The applied stress was obtained by means of the normal stress in the solution, while the strain was determined through a user-defined result. This user-defined result summed the elastic strain and plastic strain since Ansys lacks a built-in result variable to calculate the total strain. Figure 4.8 displays the numerical stress-strain curve derived from this simulation alongside the experimental curve.

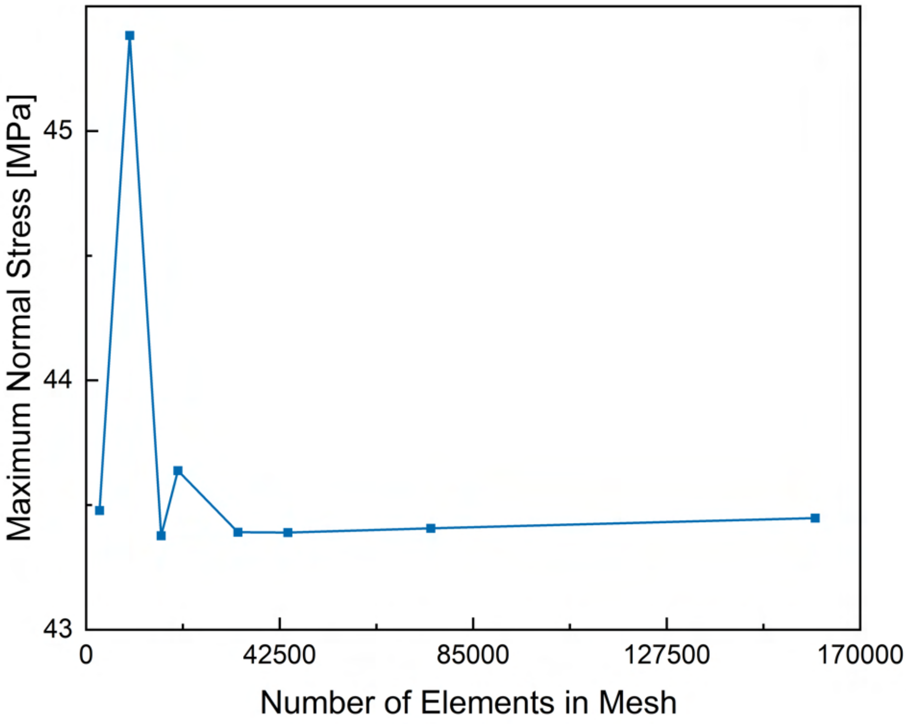

Figure 4.6: Mesh convergence of the PETG specimen numerical model.

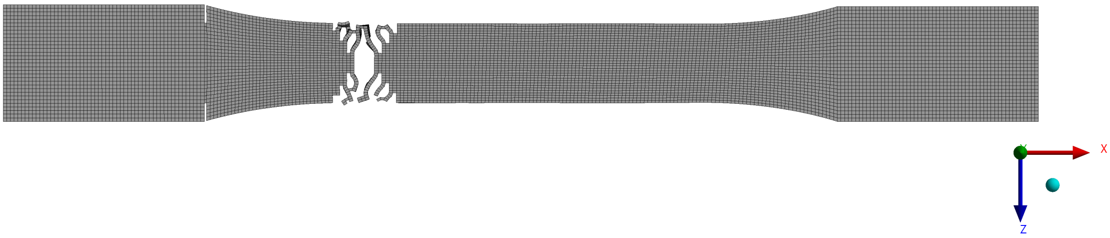

Figure 4.7: Numerical results of the PETG specimen simulation: deformed configuration.

The excellent agreement between the numerical data and the experimental results, as shown in Figure 4.8, confirms the correct implementation of this numerical model, paving the way for the primary focus of this study: the numerical simulation of the S-shaped structure.

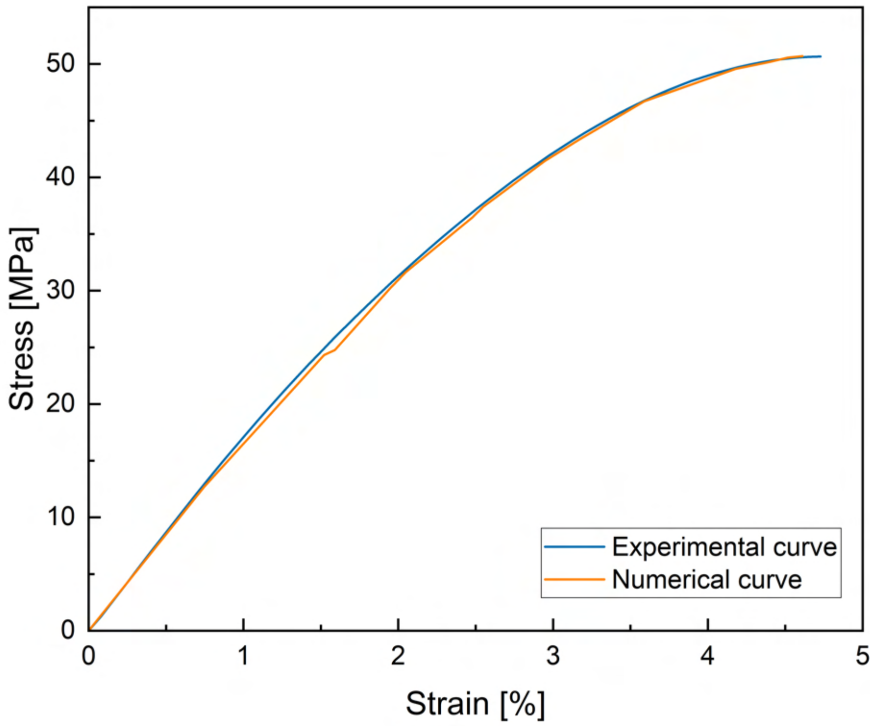

Figure 4.8: Experimental vs numerical stress-strain curves of the PETG specimen simulation.

4.4 S-Shaped Structure Numerical Model

To simulate the compressive behavior of the S-shaped structure, an explicit dynamics analysis approach was employed. The Engineering Data utilized for this analysis remained consistent with the one used in the explicit dynamics analysis detailed in Section 4.3. The imported geometry was the S-shaped structure, as depicted in Figure 3.2. The simulation process was initiated within the Mechanical Application of Ansys.

In the initial phase of the simulation setup, the stiffness behavior and material properties were defined. The S-shaped structure was characterized as a flexible body, with its material specified as PETG, as defined in the Engineering Data. The boundary conditions applied in this simulation included a fixed support at the bottom face and a displacement of 15 mm at the top face to replicate a compression test scenario.

Similar to the procedure outlined in Section 4.3, an imposed simulation end time of 0.003 s, along with the activation of erosion control on material failure, was employed to achieve a simulation rate of 5 m/s. Additionally, 30 load steps were defined, each lasting for 0.0001 s and incrementally increasing the displacement by 0.5 mm. A mesh convergence analysis was carried out in a manner analogous to Section 4.3, with the results presented in Figure 4.10.

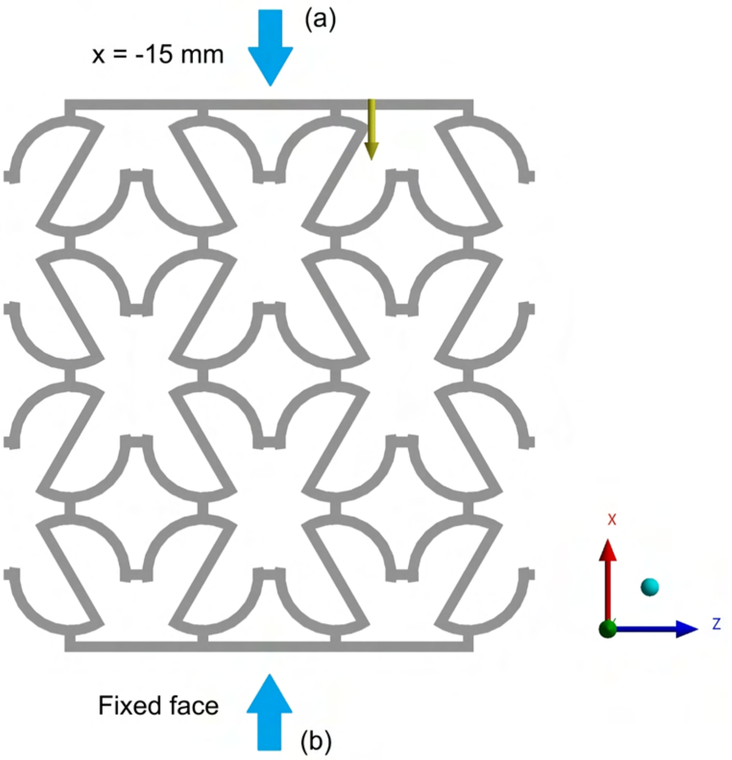

Figure 4.9: PETG S-shaped sample boundary conditions: (a) displacement applied; (b) fixed face.

From Figure 4.10, it is clear that mesh convergence occurs when the number of elements in the mesh approaches approximately 130000, corresponding to a mesh element size of 0.5 mm. However, it became apparent that the simulation of the compression of the structure could not accurately reproduce the experimental results, leading to convergence errors. Notably, the energy error was found to be too large and the simulation halted at a displacement of 14 mm. In explicit dynamics simulations, the total energy within the system should ideally remain conserved throughout the simulation, signifying that energy cannot be created or destroyed but can only change forms. Therefore, monitoring the energy balance in the system is crucial in explicit dynamics simulations. The relative energy error, which compares the current total energy with the initial reference energy, was set to 10% as a threshold in the Analysis Settings. When this error exceeds the defined threshold, the simulation is terminated. It is essential to highlight that this error serves as a warning and does not necessarily indicate incorrect results, particularly when no abrupt spikes in the energy history curve are observed, which was the case. To address this issue, the simulation was processed until a displacement of 15 mm by setting a very high number for the energy reference cycle, such as 9×10^7.

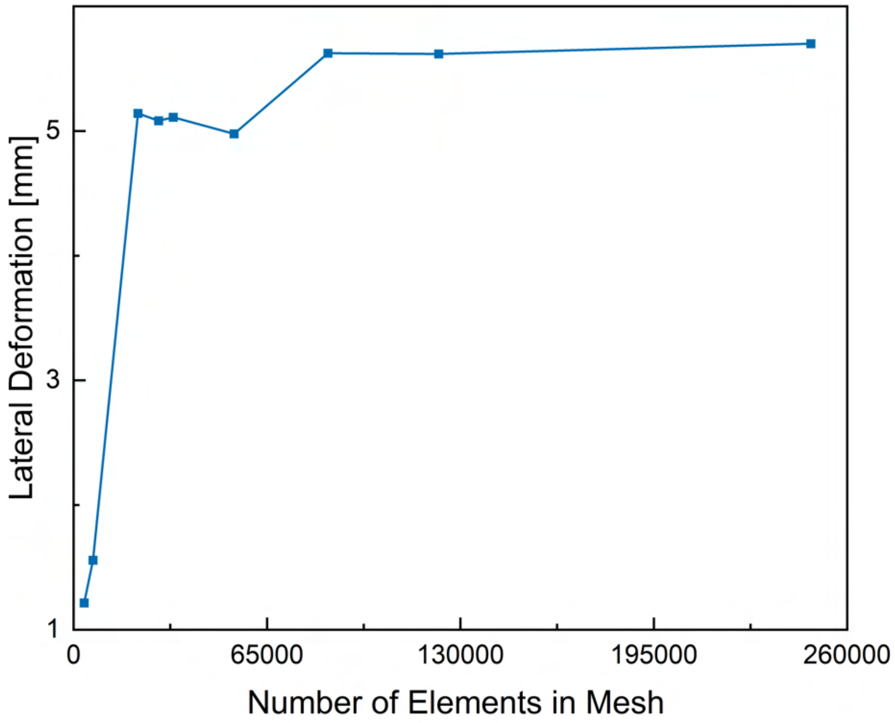

Figure 4.10: Mesh convergence of the PETG S-shaped sample numerical model.

During the first half of the simulation, up to a displacement of 7.5 mm, it was noted that the simulation deviated from the behavior observed in the experimental test images. This deviation likely stemmed from stability issues, as explicit solvers are known to exhibit reduced stability when addressing quasi-static problems. This instability is particularly prominent in scenarios involving nonlinear materials and intricate interactions, characteristics that were inherent in this simulation. To address these discrepancies, the same structure was subjected to a static structural analysis using the Engineering Data, geometry, stiffness behavior, material properties, boundary conditions, and mesh definitions consistent with the explicit dynamics analysis. Similar to the previous analysis, 30 load steps were defined, each incrementing the displacement by 0.5 mm.

After a close inspection of the results obtained from the simulation using an implicit solver, it was observed that beyond a displacement of 7.5 mm, the simulation exhibited issues such as penetration of certain structural components, leading to inaccurate behavior. Consequently, a decision was made to combine the results obtained from two separate simulations: one covering displacements from 0 mm to 7.5 mm, conducted through static analysis (implicit solver), and another encompassing displacements from 7.5 mm to 15 mm, conducted through explicit dynamics analysis (explicit solver). Due to the simulation limitations, precise values of stress-strain or force-displacement curves could not be obtained. Therefore, the Poisson's ratio of the simulated structure was adopted to compare the results. To achieve this, directional deformation was obtained along the z direction of two specific faces of the structure, as illustrated in Figure 4.11.

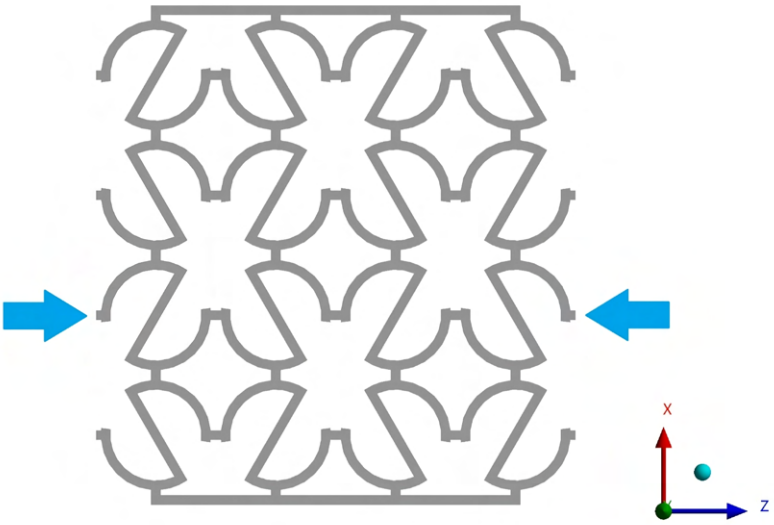

Figure 4.11: PETG S-shaped sample faces where lateral deformation along the z direction is calculated.

With these directional deformation values, the total deformation in both the lateral and longitudinal directions was calculated. The lateral strain was determined using Equation 3.2, with δ representing the total lateral deformation and l as the initial lateral length of the structure (74 mm). The longitudinal strain was computed similarly, utilizing δ as the applied displacement and l as the initial longitudinal length (77 mm). These calculated values were then employed in Equation 3.4 to derive the Poisson's ratio.

Chapter 5

Results and Discussion

The following section provides a comprehensive analysis and interpretation of the outcomes derived from both experimental and numerical tests conducted on the S-shaped structure. This pivotal chapter offers a profound insight into the mechanical behavior, properties, and performance characteristics of the investigated auxetic structure, as well as the implications of these research findings.

5.1 Experimental Results

In this section, a meticulous examination of the results obtained from a series of experimental tests is presented, including compression tests, creep-recovery tests, and the measurement of various material properties. These experimental endeavors aimed to elucidate the structural response of the S-shaped configuration under different loading conditions, offering valuable insights into its deformation mechanisms, stress-strain relationships, and energy absorption capabilities.

5.1.1 Compression Tests

The primary objective of the compression tests was to enable the mechanical characterization of the S-shaped structure. This characterization was achieved through the analysis of stress-strain curves, as explained in Subsubsection 3.2.2.1, and these curves are depicted in Figure 5.1. These curves illustrate the elastic-plastic deformation responses of the samples.

The stress-strain curves provided valuable data for determining several mechanical properties of the samples, including the stress of the yield point, the maximum stress before densification, and stiffness. These properties were calculated as described in 3.2 and their values are summarized in Table 5.1.

Within the elastic region of the stress-strain curves, a nearly linear relationship between stress and strain is evident, signifying uniform deformation of the unit cells. This linear region persists until a strain of approximately 3.508%, that corresponds to the yield point. Beyond this point, plastic deformation begins, introducing some waviness in the curves. At around 21.776% in strain, it is reached the maximum stress before the plateau phase. In this phase, the cell structures collapse due to buckling and bending of the cell unit and the plastic yielding. After 48.605% strain, the structures approach their compression limits, leading to a densely packed and distorted form. Data obtained beyond the plateau phase were excluded from structural characterization.

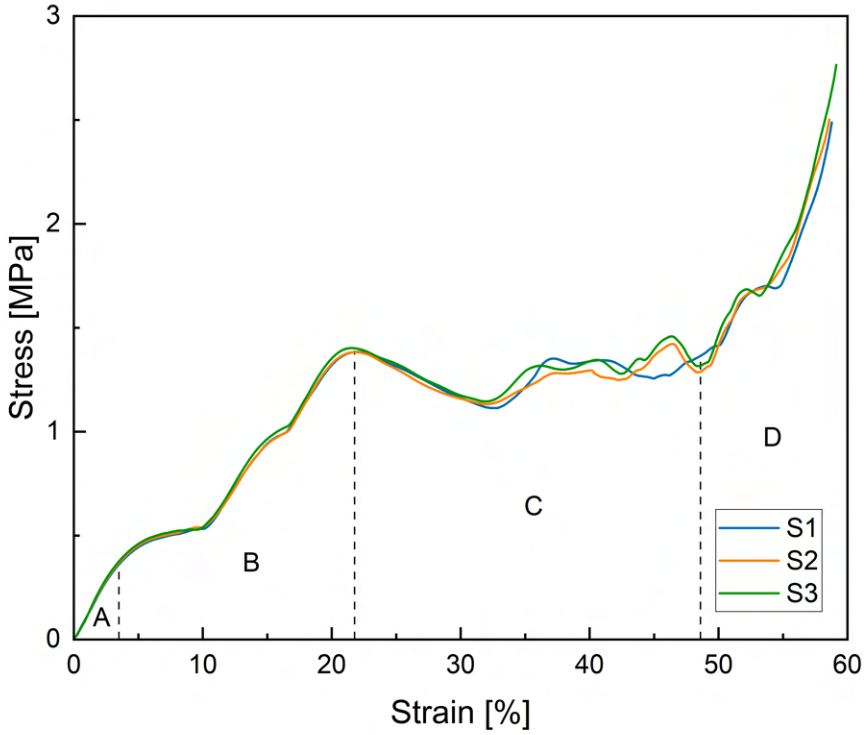

Figure 5.1: Experimental compressive test stress-strain curves of the PETG S-shaped samples: A - elastic deformation region; B - plastic deformation region; C - plateau region; D - densification region.

Table 5.1: Experimental compressive test results of the PETG S-shaped samples: mass, TEA and SEA.

Sample	**Stress of the Yield Point (MPa)**	**Maximum Stress Before Densification (MPa)**	**Stiffness (MPa)**
S1	0.354	1.384	10.409
S2	0.374	1.383	10.465
S3	0.380	1.402	10.691
Average	0.369	1.390	10.522
CoV (%)	3.01	0.628	1.16

The maximum stress before densification was found to be 1.390 MPa, the stress of the yield point 0.369 MPa, and the stiffness 10.522 MPa. These values exhibit low coefficients of variation, indicating the precision and validity of the results.

Upon analyzing the stress-strain curves globally in Figure 5.1, it can be observed that stress consistently increases during the elastic and plastic regions, indicating increased stiffness. Beyond the maximum stress before densification point, there is a decrease in stiffness, indicating structural failure, followed by a subsequent increase in stiffness due to significant densification. This behavior mirrors the stress-strain curves obtained by Meena and Singamneni [119], with similar values for the strain at yield point and at the point of maximum stress before densification despite the material used in their work was stainless steel that allows the structures to support higher values of stress. This suggests that the behavior of the S-shaped structure under compression is influenced more by its structural geometry than by its material properties.

The Poisson's ratio (ν) was calculated as described in Subsubsection 3.2.2.1, and Table 5.2 illustrates frames and ν values for various displacements. However, ν was not calculated for displacements of 20 and 25 mm, as these corresponded to the densification region. For a 0 mm displacement, the structure remained undeformed. At 5 mm, some deformation was observed, while at 10 and 15 mm, unit cells displayed rotational behavior. For 20 and 25 mm deformations, unit cells compressed without rotation, indicating densification. Notably, ν values increased with greater applied displacements, indicating a more pronounced Negative Poisson's Ratio (NPR) at lower displacement values.

Table 5.2: Experimental compressive test results of the PETG S-shaped samples: different applied displacements, their respective frame and value of Poisson's ratio.

Displacement	**0 mm**	**5 mm**	**10 mm**	**15 mm**	**20 mm**	**25 mm**
Frame						
Poisson's Ratio	0	-2.45	-1.52	-0.91	-	-

Upon comparing the Poisson's ratio results obtained in this study with those reported by Meena and Singamneni [119], notable differences emerge. Meena and Singamneni [119] reported values of ν around -1.6, -1.6, and -0.9 at displacements of 5, 10, and 15 mm, respectively. These values significantly differ from the results obtained in the current work. A detailed analysis of deformation behavior, considering all frames from both studies, reveals distinct patterns. The primary disparity lies in the material utilized.

In this study, the "S" structure was fabricated using PETG, whereas Meena and Singamneni [119] employed stainless steel. Despite geometric similarities between the "S"structures in both studies, they exhibited different deformation characteristics. Specifically, the PETG "S" structure demonstrated more pronounced lateral deformation in the two middle lines of "S" unit cells, with comparatively less deformation in the lines in contact with the faces, particularly at smaller displacements. In contrast, the stainless steel "S" structure by Meena and Singamneni [119] showcased a more consistent lateral deformation, where the two lines in contact with the faces deformed to a similar extent as the two middle lines. Notably, these face-contacting lines did not undergo as much lateral deformation as observed in the PETG "S" structure. This divergence, particularly evident at a 5 mm displacement, resulted in a more negative Poisson's ratio in the present study. This underscores that material properties exert a substantial influence on the Poisson's ratio of the structure, not solely determined by the adopted geometry, although their respective impacts may vary.

Another important mechanical property is the total energy absorption (TEA), which is characterized by the area under the force-displacement curve, represented in Figure 5.2. TEA calculations were carried out as detailed in Subsubection 3.2.2.1.

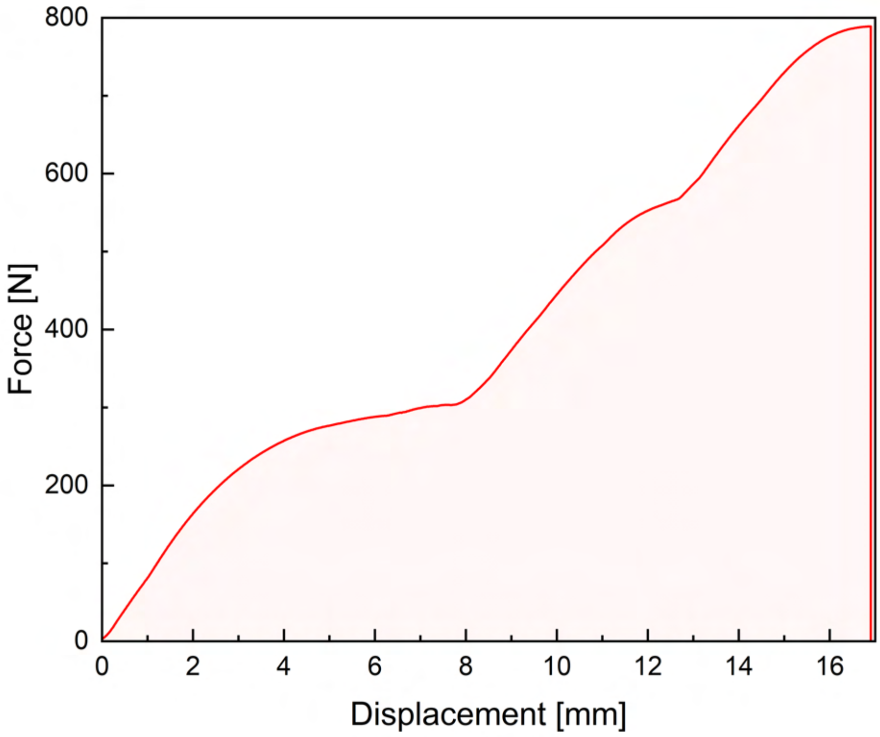

Figure 5.2: Experimental compressive test energy absorption curve of the PETG S-shaped samples.

For evaluating the energy absorption performance, the most common index is the specific energy absorption (SEA), that is, the energy absorption per unit mass. Table 5.3 presents the mass, TEA, and SEA values of each sample.

Table 5.3: Experimental results from the uniaxial tensile test.

Sample	Mass (g)	Total Energy Absorption (J)	Specific Energy Absorption (kJ/kg)
S1	19.381	6.853	0.354
S2	19.519	6.822	0.350
S3	19.231	6.773	0.352
Average	19.377	6.816	0.352
CoV (%)	0.607	0.483	0.464

The observed mass, TEA, and specific energy absorption (SEA) values were 19.377 g, 6.816 J, and 0.352 kJ/kg, respectively. Similar to other properties derived from experimental tests, these values demonstrated low coefficients of variation, indicating the precision and validity of the results.

Interestingly, even after being compressed to strain levels of approximately 60%, all samples remained free from cracking. This observation suggests that the S-shaped structure does not exhibit significant stress concentrations, a common issue in structures like the re-entrant structure, which often experiences cracking under substantial compression.

5.1.2 Creep-Recovery Tests

The purpose of the creep-recovery tests was to investigate the behavior of the S-shaped structure subjected to cyclic loading, where a sustained force is applied for an extended period, followed by its release and subsequent recovery. As described in Subsubsection 3.2.2.2, two distinct creep-recovery tests were conducted. In the first creep-recovery test, in which a displacement of 1.7 mm was applied, a force-time graph was generated, presented in Figure 5.3. As it is possible to see in Figure 5.2, with a displacement of 1.7 mm applied to the S-shaped samples, they are subjected to elastic deformation.

The results reveal a consistent behavior among all three samples. In the initial cycle, as the displacement is applied, the force supported by the structure initially increases. However, after reaching a maximum point, it experiences a sudden slight decrease. Subsequently, for the remainder of the applied displacement within this cycle, the force gradually decreases and approaches a nearly constant value. As the displacement approaches nearly 0 mm, the applied force decreases substantially until it is almost negligible, and the structure undergoes recovery for a duration equivalent to the time it was subjected to external forces. In the second and third cycles, the behavior remains consistent, differing from the first cycle primarily in the maximum force reached at the onset of the 1.7 mm displacement. Furthermore, in the second and third cycles this maximum force is slightly lower compared to the first cycle. Beyond this point, in the second and third cycles, the force values are nearly identical to those in the first cycle. The rate of reduction in force is gradual, leading to a nearly constant force value. This suggests that structural recovery occurs when no external force is applied. The minimal decrease in applied force between cycles and the stabilization of the endured force after 1.7 mm of displacement implies that an hour of force application is sufficient for the structure to stabilize. It can be inferred that if the test included more cycles, the behavior would likely remain consistent.

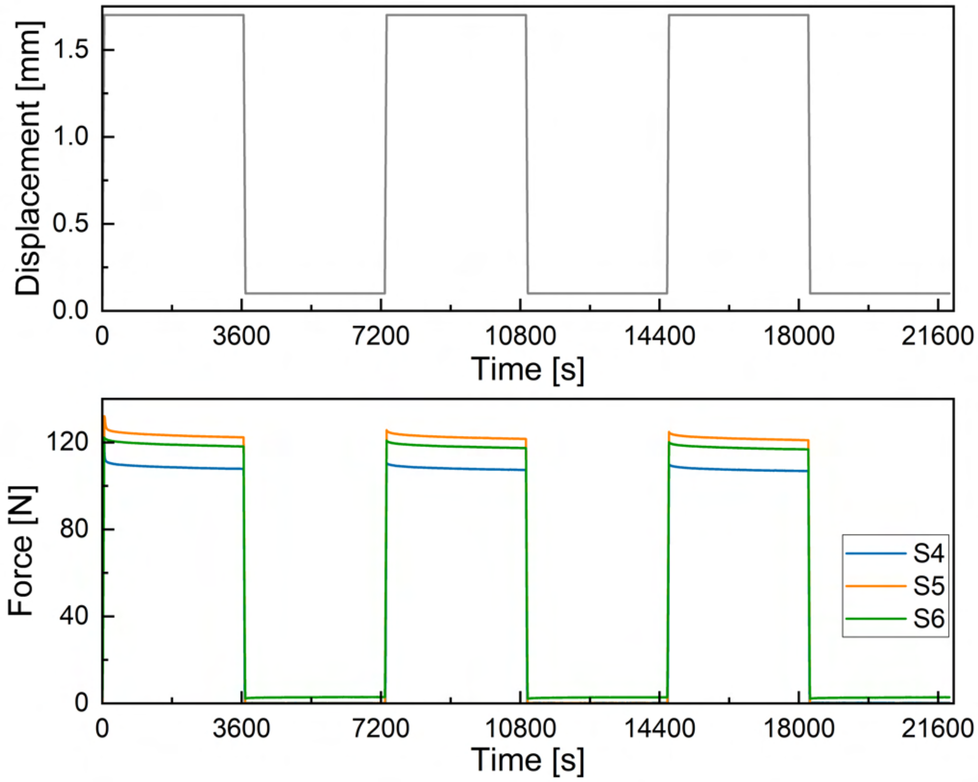

Figure 5.3: Experimental 1.7 mm displacement applied creep-recovery test curves of the PETG S-shaped samples.

The second test aimed to comprehend the recovery of the structure when subjected to a displacement corresponding to force values within the plastic deformation range of the structure. Figure 5.4 illustrates the results of the creep-recovery test applying a displacement of 4.6 mm. As it is possible to see in Figure 5.2, with a displacement of 4.6 mm applied to the S-shaped samples, they are subjected to plastic deformation.

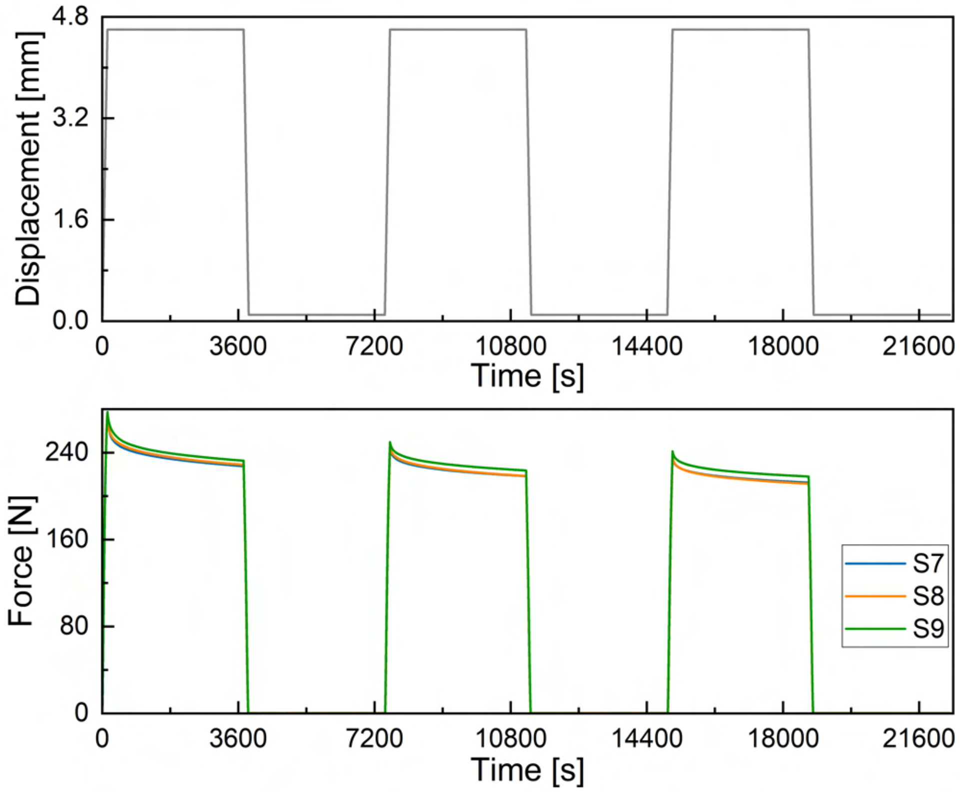

Figure 5.4: Experimental 4.6 mm displacement applied creep-recovery test curves of the PETG S-shaped samples.

Upon examination of Figure 5.4, a prominent peak load is observed at the outset of the first cycle, coinciding with the attainment of the 4.6 mm displacement. This peak represents the maximum force value sustained throughout the entire test. Subsequently, the applied force decreases as the displacement is retracted. After the recovery period, the displacement is re-applied, and upon reaching 4.6 mm of displacement, the force exhibits another peak, lower than the one observed in the first cycle but higher than the final force value in cycle 1 when the 4.6 mm of displacement was applied. After this peak, the force gradually decreases at a rate similar to that in the first cycle. The third cycle closely resembles the second cycle, with the peak slightly lower than that of the second cycle, followed by a force decrease similar to cycle 2. It is clear that in all cycles, even after an hour of applying a displacement of 4.6 mm, the force sustained by the structure did not stabilize. This suggests that if this displacement were applied continuously for more than an hour, the endured force would likely continue to decrease. Additionally, during the recovery phases, the structure exhibited some degree of recovery, although not complete. The initial cycle showed more pronounced damage, primarily because it was the first instance where the structure was subjected to plastic deformation, resulting in a more significant difference in resistance between cycle 1 and cycle 2.

5.2 Numerical Results

This section presents the results and discussion of numerical tests conducted in reference to Section 4.4. These numerical tests include the generation of numerical images depicting the behavior of the S-shaped structure during simulations. Additionally, the key result obtained through numerical analysis is the Poisson's ratio of the structure under various applied displacements, as depicted in Figure 5.5.

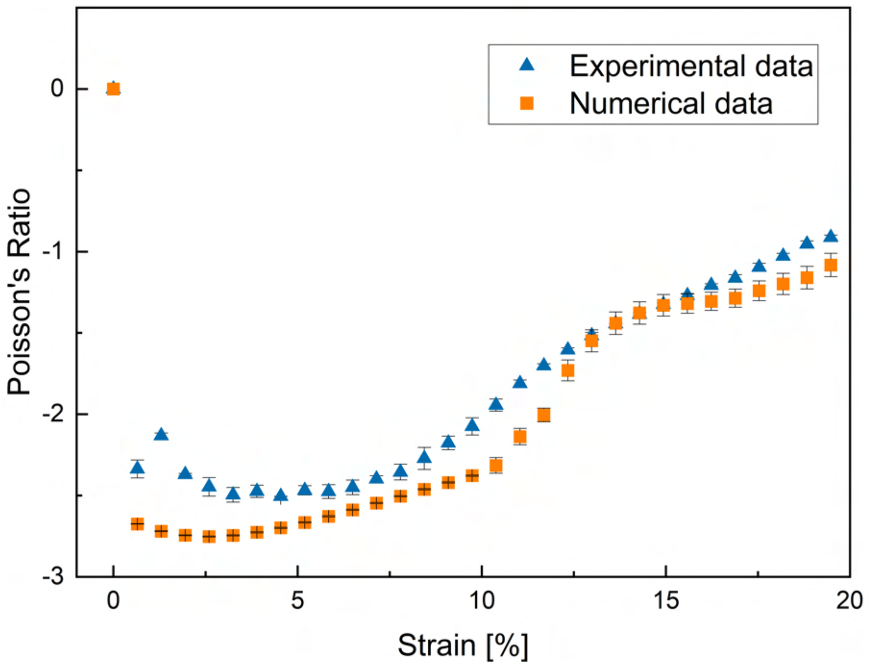

Figure 5.5: Poisson's ratio results of the PETG S-shaped samples: numerical data vs experimental data.

Figure 5.5 reveals a notable similarity between the numerical and experimental Poisson's ratio data. Overall, the numerically determined Poisson's ratios exhibit more negative values than those obtained experimentally. This contrasts with the findings of Meena and Singamneni [119]. This difference may be attributed to the mentioned differences in material or to the possibility of using material property data that do not agree with their material properties. Another contributing factor could be the use of only an implicit numerical model in their work.

Table 5.4 presents a series of images showcasing the numerical and experimental S-shaped structures under various applied displacements, facilitating a direct comparison between the two sets of images.

Table 5.4: Numerical vs experimental compressive test results of the PETG S-shaped samples: different applied displacements and their respective frames.

Displacement	**0 mm**	**1 mm**	**2 mm**	**3 mm**	**4 mm**	**5 mm**	**6 mm**	**7 mm**
Numerical	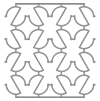	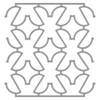	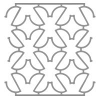	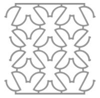	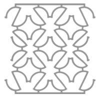	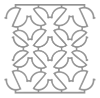	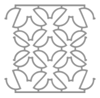	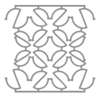
Experimental								
Displacement	**8 mm**	**9 mm**	**10 mm**	**11 mm**	**12 mm**	**13 mm**	**14 mm**	**15 mm**
Numerical	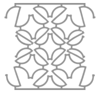	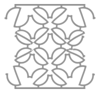	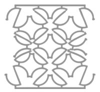	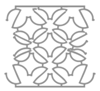	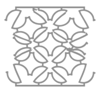	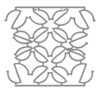	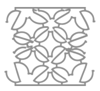	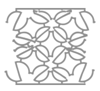
Experimental								

As depicted in Table 5.4, observations reveal that at an applied displacement of 0 mm, both numerical and experimental structures exhibit no discernible deformation. Similarly, at 1 mm displacement, minimal deformation is perceptible in both numerical and experimental investigations. By the time the displacement reaches 2 mm, deformation becomes apparent in both studies, notably initiating at the central lines. The lateral deformation becomes noticeable, and the behavior parallels in both the numerical and experimental realms. Beyond 3 mm, the deformation of cells in the central rows becomes markedly visible, particularly in the tip cells, demonstrating congruence between the two study methodologies. Starting from 6 mm of displacement, the deformation of central cells in both top and bottom rows becomes more pronounced in both numerical and experimental models. Up to 7 mm of applied displacement, the deformations in the numerical and experimental models remain remarkably identical. However, deviations emerge at 8 mm, as the structures in both studies diverge visibly. The numerical model exhibits vertical symmetry, unlike its experimental counterpart. Concurrently, the numerical study reveals the initiation of tip cell failure in the middle lines, a phenomenon absent in the experimental study. Despite these distinctions, the lateral deformation in the numerical study maintains substantial similarity to that in the experimental study. At a displacement of 10 mm, the numerical study exhibits visible failure in the central cells of the top row, a phenomenon absent in the experimental model. Upon reaching a displacement of 11 mm, the vertical symmetry observed in the numerical result diminishes, while at 12 mm displacement, the experimental result reverts to a state of vertical symmetry. Beyond 14 mm, numerical results progressively deviate from the experimental findings, and up to a displacement of 15 mm, both studies manifest similar lateral deformation, although individual cell deformations are not entirely congruent.

Chapter 6

Conclusions and Future Perspectives

The concluding chapter of this work encompasses a comprehensive summary of the findings and insights obtained throughout the study of auxetic structures. It serves as a platform to consolidate key outcomes and draw important conclusions from the research undertaken. Furthermore, this chapter explores the potential avenues for future investigations and the prospective applications of auxetic materials in various domains. It aims to provide a balanced perspective on the current state of knowledge in the field of auxetics, while also offering a forward-looking view into the possibilities and directions for future research and practical implementations.

6.1 Conclusions

In recent years, advances in various sectors, including aviation and aerospace, have driven the development of advanced materials with superior performance characteristics to meet stringent engineering requirements. These materials must combine high stiffness and strength with attributes such as weight savings, corrosion resistance, low maintenance, and cost-effectiveness. Composite materials, such as those used extensively in Boeing's B787 and Airbus's A380, have revolutionized aircraft design by reducing weight, leading to lower fuel costs, emissions, and maintenance. Unmanned aerial vehicles (UAVs) have also benefitted from composite materials, resulting in more capable and costly UAVs. However, there are still demands for materials with high shear strength, impact resistance, energy absorption, and damage detection in aerospace applications. Auxetic materials, a class of mechanical metamaterials with a negative Poisson's ratio, offer unique properties like superior shear and indentation resistance, fracture resistance, and energy absorption. These materials show promise for enhancing various aerospace components, from lightweight composites to airplane seats and interiors, wing and fuselage components, and even morphing airfoils, although further research is needed to unlock their full potential in this field.

The present work investigated auxetic structures, aiming to comprehensively understand their nature and potential applications. To achieve this, an initial research phase was conducted, encompassing topics related to auxetic structures such as Fiber-Reinforced Polymers (FRPs), sandwich composite structures, auxetic materials, auxetic composites, and additive manufacturing. This extensive review of the literature provided insights into the broader context of auxetic structures, elucidating their applications, potential use cases, and manufacturing methodologies. Additionally, a detailed exploration of their properties and classification was performed, ultimately leading to the selection of the S-shaped structure as the focus of the present study. The S-shaped structure, originally devised by Meena and Singamneni in Ref. [119], was chosen due to its novelty, relative limited existing research, and its unique geometric configuration, which suggested a wide range of potential applications across various engineering domains.

The primary objective of this research was to conduct a comprehensive investigation into the mechanical behavior of the S-shaped structure, which was fabricated using the Fused Filament Fabrication (FFF) technique. To achieve this goal, a systematic approach was undertaken, involving both experimental and numerical testing methodologies. However, before delving into the analysis of the S-shaped structure, it was imperative to carefully select the material for sample fabrication and subsequently characterize its mechanical properties. In this context, Polyethylene Terephthalate Glycol (PETG) was selected. The characterization process involved the fabrication of Type I specimens according to the ASTM D638 standard. Subsequently, a uniaxial tensile test, also conducted following the ASTM D638 standard, was employed to determine the mechanical properties of PETG. This comprehensive material characterization served as a critical foundation for developing accurate numerical models of the material's behavior in subsequent analyses.

Then, a series of PETG S-shaped structures were fabricated and subjected to compression and creep-recovery tests. Compressive tests served as a means of comprehensive investigation of the structural response of the S-shaped configuration when subjected to compressive loading conditions. These tests facilitated a nuanced exploration of deformation mechanisms, with the stress-strain curves offering a clear delineation of distinct elastic and plastic regions within the material's behavior. Critical mechanical properties such as the stress of the yield point, the maximum stress before densification, and the stiffness were derived from these stress-strain curves. Furthermore, during these tests, the Poisson's ratio of the samples was calculated under varying displacement conditions, in addition to the determination of Total Energy Absorption (TEA) and Specific Energy Absorption (SEA) parameters, which contributed to a comprehensive assessment of the material's performance characteristics.

Several significant conclusions can be drawn from the outcomes of these experiments. The stress-strain curves exhibited remarkable similarities to those reported by Meena and Singamneni [119], despite the utilization of different materials. This observation suggests that the structural behavior of the S-shaped configuration is primarily influenced by its geometric attributes rather than the material properties. Notably, while the stress levels achieved by the stainless steel structures exceeded those of the PETG counterparts, the fundamental compression behavior of both structures remained consistent. Additionally, the strain values corresponding to the point of maximum stress before densification and the yield point exhibited striking similarities between the two materials.

Concerning the Poisson's ratio, the values acquired in this study exhibit slight deviations compared to those reported by Meena and Singamneni in Ref. [119]. This discrepancy may find its reason in the distinct visual deformation behaviors observed in the respective experiments. A visual inspection of the images provided in their research compared to those generated in the present investigation highlights notable distinctions. Despite the underlying geometric similarities between the two structures, the stainless steel "S" configuration featured in Meena and Singamneni's work [119] displayed a more uniform lateral deformation pattern, where the deformation in the two lines aligned with the faces resembled that of the two middle lines. In contrast, the PETG "S" structure exhibited a more pronounced lateral deformation in its central lines of "S" unit cells, with comparatively less deformation in the lines aligned with the faces, particularly evident at bigger displacements (Figures 4(h) and 4(i) of Meena and Singamneni's work [119] and images of displacements of 10 and 5 mm of Table 5.4). Remarkably, these central lines exhibited more substantial lateral deformation compared to the stainless steel "S" structure. This distinct deformation behavior can potentially account for the more negative Poisson's ratio values observed in the present study compared to the work by Meena and Singamneni [119], clarifying that material properties indeed exert an influence on Poisson's ratio, in addition to structural geometry.

Regarding energy absorption, it is worth noting that the compressive test employed in this study may not be the most suitable method for investigating this specific property. Ideally, an impact test would be more appropriate for such an analysis. However, the structural design of the S-shaped configuration was not optimized for impact testing. Consequently, the total energy absorption during the compressive test was calculated to provide insight into this aspect. Regrettably, the specific energy absorption (SEA) value obtained from these calculations, 0.352 kJ/kg, does not exhibit exceptionally high values but still demonstrates suitability for various industrial applications. These applications span a wide range of industries, including, but not limited to, composites, automotive crash safety, aeronautics, aerospace, sports equipment, and numerous other sectors.

Upon careful observation, it became evident that despite the fact that the S-shaped structure was compressed to a strain of 60%, there were no signs of cracking in any of the samples. This observation underscores the absence of significant stress concentrations within these structures, which is a common issue encountered in other types of auxetic structures, such as the re-entrant structure.

Another experimental test conducted on the S-shaped structure involved the creep-recovery test. Two distinct tests were performed, differing in the magnitude of displacement applied relative to the yield strength point. In the first test, a displacement of 1.7 mm was applied, and the results suggest that one hour of force application is adequate to achieve structural stabilization. Subsequent cycles are expected to demonstrate consistent behavior, and prolonging the duration of applied displacement may eventually result in a constant force level. These findings also suggest that this structure, when subjected to forces within the elastic region, can fully recover.

In the second creep-recovery test, a displacement of 4.6 mm was applied, and the results indicate that during the initial cycle, when this 4.6 mm displacement was imposed, the structure experienced a weakening effect, causing a decrease in sustained force. It is likely that if the displacement was applied for a longer duration, the force would further decrease, but eventually stabilize at a constant value. Additionally, it can be inferred that the recovery time allowed for the structure's recuperation, albeit not complete due to the plastic deformation it experienced. However, in subsequent cycles, the force endured by the structure exceeded the last recorded force value of the preceding cycle. This suggests that even when subjected to a force 30% above the yield point, the structure can withstand the load, albeit without displaying its optimal mechanical properties.

After completing the experimental phase of this research, the numerical phase was undertaken. Initially, a single-element numerical model was developed to ascertain the alignment of material properties with the prior experimental characterization of PETG. Following this, a simulation of a PETG specimen was conducted, to compare the simulation outcomes with the experimental data acquired during the specimen characterization process. This step aimed to evaluate the accuracy of the numerical model. Subsequently, the numerical model was adapted for use with the S-shaped structure. During this phase, it was determined that neither the implicit solver nor the explicit solver could accurately replicate the entire compression behavior of this structure.

The implicit solver demonstrated competence in simulating the initial stages of compression. However, when higher displacement values were applied, the solver exhibited issues related to structure penetration. Addressing this problem would require the implementation of a high number of contact interactions, demanding substantial computational resources that were beyond the scope of this work. In contrast, the explicit solver performed well in simulating the compression of the structure at higher displacement levels. Nevertheless, it encountered difficulties in accurately replicating the compression at lower displacement values. In light of these observations, a decision was made to integrate the results obtained from both solvers. Specifically, for the displacement range from 0 to 7.5 mm, the results from the implicit solver were considered, while for the range from 7.5 to 15 mm, the results from the explicit solver were utilized.

The numerical simulation of the compression of the S-shaped structure primarily allowed for a comparison of the Poisson's ratio with the experimental results. Upon comparing these values, it was determined that the Poisson's ratio data obtained through both experimental and numerical means exhibited a high degree of similarity. Remarkably, despite the fact that the numerical models for the structure were not entirely optimized, the results yielded a satisfactory level of agreement.

6.2 Future Perspectives

This section explores the horizons beyond the current study, shedding light on the potential directions for further research and applications in the field. Within this section, three key subsections are explored: (i) Limitations and Possible Improvements, (ii) Future Investigations, and (iii) Future Applications. Each subsection will provide valuable insight to the challenges and opportunities that lie ahead, offering a comprehensive view of the promising developments in the subject matter.

6.2.1 Limitations and Possible Improvements

Throughout this study, several challenges and limitations were encountered, affecting both the experimental and numerical aspects of the research.

One notable challenge pertained to the nozzle diameter of the 3D printer utilized, which had a diameter of 0.8 mm, whereas the most common nozzle size is 0.4 mm. While a larger nozzle diameter offers advantages such as increased filament deposition rates and consequently faster printing, it also results in wider extruded filament lines that allows, for example, doing a wall with 2 transitions instead of 4. Also using a larger nozzle allows printing with less filament retractions. Despite the above mentioned advantages, the use of a 0.8 mm nozzle led to reduced printing accuracy, particularly evident in the printed samples of the S-shaped structure. Employing a smaller nozzle, such as 0.4 mm or even smaller, would significantly enhance the accuracy of printed samples.

In the experimental phase, another limitation arose due to the unavailability of equipment capable of conducting an impact test on the S-shaped structure. Such a test would have provided more precise insight into the energy absorption characteristics of this structure. However, the absence of suitable equipment constrained the execution of this valuable test.

Concerning the numerical portion of the study, reproducing the compression behavior of the S-shaped structure posed a substantial challenge. Both the implicit and explicit solvers exhibited limitations in accurately simulating this compression behavior. To mitigate these limitations, substantial computational power and additional time for model refinement would be required. Improvements in mesh refinement, which was identified as a potential source of inaccuracies, could be achieved with increased computational resources. Additionally, a more reliable approach might involve simulating the structure's behavior up to 7.5 mm using the implicit solver, followed by the continuation of the simulation using the explicit solver imposing the initial imperfection as the final result of the implicit solver simulation. This combined approach could enhance the accuracy and reliability of the numerical model.

6.2.2 Future Investigations

This subsection is dedicated to outlining the prospective areas of research and exploration that can further advance the understanding of auxetic materials. In the realm of auxetic materials, there exists a plethora of unexplored avenues that hold promise for investigation. Below, several of these promising prospects are listed for future research endeavors:

- Reproduction this work but on other auxetic structures;
- Reproduction this work but using a different nozzle diameter;
- Reproduction this work but using a different material and different method of fabrication;
- Application of little modifications in existent auxetic structures and comparative work between these modified structures and the existent structures;
- Experimental and numerical comparative works between different auxetic structures with the same material;
- Experimental and numerical comparative works between different materials with the same auxetic structure;
- Impact tests in auxetic structures;
- Implementation of an auxetic structure in a composite core;
- Investigation on the use of auxetic structures in morphing structures.

6.2.3 Future Applications

This subsection is dedicated to delineating prospective applications for auxetic structures. Although this study has contributed to a deeper understanding of these distinctive materials, it is imperative to investigate their potential practical implementations. This section aims to elucidate potential domains in which auxetic structures could offer valuable applications, providing insight into their practical relevance and influence. Auxetic structures exhibit significant potential across a variety of domains, and below are some illustrative examples of their potential future applications:

- Protective gear and armor;
- Sports equipment;
- Biomedical devices;
- Shock-absorbing foundations and earthquake-resistant structures;
- Energy absorption systems;
- Car seats, airbags and bumpers;
- Expandable structures;
- Airplane seats and interiors;
- Strong lightweight structures for aircrafts and spacecrafts;
- Morphing airfoils.

Bibliography

[1] A. Alderson and K. L. Alderson, “Auxetic materials,” *Proceedings of the Institution of Mechanical Engineers, Part G: Journal of Aerospace Engineering*, vol. 221, pp. 565–575, 2007. [Online]. Available: https://doi.org/10.1243/09544100JAERO185 1, 2, 3

[2] G. Marsh, “Airframers exploit composites in battle for supremacy,” *Reinforced Plastics*, vol. 49, no. 3, pp. 26–32, 2005. [Online]. Available: https://doi.org/10.1016/S0034-3617(05)00577-1 1

[3] J. Austermann, A. J. Redmann, V. Dahmen, A. L. Quintanilla, S. J. Mecham, and T. A. Osswald, “Fiber-reinforced composite sandwich structures by co-curing with additive manufactured epoxy lattices,” *Journal of Composites Science*, vol. 3, no. 2, p. 53, may 2019. [Online]. Available: https://doi.org/10.3390/jcs3020053 1

[4] M. Alberto, *Introduction of Fibre-Reinforced Polymers - Polymers and Composites: Concepts, Properties and Processes*. InTech, jan 2013. [Online]. Available: https://www.intechopen.com/chapters/41941 1, 2

[5] J. K. Borchardt, “Unmanned aerial vehicles spur composites use,” *Reinforced Plastics*, vol. 48, no. 4, pp. 28–31, 2004. [Online]. Available: https://doi.org/10.1016/S0034-3617(04)00194-8 2

[6] M. M. and, “Advanced composite materials of the future in aerospace industry,” *INCAS BULLETIN*, vol. 5, no. 3, pp. 139–150, sep 2013. 2

[7] F. Usta, H. S. Türkmen, and F. Scarpa, “Low-velocity impact resistance of composite sandwich panels with various types of auxetic and non-auxetic core structures,” *Thin-Walled Structures*, vol. 163, p. 107738, jun 2021. [Online]. Available: https://doi.org/10.1016/j.tws.2021.107738 2

[8] T. A. Schaedler and W. B. Carter, “Architected cellular materials,” *Annual Review of Materials Research*, vol. 46, no. 1, pp. 187–210, jul 2016. [Online]. Available: https://doi.org/10.1146/annurev-matsci-070115-031624 2, 3

[9] T. Li and L. Wang, “Bending behavior of sandwich composite structures with tunable 3d-printed core materials,” *Composite Structures*, vol. 175, pp. 46–57, sep 2017. [Online]. Available: https://doi.org/10.1016/j.compstruct.2017.05.001 2

[10] S. M. Zaharia, L. A. Enescu, and M. A. Pop, “Mechanical performances of lightweight sandwich structures produced by material extrusion-based additive manufacturing,” *Polymers*, vol. 12, no. 8, p. 1740, aug 2020. [Online]. Available: https://doi.org/10.3390/polym12081740 2

[11] A. I. Indreş, D. M. Constantinescu, and O. A. Mocian, “Bending behavior of 3d printed sandwich beams with different core topologies,” *Material Design & Processing Communications*, vol. 3, no. 4, jun 2021. [Online]. Available: https://doi.org/10.1002/mdp2.252 2, 4

[12] S. D. Nath and S. Nilufar, “Performance evaluation of sandwich structures printed by vat photopolymerization,” *Polymers*, vol. 14, 4 2022. [Online]. Available: https://doi.org/10.3390/polym14081513 2

[13] D. S. Schwartz, D. S. Shih, A. G. Evans, and H. N. Wadley, *Porous and cellular materials for structural applications*, 12 1998. [Online]. Available: https://www.osti.gov/biblio/361796 2

[14] T. A. Schaedler, C. J. Ro, A. E. Sorensen, Z. Eckel, S. S. Yang, W. B. Carter, and A. J. Jacobsen, “Designing metallic microlattices for energy absorber applications,” *Advanced Engineering Materials*, vol. 16, no. 3, pp. 276–283, nov 2013. [Online]. Available: https://doi.org/10.1002/adem.201300206 2

[15] D. W. Abueidda, I. Jasiuk, and N. A. Sobh, “Acoustic band gaps and elastic stiffness of PMMA cellular solids based on triply periodic minimal surfaces,” *Materials & Design*, vol. 145, pp. 20–27, may 2018. [Online]. Available: https://doi.org/10.1016/j.matdes.2018.02.032 2

[16] V. T. Le and N. S. Goo, “Thermomechanical performance of bio-inspired corrugated-core sandwich structure for a thermal protection system panel,” *Applied Sciences*, vol. 9, no. 24, p. 5541, dec 2019. [Online]. Available: https://doi.org/10.3390/app9245541 2

[17] H. G. Allen, *Analysis and design of structural sandwich panels*, 1st ed., ser. The @Commonwealth and international library. Oxford [u.a.]: Pergamon Pr., 1969. [Online]. Available: https://doi.org/10.1016/C2013-0-02134-2 3

[18] K. Peliński and J. Smardzewski, “Static response of synclastic sandwich panel with auxetic wood-based honeycomb cores subject to compression,” *Thin-Walled Structures*, vol. 179, p. 109559, oct 2022. [Online]. Available: https://doi.org/10.1016/j.tws.2022.109559 3

[19] W. Huang, Z. Fan, W. Zhang, J. Liu, and W. Zhou, “Impulsive response of composite sandwich structure with tetrahedral truss core,” *Composites Science and Technology*, vol. 176, pp. 17–28, may 2019. [Online]. Available: https://doi.org/10.1016/j.compscitech.2019.03.020 3

[20] J. Xiong, R. Ghosh, L. Ma, H. Ebrahimi, A. Hamouda, A. Vaziri, and L. Wu, “Bending behavior of lightweight sandwich-walled shells with pyramidal truss cores,” *Composite Structures*, vol. 116, pp. 793–804, sep 2014. [Online]. Available: http://dx.doi.org/10.1016/j.compstruct.2014.06.006 3

[21] S. Li, Y. Feng, M. Wang, and Y. Hu, "Mechanical behavior of natural fiber-based bi-directional corrugated lattice sandwich structure," *Materials*, vol. 11, no. 12, p. 2578, dec 2018. [Online]. Available: http://dx.doi.org/10.3390/ma11122578 3

[22] L.-J. Feng, J. Xiong, L.-H. Yang, G.-C. Yu, W. Yang, and L.-Z. Wu, "Shear and bending performance of new type enhanced lattice truss structures," *International Journal of Mechanical Sciences*, vol. 134, pp. 589–598, dec 2017. [Online]. Available: http://dx.doi.org/10.1016/j.ijmecsci.2017.10.045 3

[23] B. Wang, J. Hu, Y. Li, Y. Yao, S. Wang, and L. Ma, "Mechanical properties and failure behavior of the sandwich structures with carbon fiber-reinforced x-type lattice truss core," *Composite Structures*, vol. 185, pp. 619–633, feb 2018. [Online]. Available: http://dx.doi.org/10.1016/J.COMPSTRUCT.2017.11.066 3

[24] J. Xiong, A. Vaziri, L. Ma, J. Papadopoulos, and L. Wu, "Compression and impact testing of two-layer composite pyramidal-core sandwich panels," *Composite Structures*, vol. 94, no. 2, pp. 793–801, jan 2012. [Online]. Available: http://dx.doi.org/10.1016/j.compstruct.2011.09.018 3

[25] B. R. Goncalves and J. Romanoff, "Size-dependent modelling of elastic sandwich beams with prismatic cores," *International Journal of Solids and Structures*, vol. 136-137, pp. 28–37, apr 2018. [Online]. Available: http://dx.doi.org/10.1016/J.IJSOLSTR.2017.12.001 3

[26] J. Smardzewski, "Wooden sandwich panels with prismatic core – energy absorbing capabilities," *Composite Structures*, vol. 230, p. 111535, dec 2019. [Online]. Available: http://dx.doi.org/10.1016/j.compstruct.2019.111535 3

[27] Z. Zhao, L. Li, X. Wang, Q. Zhang, B. Han, and T. Lu, "Strength optimization of ultralight corrugated-channel-core sandwich panels," *Science China Technological Sciences*, vol. 62, no. 8, pp. 1467–1477, dec 2018. [Online]. Available: http://dx.doi.org/10.1007/s11431-018-9356-8 3

[28] G. Chen, Y. Cheng, P. Zhang, J. Liu, C. Chen, and S. Cai, "Design and modelling of auxetic double arrowhead honeycomb core sandwich panels for performance improvement under air blast loading," *Journal of Sandwich Structures & Materials*, vol. 23, no. 8, pp. 3574–3605, jun 2020. [Online]. Available: http://dx.doi.org/10.1177/1099636220935563 3

[29] A. Florence and M. A. Jaswin, "Vibration and flexural characterization of hybrid honeycomb core sandwich panels filled with different energy absorbing materials," *Materials Research Express*, vol. 6, no. 7, p. 075326, apr 2019. [Online]. Available: http://dx.doi.org/10.1088/2053-1591/ab1576 3

[30] G. Sun, D. Chen, X. Huo, G. Zheng, and Q. Li, "Experimental and numerical studies on indentation and perforation characteristics of honeycomb sandwich panels,"

Composite Structures, vol. 184, pp. 110–124, jan 2018. [Online]. Available: http://dx.doi.org/10.1016/j.compstruct.2017.09.025 3

[31] M. Hussain, N. Abbas, N. Zahra, U. Sajjad, and M. B. Awan, "Investigating the performance of GFRP/wood-based honeycomb sandwich panels for sustainable prefab building construction," *SN Applied Sciences*, vol. 1, no. 8, jul 2019. [Online]. Available: http://dx.doi.org/10.1007/s42452-019-0932-3 3

[32] G. Sun, X. Huo, H. Wang, P. J. Hazell, and Q. Li, "On the structural parameters of honeycomb-core sandwich panels against low-velocity impact," *Composites Part B: Engineering*, vol. 216, p. 108881, jul 2021. [Online]. Available: http://dx.doi.org/10.1016/J.COMPOSITESB.2021.108881 3

[33] J. Xiong, Y. Du, D. Mousanezhad, M. E. Asl, J. Norato, and A. Vaziri, "Sandwich structures with prismatic and foam cores: A review," *Advanced Engineering Materials*, vol. 21, no. 1, p. 1800036, oct 2018. [Online]. Available: http://dx.doi.org/10.1002/adem.201800036 3

[34] F. Balıkoğlu, T. Demircioğlu, O. İnal, N. Arslan, and A. Ataş, "Compression after low velocity impact tests of marine sandwich composites: Effect of intermediate wooden layers," *Composite Structures*, vol. 183, pp. 636–642, jan 2018. [Online]. Available: http://dx.doi.org/10.1016/j.compstruct.2017.08.003 3

[35] R. Bai, J. Guo, Z. Lei, D. Liu, Y. Ma, and C. Yan, "Compression after impact behavior of composite foam-core sandwich panels," *Composite Structures*, vol. 225, p. 111181, oct 2019. [Online]. Available: http://dx.doi.org/10.1016/J.COMPSTRUCT.2019.111181 3

[36] X. Huo, H. Liu, Q. Luo, G. Sun, and Q. Li, "On low-velocity impact response of foam-core sandwich panels," *International Journal of Mechanical Sciences*, vol. 181, p. 105681, sep 2020. [Online]. Available: http://dx.doi.org/10.1016/J.IJMECSCI.2020.105681 3

[37] A. F. Nejad, S. R. Koloor, S. S. Hamzah, and M. Yahya, "Mechanical behaviour of pin-reinforced foam core sandwich panels subjected to low impact loading," *Polymers*, vol. 13, no. 21, p. 3627, oct 2021. [Online]. Available: http://dx.doi.org/10.3390/polym13213627 3

[38] B. Castanie, C. Bouvet, and M. Ginot, "Review of composite sandwich structure in aeronautic applications," *Composites Part C: Open Access*, vol. 1, p. 100004, aug 2020. [Online]. Available: http://dx.doi.org/10.1016/j.jcomc.2020.100004 3

[39] K. E. Evans, "Auxetic polymers: a new range of materials," *Endeavour*, vol. 15, no. 4, pp. 170–174, jan 1991. [Online]. Available: https://doi.org/10.1016/0160-9327(91)90123-S 4

[40] Z. Wang, A. Zulifqar, and H. Hu, “Auxetic composites in aerospace engineering,” pp. 213–240, 2016. [Online]. Available: https://doi.org/10.1016/B978-0-08-100037-3.00007-9 4, 5, 7

[41] P. Soman, D. Y. Fozdar, J. W. Lee, A. Phadke, S. Varghese, and S. Chen, “A three-dimensional polymer scaffolding material exhibiting a zero poisson's ratio,” *Soft Matter*, vol. 8, no. 18, p. 4946, 2012. 4

[42] K. Liu, L. Han, W. Hu, L. Ji, S. Zhu, Z. Wan, X. Yang, Y. Wei, Z. Dai, Z. Zhao, Z. Li, P. Wang, and R. Tao, “4d printed zero poisson's ratio metamaterial with switching function of mechanical and vibration isolation performance,” *Materials & Design*, vol. 196, p. 109153, nov 2020. 4

[43] L. Jiang and H. Hu, “Low-velocity impact response of multilayer orthogonal structural composite with auxetic effect,” *Composite Structures*, vol. 169, pp. 62–68, jun 2017. [Online]. Available: https://doi.org/10.1016/j.compstruct.2016.10.018 4

[44] R. Lakes, “Foam structures with a negative poisson’s ratio,” *Science*, vol. 235, no. 4792, pp. 1038–1040, feb 1987. [Online]. Available: https://doi.org/10.1126/science.235.4792.1038 4, 5, 15

[45] J. B. Choi and R. S. Lakes, “Non-linear properties of metallic cellular materials with a negative poisson's ratio,” *Journal of Materials Science*, vol. 27, no. 19, pp. 5375–5381, oct 1992. [Online]. Available: https://doi.org/10.1007/BF02403846 4, 15

[46] I. I. Argatov, R. Guinovart-Díaz, and F. J. Sabina, “On local indentation and impact compliance of isotropic auxetic materials from the continuum mechanics viewpoint,” *International Journal of Engineering Science*, vol. 54, pp. 42–57, may 2012. [Online]. Available: https://doi.org/10.1016/j.ijengsci.2012.01.010 4, 15

[47] J. B. Choi and R. S. Lakes, “Fracture toughness of re-entrant foam materials with a negative poisson's ratio: experiment and analysis,” *International Journal of Fracture*, vol. 80, no. 1, pp. 73–83, 1996. [Online]. Available: https://doi.org/10.1007/BF00036481 4

[48] A. Alderson, J. Rasburn, S. Ameer-Beg, P. G. Mullarkey, W. Perrie, and K. E. Evans, “An auxetic filter: a tuneable filter displaying enhanced size selectivity or defouling properties,” *Industrial & Engineering Chemistry Research*, vol. 39, no. 3, pp. 654–665, jan 2000. [Online]. Available: https://doi.org/10.1021/ie990572w 4

[49] G. Imbalzano, P. Tran, T. D. Ngo, and P. V. Lee, “A numerical study of auxetic composite panels under blast loadings,” *Composite Structures*, vol. 135, pp. 339–352, jan 2016. [Online]. Available: https://doi.org/10.1016/j.compstruct.2015.09.038 4, 17

[50] K. Alderson and K. Evans, “The fabrication of microporous polyethylene having a negative poisson's ratio,” *Polymer*, vol. 33, no. 20, pp. 4435–4438, jan 1992. [Online]. Available: https://doi.org/10.1016/0032-3861(92)90294-7 5

[51] K. E. Evans and B. D. Caddock, “Microporous materials with negative poisson's ratios. II. mechanisms and interpretation,” *Journal of Physics D: Applied Physics*, vol. 22, no. 12, pp. 1883–1887, dec 1989. [Online]. Available: https://dx.doi.org/10.1088/0022-3727/22/12/013 5

[52] N. Ravirala, A. Alderson, K. L. Alderson, and P. J. Davies, “Expanding the range of auxetic polymeric products using a novel melt-spinning route,” *physica status solidi (b)*, vol. 242, no. 3, pp. 653–664, mar 2005. [Online]. Available: https://doi.org/10.1002/pssb.200460384 5

[53] M. Sloan, J. Wright, and K. Evans, “The helical auxetic yarn – a novel structure for composites and textiles geometry, manufacture and mechanical properties,” *Mechanics of Materials*, vol. 43, no. 9, pp. 476–486, sep 2011. [Online]. Available: https://doi.org/10.1016/j.mechmat.2011.05.003 5

[54] Z. Wang and H. Hu, “3d auxetic warp-knitted spacer fabrics,” *physica status solidi (b)*, vol. 251, no. 2, pp. 281–288, sep 2013. [Online]. Available: https://doi.org/10.1002/pssb.201384239 5

[55] Q. Ma, M. Rejab, J. Siregar, and Z. Guan, “A review of the recent trends on core structures and impact response of sandwich panels,” *Journal of Composite Materials*, vol. 55, no. 18, pp. 2513–2555, feb 2021. 5

[56] A. V. Mazaev, O. Ajeneza, and M. V. Shitikova, “Auxetics materials: classification, mechanical properties and applications,” *IOP Conference Series: Materials Science and Engineering*, vol. 747, no. 1, p. 012008, jan 2020. [Online]. Available: https://iopscience.iop.org/article/10.1088/1757-899X/747/1/012008 6, 19

[57] M. Balan P, J. Mertens A, and M. V. A. R. Bahubalendruni, “Auxetic mechanical metamaterials and their futuristic developments: A state-of-art review,” *Materials Today Communications*, vol. 34, p. 105285, 2023. [Online]. Available: https://doi.org/10.1016/j.mtcomm.2022.105285 8, 9, 17, 18, 19, 20, 21, 22, 23

[58] V. H. Carneiro, J. Meireles, and H. Puga, “Auxetic materials — a review,” *Materials Science-Poland*, vol. 31, no. 4, pp. 561–571, oct 2013. [Online]. Available: https://doi.org/10.2478/s13536-013-0140-6 13, 14, 15

[59] K. E. Evans and A. Alderson, “Auxetic materials: Functional materials and structures from lateral thinking!” *Advanced Materials*, vol. 12, no. 9, pp. 617–628, may 2000. [Online]. Available: https://doi.org/10.1002/(SICI)1521-4095(200005)12:9<617::AID-ADMA617>3.0.CO;2-3 14

[60] Y. Prawoto, “Seeing auxetic materials from the mechanics point of view: A structural review on the negative poisson’s ratio,” *Computational Materials Science*, vol. 58, pp. 140–153, jun 2012. [Online]. Available: https://doi.org/10.1016/j.commatsci.2012.02.012 14

[61] A. Alderson, “A triumph of lateral thought,” *Chemistry & Industry*, pp. 384–387, 1999. 14

[62] R. Critchley, I. Corni, J. A. Wharton, F. C. Walsh, R. J. K. Wood, and K. R. Stokes, “A review of the manufacture, mechanical properties and potential applications of auxetic foams,” *physica status solidi (b)*, vol. 250, no. 10, pp. 1963–1982, apr 2013. [Online]. Available: https://doi.org/10.1002/pssb.201248550 15

[63] K. V. Tretiakov and K. W. Wojciechowski, “Elasticity of two-dimensional crystals of polydisperse hard disks near close packing: Surprising behavior of the poisson's ratio,” *The Journal of Chemical Physics*, vol. 136, no. 20, p. 204506, may 2012. [Online]. Available: https://doi.org/10.1063/1.4722100 15

[64] V. L. Coenen and K. L. Alderson, “Mechanisms of failure in the static indentation resistance of auxetic carbon fibre laminates,” *physica status solidi (b)*, vol. 248, no. 1, pp. 66–72, sep 2010. [Online]. Available: https://doi.org/10.1002/pssb.201083977 15

[65] J. Dirrenberger, S. Forest, and D. Jeulin, “Effective elastic properties of auxetic microstructures: anisotropy and structural applications,” *International Journal of Mechanics and Materials in Design*, vol. 9, no. 1, pp. 21–33, may 2012. [Online]. Available: https://doi.org/10.1007/s10999-012-9192-8 15

[66] J. P. Donoghue, K. L. Alderson, and K. E. Evans, “The fracture toughness of composite laminates with a negative poisson's ratio,” *physica status solidi (b)*, vol. 246, no. 9, pp. 2011–2017, aug 2009. [Online]. Available: https://doi.org/10.1002/pssb.200982031 15

[67] S. Yang, V. B. Chalivendra, and Y. K. Kim, “Fracture and impact characterization of novel auxetic kevlar®/epoxy laminated composites,” *Composite Structures*, vol. 168, pp. 120–129, may 2017. [Online]. Available: https://doi.org/10.1016/j.compstruct.2017.02.034 15

[68] J. Grima, “Modelling auxetic materials,” *Gdansk, Poland*, 2009. 15

[69] R. S. Lakes and R. Witt, “Making and characterizing negative poisson's ratio materials,” *International Journal of Mechanical Engineering Education*, vol. 30, no. 1, pp. 50–58, jan 2002. [Online]. Available: https://doi.org/10.7227/IJMEE.30.1.5 15

[70] A. Lorato, P. Innocenti, F. Scarpa, A. Alderson, K. Alderson, K. Zied, N. Ravirala, W. Miller, C. Smith, and K. Evans, “The transverse elastic properties of chiral

honeycombs," *Composites Science and Technology*, vol. 70, no. 7, pp. 1057–1063, jul 2010. [Online]. Available: https://doi.org/10.1016/j.compscitech.2009.07.008 15

[71] A. Alderson, K. Alderson, G. Chirima, N. Ravirala, and K. Zied, "The in-plane linear elastic constants and out-of-plane bending of 3-coordinated ligament and cylinder-ligament honeycombs," *Composites Science and Technology*, vol. 70, no. 7, pp. 1034–1041, jul 2010. [Online]. Available: https://doi.org/10.1016/j.compscitech.2009.07.010 16

[72] X. Ren, R. Das, P. Tran, T. D. Ngo, and Y. M. Xie, "Auxetic metamaterials and structures: a review," *Smart Materials and Structures*, vol. 27, no. 2, p. 023001, jan 2018. [Online]. Available: https://dx.doi.org/10.1088/1361-665X/aaa61c 16, 18, 21

[73] J. N. Grima, "Auxetic metamaterials," 2010. 16

[74] A. Alderson, J. Rasburn, K. Evans, and J. Grima, "Auxetic polymeric filters display enhanced de-fouling and pressure compensation properties," *Membrane Technology*, vol. 2001, no. 137, pp. 6–8, sep 2001. [Online]. Available: https://doi.org/10.1016/S0958-2118(01)80299-8 16

[75] A. Alderson, J. Rasburn, and K. E. Evans, "Mass transport properties of auxetic (negative poisson's ratio) foams," *physica status solidi (b)*, vol. 244, no. 3, pp. 817–827, mar 2007. [Online]. Available: https://doi.org/10.1002/pssb.200572701 16

[76] Q. Chen and N. M. Pugno, "In-plane elastic buckling of hierarchical honeycomb materials," *European Journal of Mechanics - A/Solids*, vol. 34, pp. 120–129, jul 2012. [Online]. Available: https://doi.org/10.1016/j.euromechsol.2011.12.003 17

[77] S. Yang, C. Qi, D. Wang, R. Gao, H. Hu, and J. Shu, "A comparative study of ballistic resistance of sandwich panels with aluminum foam and auxetic honeycomb cores," *Advances in Mechanical Engineering*, vol. 5, p. 589216, jan 2013. [Online]. Available: https://doi.org/10.1155/2013/589216 17

[78] S. Mohsenizadeh, R. Alipour, M. S. Rad, A. F. Nejad, and Z. Ahmad, "Crashworthiness assessment of auxetic foam-filled tube under quasi-static axial loading," *Materials & Design*, vol. 88, pp. 258–268, dec 2015. [Online]. Available: https://doi.org/10.1016/j.matdes.2015.08.152 17

[79] G. Imbalzano, S. Linforth, T. D. Ngo, P. V. S. Lee, and P. Tran, "Blast resistance of auxetic and honeycomb sandwich panels: Comparisons and parametric designs," *Composite Structures*, vol. 183, pp. 242–261, jan 2018. [Online]. Available: https://doi.org/10.1016/j.compstruct.2017.03.018 17

[80] C. Qi, A. Remennikov, L.-Z. Pei, S. Yang, Z.-H. Yu, and T. D. Ngo, "Impact and close-in blast response of auxetic honeycomb-cored sandwich panels: Experimental

tests and numerical simulations," *Composite Structures*, vol. 180, pp. 161–178, nov 2017. [Online]. Available: https://doi.org/10.1016/j.compstruct.2017.08.020 17

[81] F. Scarpa, W. A. Bullough, and P. Lumley, "Trends in acoustic properties of iron particle seeded auxetic polyurethane foam," *Proceedings of the Institution of Mechanical Engineers, Part C: Journal of Mechanical Engineering Science*, vol. 218, no. 2, pp. 241–244, feb 2004. [Online]. Available: https://doi.org/10.1243/095440604322887099 17

[82] R. Johnston and Z. Kazancı, "Analysis of additively manufactured (3d printed) dual-material auxetic structures under compression," *Additive Manufacturing*, vol. 38, 2 2021. [Online]. Available: https://doi.org/10.1016/j.addma.2020.101783 17

[83] M. R. Hassan, F. Scarpa, N. A. Mohamed, and M. Ruzzene, "Tensile properties of shape memory alloy chiral honeycombs," *physica status solidi (b)*, vol. 245, no. 11, pp. 2440–2444, nov 2008. [Online]. Available: https://doi.org/10.1002/pssb.200880263 17

[84] S. Jacobs, C. Coconnier, D. DiMaio, F. Scarpa, M. Toso, and J. Martinez, "Deployable auxetic shape memory alloy cellular antenna demonstrator: design, manufacturing and modal testing," *Smart Materials and Structures*, vol. 21, no. 7, p. 075013, jun 2012. [Online]. Available: https://iopscience.iop.org/article/10.1088/0964-1726/21/7/075013 17

[85] M. Bianchi, F. Scarpa, and C. Smith, "Shape memory behaviour in auxetic foams: Mechanical properties," *Acta Materialia*, vol. 58, no. 3, pp. 858–865, feb 2010. [Online]. Available: https://doi.org/10.1016/j.actamat.2009.09.063 17

[86] F. Scarpa, P. Pastorino, A. Garelli, S. Patsias, and M. Ruzzene, "Auxetic compliant flexible pu foams: static and dynamic properties," *physica status solidi (b)*, vol. 242, no. 3, pp. 681–694, Feb. 2005. [Online]. Available: https://onlinelibrary.wiley.com/doi/10.1002/pssb.200460386 17

[87] A. Alderson, K. L. Alderson, S. A. McDonald, B. Mottershead, S. Nazare, P. J. Withers, and Y. T. Yao, "Piezomorphic materials," *Macromolecular Materials and Engineering*, vol. 298, no. 3, pp. 318–327, jun 2012. [Online]. Available: https://doi.org/10.1002/mame.201200028 17

[88] M. Bianchi, S. Frontoni, F. Scarpa, and C. W. Smith, "Density change during the manufacturing process of PU-PE open cell auxetic foams," *physica status solidi (b)*, vol. 248, no. 1, pp. 30–38, aug 2010. [Online]. Available: https://doi.org/10.1002/pssb.201083966 17

[89] K. K. Saxena, R. Das, and E. P. Calius, “Three decades of auxetics research - materials with negative poisson's ratio: A review,” *Advanced Engineering Materials*, vol. 18, no. 11, pp. 1847–1870, jun 2016. [Online]. Available: https://doi.org/10.1002/adem.201600053 18

[90] L. J. Gibson and M. F. Ashby, “Cellular solids,” may 1997. [Online]. Available: https://doi.org/10.1017/CBO9781139878326 18

[91] J. N. Grima, R. Gatt, and P.-S. Farrugia, “On the properties of auxetic meta-tetrachiral structures,” *physica status solidi (b)*, vol. 245, no. 3, pp. 511–520, mar 2008. [Online]. Available: https://doi.org/10.1002/pssb.200777704 18, 22, 24

[92] J. N. Grima and K. E. Evans, “Auxetic behavior from rotating squares,” *Journal of Materials Science Letters*, vol. 19, no. 17, pp. 1563–1565, 2000. [Online]. Available: https://doi.org/10.1023/A:1006781224002 18, 21

[93] J. Qiao and C. Q. Chen, “Analyses on the in-plane impact resistance of auxetic double arrowhead honeycombs,” *Journal of Applied Mechanics*, vol. 82, no. 5, may 2015. [Online]. Available: https://doi.org/10.1115/1.4030007 18

[94] X.-T. Wang, B. Wang, X.-W. Li, and L. Ma, “Mechanical properties of 3d re-entrant auxetic cellular structures,” *International Journal of Mechanical Sciences*, vol. 131-132, pp. 396–407, oct 2017. [Online]. Available: https://doi.org/10.1016/j.ijmecsci.2017.05.048 18

[95] L. J. Gibson, M. F. Ashby, G. S. Schajer, and C. I. Robertson, “The mechanics of two-dimensional cellular materials,” *Proceedings of the Royal Society of London. A. Mathematical and Physical Sciences*, vol. 382, no. 1782, pp. 25–42, jul 1982. [Online]. Available: https://doi.org/10.1098/rspa.1982.0087 18

[96] I. Masters and K. Evans, “Models for the elastic deformation of honeycombs,” *Composite Structures*, vol. 35, no. 4, pp. 403–422, aug 1996. [Online]. Available: https://doi.org/10.1016/S0263-8223(96)00054-2 18

[97] J. A. J, J. Schneider, A. Schiffer, F. Hafeez, and S. Kumar, “Dynamic crushing of tailored honeycombs realized via additive manufacturing,” *International Journal of Mechanical Sciences*, vol. 219, p. 107126, apr 2022. [Online]. Available: https://doi.org/10.1016/j.ijmecsci.2022.107126 19

[98] K. Evans, M. Nkansah, and I. Hutchinson, “Auxetic foams: Modelling negative poisson's ratios,” *Acta Metallurgica et Materialia*, vol. 42, no. 4, pp. 1289–1294, apr 1994. [Online]. Available: https://doi.org/10.1016/0956-7151(94)90145-7 19

[99] L. Yang, O. Harrysson, H. West, and D. Cormier, “Mechanical properties of 3d re-entrant honeycomb auxetic structures realized via additive manufacturing,” *International Journal of Solids and Structures*, vol. 69-70, pp. 475–490, sep 2015. [Online]. Available: https://doi.org/10.1016/j.ijsolstr.2015.05.005 19

[100] J. N. Grima, R. Gatt, A. Alderson, and K. E. Evans, “On the potential of connected stars as auxetic systems,” *Molecular Simulation*, vol. 31, no. 13, pp. 925–935, nov 2005. [Online]. Available: https://doi.org/10.1080/08927020500401139 20

[101] B. Boopathi, G. Ponniah, and R. G. Burela, “Realizing the impact and compressive strengths of an arrowhead auxetic structure inspired by topology optimization,” *International Journal of Advances in Engineering Sciences and Applied Mathematics*, vol. 12, no. 3-4, pp. 211–217, dec 2020. [Online]. Available: https://doi.org/10.1007/s12572-021-00286-w 20

[102] C. Lira, F. Scarpa, and R. Rajasekaran, “A gradient cellular core for aeroengine fan blades based on auxetic configurations,” *Journal of Intelligent Material Systems and Structures*, vol. 22, no. 9, pp. 907–917, jun 2011. [Online]. Available: https://doi.org/10.1177/1045389X11414226 20

[103] J. N. Grima, P.-S. Farrugia, R. Gatt, and D. Attard, “On the auxetic properties of rotating rhombi and parallelograms: A preliminary investigation,” *physica status solidi (b)*, vol. 245, no. 3, pp. 521–529, mar 2008. [Online]. Available: https://doi.org/10.1002/pssb.200777705 21

[104] K. E. Evans and A. Alderson, “Rotation and dilation deformation mechanisms for auxetic behaviour in the α-cristobalite tetrahedral framework structure,” *Physics and Chemistry of Minerals*, vol. 28, no. 10, pp. 711–718, nov 2001. [Online]. Available: https://doi.org/10.1007/s002690100209 21

[105] A. Rafsanjani and D. Pasini, “Bistable auxetic mechanical metamaterials inspired by ancient geometric motifs,” *Extreme Mechanics Letters*, vol. 9, pp. 291–296, dec 2016. [Online]. Available: https://doi.org/10.1016/j.eml.2016.09.001 21

[106] J. N. Grima, A. Alderson, and K. E. Evans, “Negative poisson’s ratios from rotating rectangles,” 2004. [Online]. Available: http://dx.doi.org/10.12921/cmst.2004.10.02.137-145 21

[107] K. Wojciechowski, “Two-dimensional isotropic system with a negative poisson ratio,” *Physics Letters A*, vol. 137, no. 1-2, pp. 60–64, may 1989. [Online]. Available: https://doi.org/10.1016/0375-9601(89)90971-7 21

[108] D. Prall and R. Lakes, “Properties of a chiral honeycomb with a poisson's ratio of — 1,” *International Journal of Mechanical Sciences*, vol. 39, no. 3, pp. 305–314, mar 1997. [Online]. Available: https://doi.org/10.1016/S0020-7403(96)00025-2 21

[109] W. Wu, D. Qi, H. Liao, G. Qian, L. Geng, Y. Niu, and J. Liang, “Deformation mechanism of innovative 3d chiral metamaterials,” *Scientific Reports*, vol. 8, no. 1, aug 2018. [Online]. Available: https://doi.org/10.1038/s41598-018-30737-7 22

[110] D. Mousanezhad, B. Haghpanah, R. Ghosh, A. M. Hamouda, H. Nayeb-Hashemi, and A. Vaziri, "Elastic properties of chiral, anti-chiral, and hierarchical honeycombs: A simple energy-based approach," *Theoretical and Applied Mechanics Letters*, vol. 6, no. 2, pp. 81–96, mar 2016. [Online]. Available: https://doi.org/10.1016/j.taml.2016.02.004 22

[111] R. Gatt, D. Attard, P.-S. Farrugia, K. M. Azzopardi, L. Mizzi, J.-P. Brincat, and J. N. Grima, "A realistic generic model for anti-tetrachiral systems," *physica status solidi (b)*, vol. 250, no. 10, pp. 2012–2019, sep 2013. [Online]. Available: https://doi.org/10.1002/pssb.201384246 22, 23

[112] R. Gatt, J. P. Brincat, K. M. Azzopardi, L. Mizzi, and J. N. Grima, "On the effect of the mode of connection between the node and the ligaments in anti-tetrachiral systems," *Advanced Engineering Materials*, vol. 17, no. 2, pp. 189–198, jun 2014. [Online]. Available: https://doi.org/10.1002/adem.201400120 23

[113] J. Rossiter, K. Takashima, F. Scarpa, P. Walters, and T. Mukai, "Shape memory polymer hexachiral auxetic structures with tunable stiffness," *Smart Materials and Structures*, vol. 23, no. 4, p. 045007, feb 2014. [Online]. Available: https://iopscience.iop.org/article/10.1088/0964-1726/23/4/045007 23

[114] A. Airoldi, P. Bettini, P. Panichelli, M. F. Oktem, and G. Sala, "Chiral topologies for composite morphing structures - part i: Development of a chiral rib for deformable airfoils," *physica status solidi (b)*, vol. 252, no. 7, pp. 1435–1445, jun 2015. [Online]. Available: https://doi.org/10.1002/pssb.201451689 23

[115] A. Airoldi, P. Bettini, P. Panichelli, and G. Sala, "Chiral topologies for composite morphing structures - part II: Novel configurations and technological processes," *physica status solidi (b)*, vol. 252, no. 7, pp. 1446–1454, jun 2015. [Online]. Available: https://doi.org/10.1002/pssb.201584263 23

[116] D. Bornengo, F. Scarpa, and C. Remillat, "Evaluation of hexagonal chiral structure for morphing airfoil concept," *Proceedings of the Institution of Mechanical Engineers, Part G: Journal of Aerospace Engineering*, vol. 219, no. 3, pp. 185–192, mar 2005. [Online]. Available: https://doi.org/10.1243/095441005X30216 23

[117] P. R. Budarapu, S. S. Y. B, and R. Natarajan, "Design concepts of an aircraft wing: composite and morphing airfoil with auxetic structures," *Frontiers of Structural and Civil Engineering*, vol. 10, no. 4, pp. 394–408, dec 2016. [Online]. Available: https://doi.org/10.1007/s11709-016-0352-z 23

[118] X. Gong, J. Huang, F. Scarpa, Y. Liu, and J. Leng, "Zero poisson's ratio cellular structure for two-dimensional morphing applications," *Composite Structures*, vol. 134, pp. 384–392, dec 2015. [Online]. Available: https://doi.org/10.1016/j.compstruct.2015.08.048 23

[119] K. Meena and S. Singamneni, “A new auxetic structure with significantly reduced stress concentration effects,” *Materials &amp Design*, vol. 173, p. 107779, jul 2019. [Online]. Available: https://doi.org/10.1016/j.matdes.2019.107779 24, 25, 26, 37, 41, 65, 66, 70, 74, 75

[120] J. Xiong, D. Gu, H. Chen, D. Dai, and Q. Shi, “Structural optimization of re-entrant negative poisson’s ratio structure fabricated by selective laser melting,” *Materials and Design*, vol. 120, pp. 307–316, apr 2017. [Online]. Available: https://doi.org/10.1016/j.matdes.2017.02.022 25

[121] T. Pereira, J. V. Kennedy, and J. Potgieter, “A comparison of traditional manufacturing vs additive manufacturing, the best method for the job,” *Procedia Manufacturing*, vol. 30, pp. 11–18, 2019. [Online]. Available: https://www.sciencedirect.com/science/article/pii/S2351978919300332?via=ihub 28

[122] P. N. by Hubs, “Additive manufacturing technologies,” accessed January 8, 2024. [Online]. Available: https://www.hubs.com/get/am-technologies/ 29, 30

[123] A. Joseph, V. Mahesh, and D. Harursampath, “On the application of additive manufacturing methods for auxetic structures: a review,” *Advances in Manufacturing*, vol. 9, no. 3, pp. 342–368, jun 2021. [Online]. Available: https://link.springer.com/article/10.1007/s40436-021-00357-y 28

[124] S. Masood, “Advances in fused deposition modeling,” in *Comprehensive Materials Processing*. Elsevier, 2014, pp. 69–91. [Online]. Available: https://www.sciencedirect.com/science/article/abs/pii/B9780080965321010025 31

[125] S. Park, K. Deng, and K. K. Fu, “Additive manufacturing including laser-based manufacturing,” in *Sustainable Manufacturing Processes*. Elsevier, 2023, pp. 285–311. [Online]. Available: https://www.sciencedirect.com/science/article/abs/pii/B9780323999908000102 32

[126] Simplify3D, “Filament properties table,” accessed January 14, 2024. [Online]. Available: https://www.simplify3d.com/resources/materials-guide/properties-table/ 33

[127] Tucab, “Fil3d petg ficha técnica,” accessed April 5, 2023. [Online]. Available: https://www.tucab.pt/zArchives/Photos/PG-121/fil3d-petg-20210427.pdf 36

[128] ASTM, “Astm d638-10 standard test method for tensile properties of plastics,” accessed October 13, 2023. [Online]. Available: https://www.astm.org/d0638-10.html 37

[129] J. N. Reddy, *Introduction to the Finite Element Method*, 3rd ed. New York, N.Y.: McGraw-Hill Education, 2006, includes bibliographical references and index. - Description based on e-Publication PDF. 47, 48

[130] M. N. Bismarck-Nasr, “Finite elements in applied mechanics,” p. 518, 1993. 48

[131] Ansys, “Ansys help,” accessed October 19, 2023. [Online]. Available: https://ansyshelp.ansys.com/account/secured?returnurl=/Views/Secured/corp/v212/en/wb_sim/ds_Home.html%23ds_Home 50, 56